NAVAL POSTGRADUATE SCHOOL

MONTEREY, CALIFORNIA

THESIS

RANGE SIDELOBE RESPONSE FROM THE USE OF POLYPHASE SIGNALS IN SPOTLIGHT SYNTHETIC APERTURE RADAR

by

Danny M. Lang

December 2015

Thesis Advisor: David A.Garren
Co-Advisor: Phillip E. Pace

Approved for public release; distribution is unlimited

THIS PAGE INTENTIONALLY LEFT BLANK

REPORT DOCUMENTATION PAGE

Form Approved OMB No. 0704–0188

Public reporting burden for this collection of information is estimated to average 1 hour per response, including the time for reviewing instruction, searching existing data sources, gathering and maintaining the data needed, and completing and reviewing the collection of information. Send comments regarding this burden estimate or any other aspect of this collection of information, including suggestions for reducing this burden, to Washington headquarters Services, Directorate for Information Operations and Reports, 1215 Jefferson Davis Highway, Suite 1204, Arlington, VA 22202-4302, and to the Office of Management and Budget, Paperwork Reduction Project (0704-0188) Washington, DC 20503.

1. AGENCY USE ONLY (*Leave blank*)	2. REPORT DATE December 2015	3. REPORT TYPE AND DATES COVERED Master's thesis	
4. TITLE AND SUBTITLE RANGE SIDELOBE RESPONSE FROM THE USE OF POLYPHASE SIGNALS IN SPOTLIGHT SYNTHETIC APERTURE RADAR			**5. FUNDING NUMBERS**
6. AUTHOR(S) Danny M. Lang			
7. PERFORMING ORGANIZATION NAME(S) AND ADDRESS(ES) Center for Joint Services Electronic Warfare Naval Postgraduate School Monterey, CA 93943-5000			**8. PERFORMING ORGANIZATION REPORT NUMBER**
9. SPONSORING /MONITORING AGENCY NAME(S) AND ADDRESS(ES) N/A			**10. SPONSORING / MONITORING AGENCY REPORT NUMBER**

11. SUPPLEMENTARY NOTES The views expressed in this thesis are those of the author and do not reflect the official policy or position of the Department of Defense or the U.S. Government.

12a. DISTRIBUTION / AVAILABILITY STATEMENT Approved for public release; distribution is unlimited	12b. DISTRIBUTION CODE

13. ABSTRACT (maximum 200 words)

This thesis investigated five specific phase-shift keyed (PSK) modulated signals for usage in Spotlight Synthetic Aperture Radars (SAR) and the effects each of the individual PSK signals sidelobe structure has on SAR imagery. The specific PSK codes studied were the Frank code, P1 code, P2 code, P3 code and P4 code. A mathematical approach was used to define SAR limitations from signal parameters, and simulations were used to investigate an individual signal parameter's effects on the sidelobe structure in SAR images. Simulations were used to generate spatially diverse targets, collect each target's unique echo and apply cross-correlation match filtering and pulse integration to detect each returned echo from the targeted area.

Results show the P1 and Frank codes to be the most promising based on the selected parameter presented in this thesis. The P4 code may be better given additional processing to remove range ambiguities, enhancing its unambiguous range.

14. SUBJECT TERMS Synthetic aperture radar, peak side lobe level, phase shift key, polyphase, range sidelobes			15. NUMBER OF PAGES 115
			16. PRICE CODE
17. SECURITY CLASSIFICATION OF REPORT Unclassified	18. SECURITY CLASSIFICATION OF THIS PAGE Unclassified	19. SECURITY CLASSIFICATION OF ABSTRACT Unclassified	20. LIMITATION OF ABSTRACT UU

NSN 7540–01–280-5500

Standard Form 298 (Rev. 2–89) Prescribed by ANSI Std. 239–18

THIS PAGE INTENTIONALLY LEFT BLANK

RANGE SIDELOBE RESPONSE FROM THE USE OF POLYPHASE SIGNALS IN SPOTLIGHT SYNTHETIC APERTURE RADAR

Danny M. Lang
Civilian, Sr. Electrical Engineer II, Raytheon
B.S., University of California, Santa Barbara, 2007

Submitted in partial fulfillment of the
requirements for the degree of

MASTER OF SCIENCE IN ELECTRICAL ENGINEERING

from the

NAVAL POSTGRADUATE SCHOOL
December 2015

Approved by: David A. Garren
                    Thesis Advisor

                    Phillip E. Pace
                    Co-Advisor

                    R. Clark Robertson
                    Chair, Department of Electrical and Computer Engineering

THIS PAGE INTENTIONALLY LEFT BLANK

ABSTRACT

This thesis investigated five specific phase-shift keyed (PSK) modulated signals for usage in Spotlight Synthetic Aperture Radars (SAR) and the effects each of the individual PSK signals sidelobe structure has on SAR imagery. The specific PSK codes studied were the Frank code, P1 code, P2 code, P3 code and P4 code. A mathematical approach was used to define SAR limitations from signal parameters, and simulations were used to investigate an individual signal parameter's effects on the sidelobe structure in SAR images. Simulations were used to generate spatially diverse targets, collect each target's unique echo and apply cross-correlation match filtering and pulse integration to detect each returned echo from the targeted area.

Results show the P1 and Frank codes to be the most promising based on the selected parameter presented in this thesis. The P4 code may be better given additional processing to remove range ambiguities, enhancing its unambiguous range.

THIS PAGE INTENTIONALLY LEFT BLANK

TABLE OF CONTENTS

THIS PAGE INTENTIONALLY LEFT BLANK

LIST OF FIGURES

THIS PAGE INTENTIONALLY LEFT BLANK

LIST OF TABLES

THIS PAGE INTENTIONALLY LEFT BLANK

LIST OF ACRONYMS AND ABBREVIATIONS

ACF	Autocorrelation Function
ADC	Analog-to-Digital Converter
CW	Continuous Wave
FMCW	Frequency Modulated Continuous Wave
LPI	Low Probability of Intercept
LFM	Linearly Frequency Modulated
PRI	Pulse Repetition Interval
PSK	Phase-Shift Keying
RADAR	Radio Detection and Ranging
RAR	Real Aperture Radar
Ru	Unambiguous Range
SAR	Synthetic Aperture Radar
SNR	Signal-to-Noise Ratio

THIS PAGE INTENTIONALLY LEFT BLANK

ACKNOWLEDGMENTS

First, I would like to thank Professors Garren and Pace for their guidance and assistance in the development of this thesis. Working with both of them has been a privilege and an honor.

I want to thank my loving wife, Stephanie, for standing by my side and encouraging me to complete this chapter in my life. Without her encouragement and patience, this thesis and would not have come to closure. I also want to thank my mother for raising me and instilling in me the work ethic and values that have propelled me through life. I would also like to thank my mother-in-law for helping my wife and me keep our home in order while we both have been in school and holding full-time jobs.

Finally, I want to thank Raytheon for its support of my educational goals.

THIS PAGE INTENTIONALLY LEFT BLANK

I. INTRODUCTION

Radio detection and ranging, also known as radar, is an instrument used to detect and locate targets at a distance [1]. Radar imaging uses the same idea but images targets at a distance instead and has been implemented in a variety of civilian and military applications since its inception in the mid-20th century [2]. The use of imaging radars allows for continuing operations in the absence of optical sensors due to inadequate light, poor weather conditions or other visual obstructions [2]. The ability of imaging radars to operate in day or night and in all weather conditions created many applications for their use. Some civilian employments of radar imaging include earth surface and sea floor mapping, agricultural evaluation, and geographic surveying. A few of the military uses of radar imaging include payload guidance, theater of operation surveillance and remote sensing [3].

Synthetic aperture radar (SAR) is an advanced radar technique used for producing two-dimensional images of a targeted area or object. The concept of SAR was established in June of 1951 by Carl Wiley of the Goodyear Aircraft Corporation. Wiley found by comparing multiple pulse returns from a moving radar that finer azimuth, or cross-range resolution, as compared to a real antenna beam pattern could be synthesized [4]. This antenna synthesis is performed through coherent summation of multiple returned target echoes over a portion of the radar's movement path. To generate a synthetic aperture, the radar transmits and receives signals at fixed, steady intervals along the radar's path of movement. The distance over which the radar transmits and receives signals is the size or length of the synthetic aperture. At each of the fixed intervals of the radars' trajectory, a signal is transmitted and received, and the returned range profile data is stored to be reused in the formation of the image after the synthetic aperture is traversed. SAR systems rely on this relative movement between the radar and target to produce the required phase history data needed to form an image of the targeted area [4]. Due to the radar movement requirements to produce a synthetic aperture, it is natural for these radars to be placed on mobile platforms such as airplanes and satellites [3].

1

There are many variations of SAR in existence; however, there are two main modes of SAR: stripmap and spotlight. Stripmap mode consists of the SAR antenna forming an image by maintaining its beam in a fixed position, illuminating a strip on the ground as it moves along the synthetic aperture, hence, the name stripmap. In spotlight mode, the SAR system slews its antenna beam to illuminate the same ground patch or target area, like a "spotlight," while the radar moves along its scheduled path [5]. The purpose of spotlight-mode SAR is to improve resolution at the expense of area coverage as compared to stripmap-mode SAR as mentioned in [6]. The use of the spotlight-mode SAR is the focus of this thesis, and simulations derived in [6] and [7] are utilized.

While use of synthetic aperture provides improvement to cross-range resolution of the radar, no improvements to range resolution are provided through synthesis of a larger aperture. Range resolution is solely determined by the bandwidth of the radar's transmitted signal [3]. Traditionally, radar systems have used linearly-frequency modulated (LFM) waveforms to increase range resolution. LFM waveforms use a phenomenon known as pulse compression to increase the range resolution [3], [5], and [8]. LFM signals use a sinusoidal pulse with either linearly increasing or decreasing frequency that varies over time. Frequency-modulated continuous wave (FMCW) is another example of a LFM waveform that uses both increasing and decreasing frequency over time, one following the other [1], [9]. The frequency modulation of the LFM waveform increases the bandwidth of a signal and increases the range resolution of the radar system due to the proportionality relationship between range resolution and signal bandwidth [10]. The ability of LFM signals to sharpen range resolution by increasing the signal's bandwidth make them desirable in high resolution radars such as SAR [5].

In this thesis, five specific polyphase, or phase-shift keyed (PSK), signals are investigated for potential use in a spotlight-mode SAR system: Frank, P1, P2, P3, and P4 codes. All five of these waveforms are characterized as a linear step approximation to LFM waveforms. The ability of these signals to conceal large bandwidths, maintain low autocorrelation side lobes, and be Doppler tolerant, make them ideal waveforms for use in synthetic aperture radar.

2

A.   PREVIOUS WORKS

Prior works done by Garren, Pace, and Romero [6] and [7], who investigated the use of low probability of intercept (LPI) modulation techniques for use in SAR imagery and, more specifically, spotlight SAR imagery provided the foundation for this research. In their work, a notional SAR radar capable of transmitting and receiving LPI signals and forming two-dimensional images was simulated. The signal types used were poly-phase sequences and include the Frank and P3 codes as the transmitted LPI waveforms. Garren, Pace and Romero demonstrated through simulation that both the Frank and the P3 codes are capable of producing SAR images [6], [7]. In this thesis we build on the work in [6] and [7] by reuse of the simulation scripts used to obtain results and adding the P1, P2 and P4 codes. The simulation scripts are referred to as the SAR Simulator for the remainder of this thesis.

B.   PURPOSE OF THESIS

The primary the focus of this thesis is to examine the range and cross-range sidelobe structure of the five PSK codes in an attempt to determine which of the five codes presents the best peak-to-sidelobe level (PSL) when used to generate SAR images in the SAR Simulator. The SAR Simulator is a collection of MATLAB scripts that were used to generate the results in [6], [7]. A secondary focus of this thesis is to analyze the three not previously studied poly-phase modulated signals for use in SAR for potential improvements in SAR LPI and to understand the resulting effects of the individual poly-phase signals on the SAR imagery.

A comparison of the five codes is conducted. The specific poly-phase codes studied include the Frank, P1, P2, P3 and the P4 codes. Simulated results are used to derive conclusions and no prototype builds or measured data are included.

The comparison of the codes is performed under the constraint that each of the individual poly-phase codes is held to the same subcode period and carrier frequency. The parameters allowed to vary are the number of subcodes and the number of consecutive codes sequences being transmitted and received. The varied parameters are compared "like to like," meaning the signals compared have the same number of

3

subcodes and consecutive codes sequences. Given the stated constraints, the SAR imagery is studied for each of the individual poly-phase codes for location of target return as compared to target truth and for peak-to-sidelobe level.

C.   THESIS ORGANIZATION

An overview of each chapter and its contents is provided herein. A brief introduction to signal representation and signal fundamentals used in this thesis is provided in Chapter II. This includes Fourier analysis, passband signal representation including I and Q signal formation concepts and matched filtering. The reader is familiarized with the five poly-phase codes used in this thesis in Chapter III. The codes are expressed mathematically from principles used in Chapter II, and each code and its parameters as they pertain to this study are discussed. A brief introduction to the basic principles of radar and range determination, followed by an introduction into spotlight SAR data collection, is presented in Chapter IV. The material in Chapter V is a detailed discussion of the SAR Simulator and how it is combined with a modified version of the LPI Tool Box provided in [9]. Also discussed are implementations of the signal processing for the SAR Simulator from [6] and [7]. The methodology for investigating the peak side lobe levels of the five PSK codes, the mathematics and the simulated results are discussed in Chapter VI. Finally, a summary of the research results and conclusions and recommendations for future works in this area of study are provided in Chapter VII.

II.   SIGNAL PROCESSING

The reader is provided with an introduction to signal formats and signal processing in this chapter in order to understand the mathematical principles used herein to describe the radar signals. A variety of signal processing techniques and terminology is needed to help the reader conceptually understand the mathematics used in SAR processing and the steps required to understand SAR image reconstruction

A.   RADAR SIGNALS

Signals are used as the medium for carrying location information from the radar target back to the radar. These signals can be represented in both continuous and discrete-time formats. In a real radar system, it is understood the radar transmits and receives continuous-time signals which are converted to discrete-time signals via an analog-to-digital converter (ADC) in the radar's receiver system [11]. The differences between continuous and discrete time for a given signal containing two sine waves sampled at 1.0 GHz is seen in Figure 1.
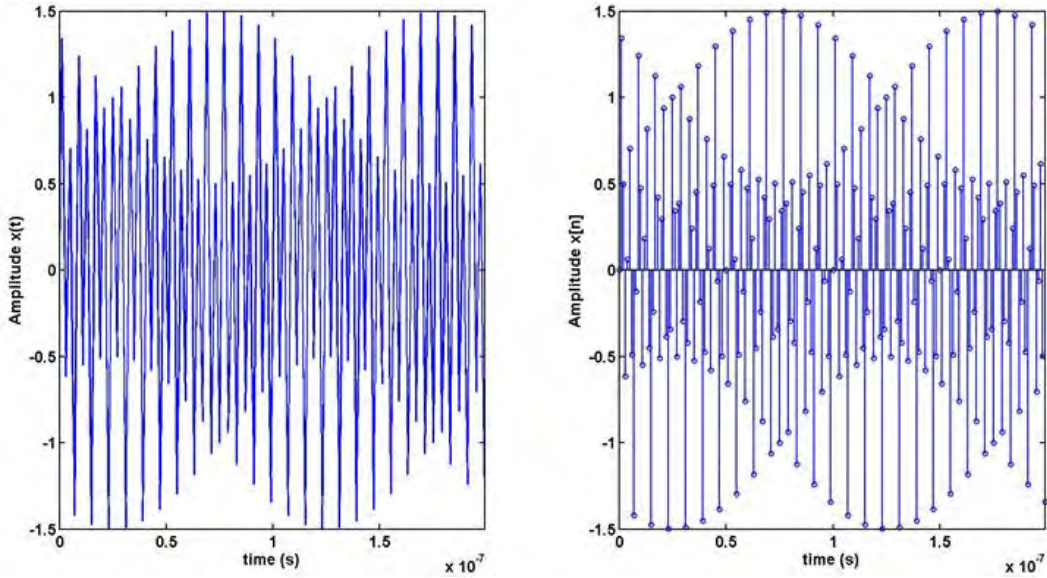
Figure 1.   Continuous and Discrete Time Comparison

Arbitrary signal in continuous time (left) and identical signal in discrete time (right).

The signals referenced in this thesis are observed in two signal domain forms: the discrete time domain and the frequency domain. Frequent transitions between the two domains occur throughout the processing of the SAR data collection and image reconstruction. Although the time-domain representation of the signals is discussed in this thesis for the poly-phase waveforms described in Chapter III, the frequency domain is the preferred domain in signal processing due to its computational efficiency [12]. The majority of the research for this thesis is performed via simulation, and it is important to show the mathematical process for time domain to frequency domain transformation and its inverse transformation. This concept of transforming from time domain to frequency domain and back again is used throughout this paper for both waveform manipulation and SAR processing. The following subsection is provided to assist the reader in the understanding of the Fourier transform principles.

B. FOURIER ANALYSIS

The Fourier transform is a mathematical method to translate a non-periodic or a periodic signal from the time domain to the frequency domain. The reverse process of going from the frequency domain to the time domain is known as the inverse Fourier transform. The discrete Fourier transform (DFT) is a method in signal and image processing for transforming discrete-time signals from the time domain to the frequency domain. Illustrated in Figure 2 is an example using the waveform from Figure 1 in the discrete time-domain and its spectrum in the frequency-domain. From the frequency domain plot, we see both sinusoidal tones from the signal $x[n]$ are clearly represented in the frequency spectrum.

Many SAR processing algorithms use some form of the DFT to perform this transformation in support of such measurements as range, cross-range, matched filtering, and image reconstruction. In this thesis the actual DFT is performed using the fast Fourier transform (FFT). The FFT is not another transform but instead is a mathematical manipulation of the DFT to improve computational efficiency; this concept is further discussed in [12].
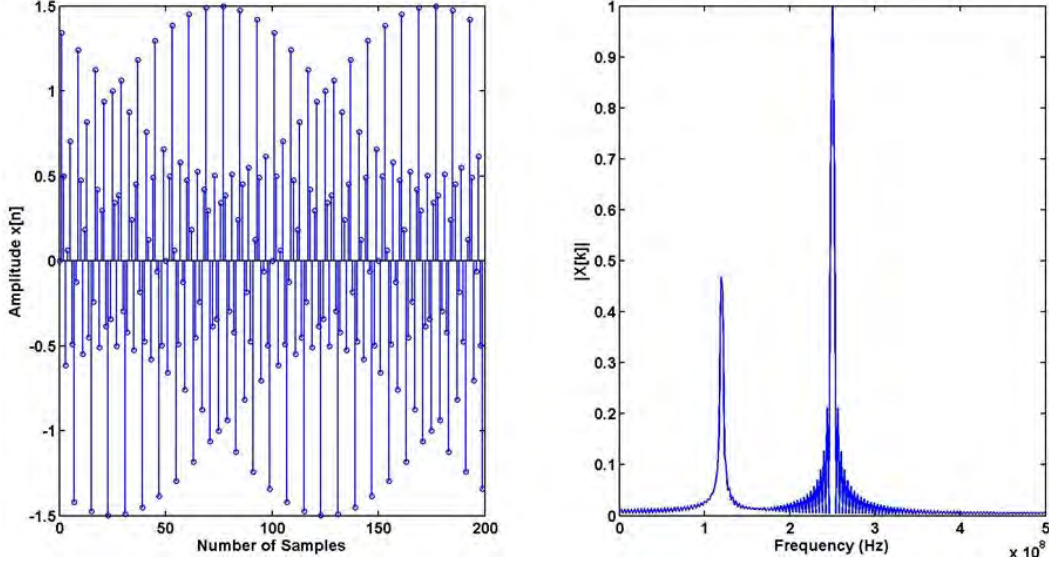
Figure 2.   Discrete Time-Domain and Frequency-Domain of an Arbitrary Signal

C.   PASSBAND SIGNAL REPRESENTATION AND TERMINOLOGY

The signals explored in this thesis can be expressed in two mathematical forms: the analytic and the complex envelope. The mathematical expressions of the complex exponential and its relation to the sinusoidal representation are introduced in this section. The identity describing the relationship between complex exponentials and sinusoids is Euler's identity, and is given by

$$e^{j\theta} = \cos(\theta) + j\sin(\theta). \qquad (1)$$

The cosine function is the real information of the complex exponential, and the sine function is the imaginary information. The variable θ is the argument of the two sinusoidal functions. Also seen from (1) is the relationship Euler's identity has with rectangular and polar formats, where the polar form is represented on the left hand side of (1), and the complex rectangular form is represented on the right as mentioned in [12]. This idea of the rectangular form leads to quadrature notation, which we apply to the poly-phase signals discussed in Chapter III. Before the quadrature notation is discussed, the concept of passband signaling is discussed and how it applies to poly-phase signals studied. A time-varying signal $x(t)$ is considered a passband signal if it has a nonzero

7

Fourier transform centered on a frequency ω_c. A visual representation of a passband signal is illustrated in Figure 3.
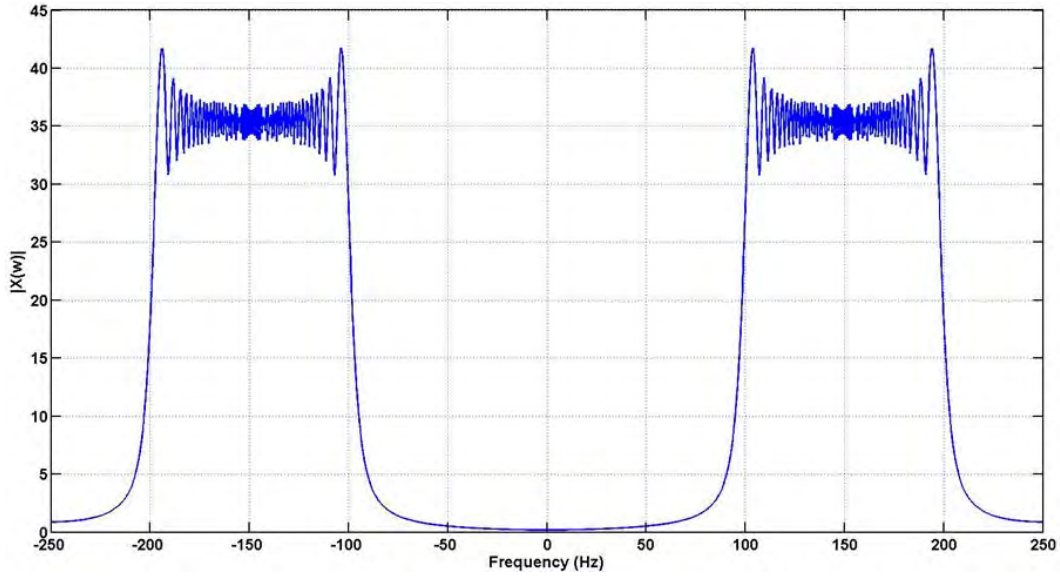
Figure 3.   Double-sided FFT of a LFM Waveform

The frequency response of a passband signal in the form of a LFM waveform with a 100-Hz bandwidth.

Passband signals are complex signals characterized by either the amplitude modulation $A(t)$, phase modulation $\phi(t)$, or both of a time-varying sinusoidal waveform with a carrier frequency of ω_c [13]. The mathematical representation of a passband signal is given by [12]

$$x(t) = A(t)\cos(\omega_c t + \phi(t)). \tag{2}$$

Here, t represents the time variable of the signal. In this thesis the phase modulation in (2) is used while $A(t)$ is held constant and is normalized to one.

D.   INPHASE AND QUADRATURE REPRESENTATION OF PASSBAND SIGNALS

Quadrature notation is a mathematical method for breaking down a complex waveform into its modulated signal and its carrier. The modulated signal is described by an inphase component I and a quadrature component Q. The decomposition of a complex waveform can be performed by applying the sum-difference trigonometric

8

identity and equating the result to (2). This decomposition process of the complex waveform yields

$$A(t)\cos(\omega_c t + \phi(\text{t})) = A(t)\cos(\omega_c t)\cos(\phi(\text{t})) - A(t)\sin(\omega_c t)\sin(\phi(\text{t})).$$ (3)

This is further discussed in [14]. By recognizing the carrier terms $cos(\omega_c t)$ and $sin(\omega_c t)$ in (3), we can substitute for the two quadrature terms, I for the $cos(\phi t)$ term and Q for the $sin(\phi t)$ term to get, respectively,

$$I(t) = A(t)\cos(\phi(t)),$$

and (4)

$$Q(t) = A(t)\sin(\phi(t)),$$

where $I(t)$ and $Q(t)$ are the two orthogonal, time-varying vectors describing the complex waveform. Substituting (4) into (3), we get the quadrature notation of the complex waveform as [14]

$$A(t)\cos(\omega_c t + \phi(t)) = I(t)\cos(\omega_c t) - Q(t)\sin(\omega_c t).$$ (5)

Quadrature notation allows for quick understanding of a complex signal. From the right side of (5), the baseband signal can be found by removing the sinusoidal carrier components $cos(\omega_c t)$ and $sin(\omega_c t)$ [13]:

$$p(t) = I(t) + jQ(t).$$ (6)

The notation shown in (6) is used in Chapter III and throughout this thesis to describe the poly-phase signals at baseband. IQ notation is preferred for complex waveforms because it allows for an easy mathematical representation of the signal.

E.   MATCH FILTERING

Matched filtering plays a major role in modern radars. Levanon describes in [15] that a radar functions by using the reflected energy from distant objects to determine the presence of targets in space. He continues by explaining that the probability of detection is determined by the signal-to-noise ratio (SNR) and not the exact waveform of the signal received; hence, maximizing the SNR versus preserving the signal shape is advantageous for detection of echoed pulses. A matched filter is defined as "a linear filter whose impulse response is determined by a specific signal in a way that will result in the maximum attainable SNR at the output of the filter when that particular signal and white

noise are passed through the filter" [15]. Using the simple block diagram shown in Figure 4, Levanon shows through the use of the Fourier transform and the Schwarz inequality that the matched filter response $h(t)$ for a given signal $s(t)$ is described by

$$h(t) = Ks^*(t_0 - t). \tag{7}$$

From (7) we see that the matched filter is the delayed, time-reversed conjugate of the signal $s(t)$, where K is an arbitrary weighting function [15]. This is used in later chapters when matched filters are used in simulation to generate target detections for SAR imaging.
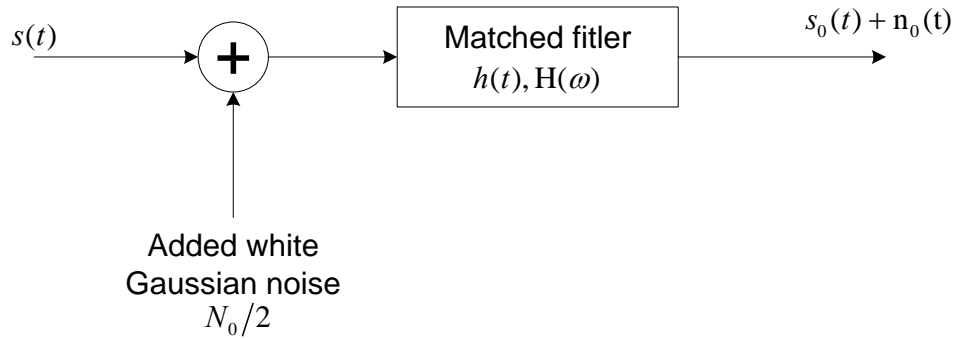
Figure 4.　　Block Diagram Depicting the Matched Filter Definitions

Adapted from [15]: N. Levanon and E. Mozeson, *Radar Signals*, Hoboken, NJ: John Wiley & Sons, Inc., 2004.

In this chapter we built a theoretical understanding of the signal processing used in this thesis. The Fourier and inverse Fourier transforms were introduced, as were the ideas of quadrature notation and matched filtering. The poly-phase signals used in this study and a background on the individual signals are discussed in the next chapter.

III. POLYPHASE SIGNALS

The history of each of the PSK codes is discussed in this thesis. Also discussed and explained in this chapter is the theoretical side lobe structure from the autocorrelation function for each of the PSK codes. Plots are provided in multiple domains to help with familiarization of the signals for the reader and to help in explaining the limitations of the signals. As mentioned in Chapter I, the five PSK Signals used in this thesis are the Frank code, P1, P2, P3, and P4 codes.

All five of the PSK modulations have very similar parameters. These parameters are number of subcodes N_c, subcode period t_b, code period T, cycles per subcode cpp, and the number of samples per subcode b_{sc}. These variables are defined in [9] and recreated here for convenience. The number of subcodes is defined by the number of elements in the poly-phase code. For example, a 16-element Frank code has $N_c = 16$. The subcode period is defined by the inverse of the required bandwidth B of the signal; i.e., $t_b = 1/B$. Once the number of subcodes N_c and the subcode period t_b is defined, the code period is defined as

$$T = N_c t_b. \tag{8}$$

The cycles per subcode is calculated by multiplying the carrier frequency f_c with the subcode period of the signal:

$$cpp = f_c t_b. \tag{9}$$

Finally, multiplying (9) by the ratio of the sample frequency f_s to the carrier frequency f_c, we define the number of samples per subcode as

$$b_{sc} = cpp \frac{f_s}{f_c}. \tag{10}$$

Other characteristics polyphase codes share are processing gain PG_R and unambiguous range R_u. For polyphase codes, the processing gain can also be defined by the ratio of the code period and the subcode period [9]

$$PG_R = T \left(1/t_b \right). \tag{11}$$

Substituting (8) into (11), we get

$$PG_R = N_c t_b \left(1/t_b\right) = N_c.$$ (12)

Here, we find that the processing gain for polyphase codes is equivalent to the number of subcodes in the code sequence [9].

A.   FRANK CODE

1.   History

The Frank code was developed by R.L. Frank and Zadoff in 1963 [15]. The Frank code is characterized as a linear-step approximation to a frequency-stepped pulse and is defined by using a discrete number of frequency steps and a discrete number of phase samples per frequency. These frequency steps and phase samples create a discrete phase history of a LFM signal. The number of frequency steps and phase samples are required to be equal for the Frank code. This requirement presents a limitation on the use of the Frank code, since the code is only able to represent signals with code lengths $N_c = L^2$ [15].

The Frank code was initially described with the discrete Fourier transform where the elements are shown in the matrix shown in Figure 5. The matrix is used to construct a Frank code by calculating each of the coefficients in the matrix for a given L and then multiplying each of the coefficients by $2\pi/L$ to generate the required phase history. The rows of the matrix are then concatenated together from top to bottom, generating the phase-shifted sequence for the prescribed Frank code. Building the Frank code in this manner is known as the construction method [15].

2.   Mathematical Discussion

An example of the construction method for a 64-element Frank code is demonstrated in this section. The first step in creating the Frank code is to generate the required matrix described by Figure 5. For $L = 8$ the matrix of Figure 5 is used to create the 64 elements for the desired Frank code. This first step results in the matrix displayed in Figure 6. The results of Figure 6 are then multiplied by the required phase adjustment $2\pi / 8$ of the 64 element Frank code. This generates the phase shift matrix $\phi(n,k)$ of the Frank code seen in Figure 7 and describes the phase-shift history of the 64-subcode

12

periods. The rows of the matrix in Figure 7 are then concatenated together to generate a 64-element vector defining the Frank code phase-shift sequence.

We can also define a Frank-coded modulation mathematically by [15]

$$\phi(n,k) = \frac{2\pi}{L}(n-1)(k-1), \quad 1 \le n \le L, \quad 1 \le k \le L. \tag{13}$$

Equation (13) allows for easy access to any element of any size Frank code without the generation of the matrix needed for the construction method.

$$\begin{bmatrix} 0 & 0 & 0 & \cdots & 0 \\ 0 & 1 & 2 & \cdots & L-1 \\ 0 & 2 & 4 & \cdots & 2(L-1) \\ \vdots & \vdots & \vdots & \ddots & \vdots \\ 0 & L-1 & 2(L-1) & \cdots & (L-1)^2 \end{bmatrix}$$

Figure 5.   Fourier Coefficients Matrix Defining the Elements of the Frank Code

Adapted from [15]: N. Levanon and E. Mozeson, *Radar Signals*, Hoboken, NJ: John Wiley & Sons, Inc., 2004.

$$\begin{bmatrix} 0 & 0 & 0 & 0 & 0 & 0 & 0 & 0 \\ 0 & 1 & 2 & 3 & 4 & 5 & 6 & 7 \\ 0 & 2 & 4 & 6 & 8 & 10 & 12 & 14 \\ 0 & 3 & 6 & 9 & 12 & 15 & 18 & 21 \\ 0 & 4 & 8 & 12 & 16 & 20 & 24 & 28 \\ 0 & 5 & 10 & 15 & 20 & 25 & 30 & 35 \\ 0 & 6 & 12 & 18 & 24 & 30 & 36 & 42 \\ 0 & 7 & 14 & 21 & 28 & 35 & 42 & 49 \end{bmatrix}$$

Figure 6.   Fourier Transform Coefficients for a 64-element Frank Code

$$\phi_{n,k} = \begin{bmatrix} 0 & 0 & 0 & 0 & 0 & 0 & 0 & 0 \\ 0 & \dfrac{2\pi}{8} & \dfrac{4\pi}{8} & \dfrac{6\pi}{8} & \dfrac{8\pi}{8} & \dfrac{10\pi}{8} & \dfrac{12\pi}{8} & \dfrac{14\pi}{8} \\ 0 & \dfrac{4\pi}{8} & \dfrac{8\pi}{8} & \dfrac{12\pi}{8} & \dfrac{16\pi}{8} & \dfrac{20\pi}{8} & \dfrac{24\pi}{8} & \dfrac{28\pi}{8} \\ 0 & \dfrac{6\pi}{8} & \dfrac{12\pi}{8} & \dfrac{18\pi}{8} & \dfrac{24\pi}{8} & \dfrac{30\pi}{8} & \dfrac{36\pi}{8} & \dfrac{42\pi}{8} \\ 0 & \dfrac{8\pi}{8} & \dfrac{16\pi}{8} & \dfrac{24\pi}{8} & \dfrac{32\pi}{8} & \dfrac{40\pi}{8} & \dfrac{48\pi}{8} & \dfrac{56\pi}{8} \\ 0 & \dfrac{10\pi}{8} & \dfrac{20\pi}{8} & \dfrac{30\pi}{8} & \dfrac{40\pi}{8} & \dfrac{50\pi}{8} & \dfrac{60\pi}{8} & \dfrac{70\pi}{8} \\ 0 & \dfrac{12\pi}{8} & \dfrac{24\pi}{8} & \dfrac{36\pi}{8} & \dfrac{48\pi}{8} & \dfrac{60\pi}{8} & \dfrac{72\pi}{8} & \dfrac{84\pi}{8} \\ 0 & \dfrac{14\pi}{8} & \dfrac{28\pi}{8} & \dfrac{42\pi}{8} & \dfrac{56\pi}{8} & \dfrac{70\pi}{8} & \dfrac{84\pi}{8} & \dfrac{98\pi}{8} \end{bmatrix}$$

Figure 7.   Coefficient Matrix of the 64-element Frank Code

3.   Frank Code Simulations

To implement the Frank code, (13) was used to generate the phase-state matrix of the Frank code [15]. The matrix $\phi(n,k)$ was then manipulated into a vector $\phi(m)$ by creating an indexing variable m such that $m = L(n-1)+k$:

$$\phi(n,k) = \sum_{n=1}^{L}\sum_{k=1}^{L}\frac{2\pi(n-1)(k-1)}{L}, \tag{14}$$

$$\phi(m) = \sum_{n=1}^{L}\sum_{k=1}^{L}\frac{2\pi(n-1)(k-1)}{L}. \tag{15}$$

This manipulation performs the concatenation process of the construction method previously discussed. The reason for putting the sequence into a vector form is that it allows for removal of unnecessary "for loops" in simulation code due to the removal of one of the indexing variables.

Once the Frank-coded phase vector is created, the IQ signal generation discussed in Chapter II was used to generate a Frank-code phase modulated signal. This was done with

$$I(n) = A\cos\left(2\pi f_c (n-1) t_s + \phi(m)\right),\tag{16}$$

$$Q(n) = A\sin\left(2\pi f_c (n-1) t_s + \phi(m)\right),\tag{17}$$

and

$$s(n) = I(n) + jQ(n).\tag{18}$$

Here, variable f_c is the carrier frequency, n is the sample number, t_s is the sample period and A is the amplitude of the sinusoid.

a.   *Frank Code Phase Shift*

Plotting the phase variable $\phi(m)$ over the number of indices leads to Figure 8. For convenience the *x*-axis of Figure 8 is incremented in steps of eight so that each of the rows of the Frank coded matrix from Figure 7 can be identified. Each of the individual "staircases" represents a row of the matrix. The first staircase is flat because the first row of the matrix is all zeros, as seen in Figure 7. The next seven rows of the matrix all make phase changes to the carrier signal as displayed in Figure 8. We see that each row of the matrix has an increased amount of phase shift relative to the previous row of the matrix. This is in agreement with the definition of the Frank coded matrix shown in Figure 5. This visible increase in phase shift from row to row of the matrix creates the stepped chirp, or linear-frequency modulation (LFM), that the Frank code is known for. This 'chirp' phenomenon is visible in Figure 8 through the increasing phase slopes of each of the staircases. An increase in phase change slope directly correlates to an in increase in frequency of the signal because frequency is the first time derivative of phase; therefore, a change in slope represents a change in frequency. This change in frequency is visible in the time-domain plots in the next section.
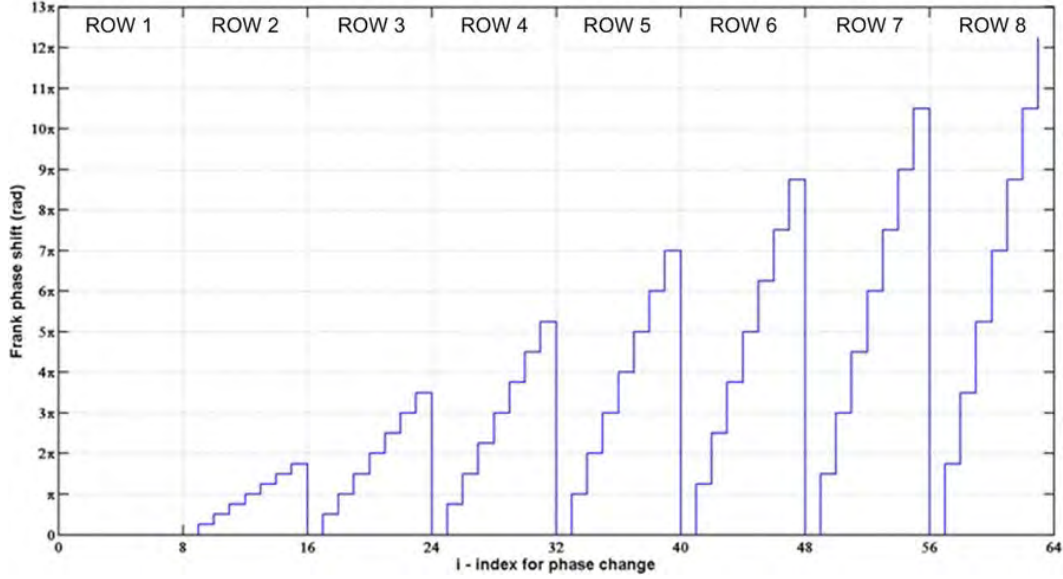
Figure 8.   Frank Coded 64-Element Phase Shift

The phase shift for each subcode period of the of the 64-element Frank-coded sequence. Adapted from [9]: P. E. Pace, *Detecting and Classifying Low Probability of Intercept Radar*, 2nd ed., Norwood, MA: Artech House, 2009.

b.   *Time-Domain Plots of the Frank Code Applied to a Carrier Signal*

In this section the time domain of the Frank code is discussed and displayed. The following graphs were created by plotting (18) over time for both $\phi(m) = 0$ and for $\phi(m)$ defined by (15). The top graph in Figure 9 is an amplitude plot of (18) over time with no modulation applied. A clean sinusoid signal, which is expected, is shown. The frequency of the sinusoid is 150 MHz. This sinusoidal signal is the carrier to which the Frank-code modulation is applied. The resultant waveform of the applied modulation is displayed in the bottom plot of Figure 9. It is also clear from the bottom plot of Figure 9 why the Frank code is characterized as a linear-step approximation to a frequency-stepped pulse. We can see that the time between successive peaks decreases from the left-hand side of the plot as time move towards the right-hand side. The decreasing time between signal peaks represents a frequency increase from the left-hand side of the plot to the right.

16
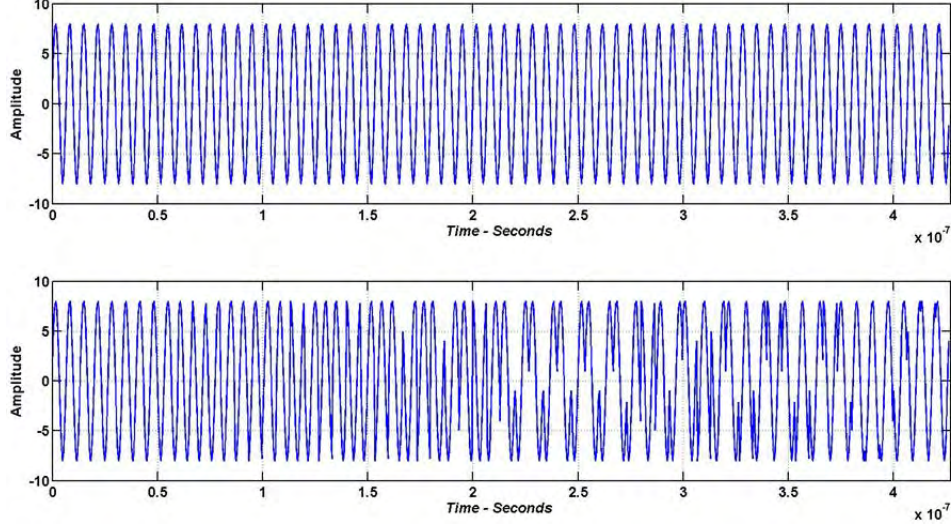
Figure 9.   Sinusoidal Carrier Compared to Frank Coded Modulation

Time-domain representation of the 150-MHz sinusoidal carrier (top) and the Frank coded modulation on the 150-MHz carrier (bottom). Adapted from [9]: P. E. Pace, *Detecting and Classifying Low Probability of Intercept Radar*, 2nd ed., Norwood, MA: Artech House, 2009.

c.   *Autocorrelation Function*

The autocorrelation function (ACF) is defined by Levanon as [15]

$$\left| R(\tau) \right| = \left| \int_{-\infty}^{\infty} u(t) u^*(t+\tau) \, dt \right|, \tag{19}$$

where, $R(\tau)$ denotes the autocorrelation of $u(t)$, $u(t)$ is the correlation reference and $u^*(t+\tau)$ is the conjugated, time-delayed version of $u(t)$. Converting (19) from continuous time to discrete time, we find:

$$\left| R[n] \right| = \left| \sum_{m=-\infty}^{\infty} u[m] u^*[m+n] \right|, \tag{20}$$

where m replaces t as the time index and n replaces τ as the delay variable. Inserting (15) into (16) and (17) and the results into (18), we get the Frank code signal $s(n)$. By inserting $s(n)$ for $u[m]$ and $s^*(m+n)$ for $u^*[m+n]$ into (20) and graphing the result, Figure 10 is created. The x-axis of the plots is defined by the number of samples per subcode multiplied by the number of subcodes of the signal. The y-axis is the energy of the signal normalized to the energy peak of the mainlobe. For this example, we took 16 samples per

17

subcode, and the Frank code had 64 elements. As a result, we expect the *x*-axis to extend to 1024 samples as displayed in Figure 10.

Figure 10.   Single Reference Frank Code ACF

ACF of the 64-element Frank modulated signal with $N = 1$. Adapted from [9]: P. E. Pace, *Detecting and Classifying Low Probability of Intercept Radar*, 2nd ed., Norwood, MA: Artech House, 2009.

The importance of the plot of the ACF is that it predicts the shape of the energy spectrum at the output of the matched filter when a matched signal is passed through the filter [15]. The filter magnitude response *K* from (7) can be weighted to cause different effects on the output of the filter, however, in this thesis we use the unweighted filter such that $K = 1$. From Figure 10, we see the mainlobe and sidelobe response of the matched filter for the 64-element Frank code. This tells us that other signal returns with nearby delays being passed through the matched filter need to have enough energy to overcome the sidelobe response of the filter output. This issue is also discussed in [15]. In the case of the 64-element Frank code with number of references $N = 1$, the *PSL* level is approximately −27.8 dB as seen in Figure 10. This modeled output of the *PSL* matches well with the expected theoretical response defined in the next section.

d. Frank Code Matched Filter Sidelobe Structure

From Figure 10, we see that the ACF of the Frank coded signal has a low *PSL* ratio of approximately 28 dB. This is explained theoretically by the definition of the *PSL* from [9]

$$PSL = 20\log_{10}\left(\frac{1}{NL\pi}\right). \tag{21}$$

In (21) the variable N is the number of reference waveforms the matched filter uses, and the variable L is the square root of the number of elements in the Frank code. In this chapter, we use the example of a 64-element Frank code where $L = 8$. In this case, from (21) we find the theoretical $PSL = -28$ dB.

As seen in (21), the *PSL* can be improved by increasing the number of reference waveforms in the matched filter as shown in Figure 11. A plot of the ACF, where the number of reference waveforms is four, is depicted in Figure 11, where we see that the *PSL* has dropped to approximately $PSL = -39.8$ dB. This result is a 12 dB difference from the single-reference waveform shown in Figure 10. Because the Frank code has a large *PSL* in the ACF, it should be a good candidate for SAR imaging. This characteristic has been demonstrated in [6] and [7].
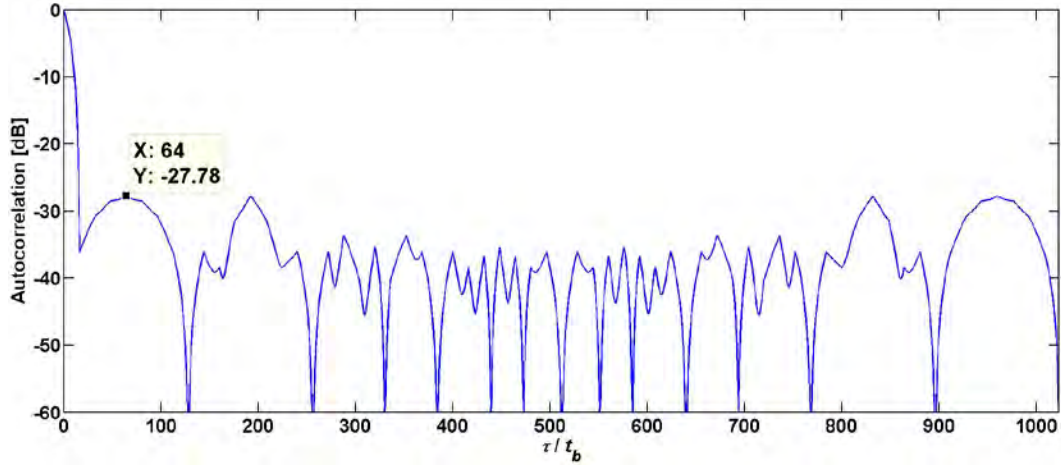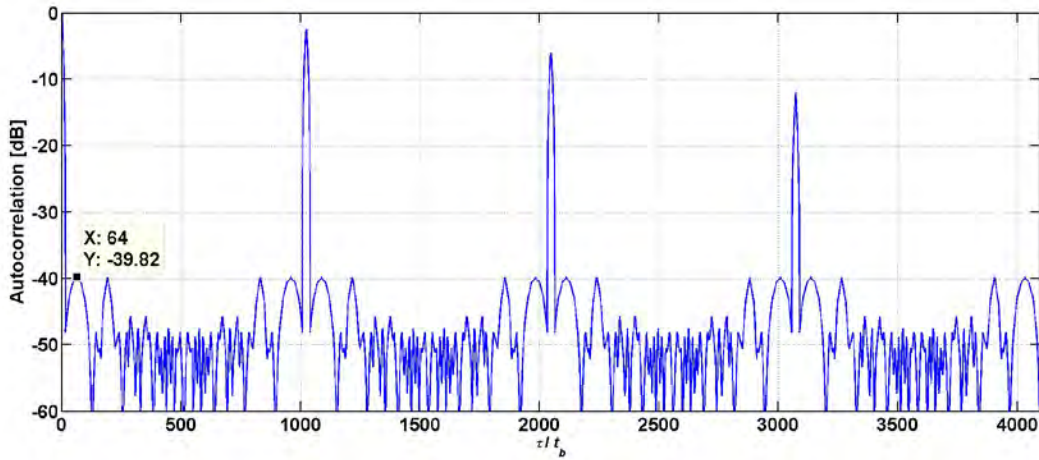

Figure 11.   Multiple Reference Frank Code ACF

ACF of the 64-element Frank modulated signal with $N = 4$. Adapted from [9]: P. E. Pace, *Detecting and Classifying Low Probability of Intercept Radar*, 2nd ed., Norwood, MA: Artech House, 2009.

B. P1 AND P2 CODES

1. History

The P1 and P2 codes were derived from the Frank code in 1981 by Lewis and Kretschmer [15]. Both the P1 and P2 codes are linear step approximations to a LFM waveform just as the Frank code is. The P1 and P2 codes are also limited to the number of subcodes being perfect squares, like the Frank code. The P2 code has another limitation in that it is only valid for L even [15]. One of the differences between the Frank and the P1 and P2 codes is that the P1 and P2 codes place the smaller phase shift values at the center of the code sequence and the larger phase change values at the ends of the code. The difference between the P1 and P2 codes is where each code starts its phase shift [9]. These differences can be seen in a comparison of Figure 12 and Figure 13.

2. Mathematical Discussion

The P1 and P2 codes like the Frank code can be implemented using the construction method discussed in detail earlier in the Frank code section of this chapter. In this section, we will only look at the equations that define the phase matrix of the P1 and P2 codes and not actually go through the step-by-step process of the construction method. The definition of the P1 and P2 codes are given by [15]:

$$\phi(n,k) = \frac{2\pi}{L}\left[(L+1)/2 - n\right]\left[(n-1)L + (k-1)\right], \quad 1 \le n \le L, \quad 1 \le k \le L, \text{ (22)}$$

$$\phi(n,k) = \frac{2\pi}{L}\left[(L+1)/2 - n\right]\left[(L+1)/2 - k\right], \quad 1 \le n \le L, \quad 1 \le k \le L, \quad L \text{ even}. \text{ (23)}$$

In a comparison of (22) and (23), the two codes are very similar mathematically and only differ in the second square bracket term. These two phase history matrix equations are then modified to create a phase history vectors just as we did for the Frank code. As mentioned in the Frank code section the conversion from phase history matrix definition to a phase history vector was made to remove a "for loop" for the complex signal generation thereby decreasing the simulation time to generate the signal.

3.   P1 and P2 Code Simulations

To implement the P1 and P2 code, (22) and (23) were modified into summation form to create their respective phase-state matrices $\phi(n,k)$. Both (22) and (23) were then manipulated into a vector form by again creating the indexing variable m such that to generate the phase vector $\phi(m)$ of the P1 and P2 codes, respectively,

$$\phi(m) = \sum_{n=1}^{L} \sum_{k=1}^{L} \frac{2\pi \left[(L+1)/2 - n \right] \left[(n-1)L + (k-1) \right]}{L}, \qquad (24)$$

and

$$\phi(m) = \sum_{n=1}^{L} \sum_{k=1}^{L} \sum_{k=1}^{L} \frac{2\pi \left[(L+1)/2 - n \right] \left[(L+1)/2 - k \right]}{L}. \qquad (25)$$

This mathematical manipulation performs the concatenation process of the construction method, allowing for simplification in the signal generation.

a.   *Phase versus Phase Index*

In the following section, phase plots of the P1 and P2 codes are presented. Figure 12 and Figure 13 were created by plotting the phase variable $\phi(m)$ over the entire code sequence of the P1 and P2 codes. Just as in the Frank code, each of the individual "staircases" represents a row of the phase matrix, meaning that every eight indices in the figure is a new row of the phase matrix for this 64-element example.

Figure 12.   P1 Coded 64-Element Phase Shift

Phase shift for each subcode period of the P1 coded 64-element sequences. Adapted from
[9]: P. E. Pace, *Detecting and Classifying Low Probability of Intercept Radar*, 2nd ed.,
Norwood, MA: Artech House, 2009.

From Figure 12, we see that the P1 code initially has an increasing slope that steadily declines as the code index increases to the center, or mid-way, through the code sequence. Once the index passes the mid-way point, the slope of the phase becomes negative, and the slope of the phase increases as the code is indexed through to the end. Another observation is that the phase staring point between rows is larger as the P1 code is indexed from start to finish. This differs from the Frank code, where each row began its phase change from the zero-phase state. Like the Frank code, the P1 code's phase slope changes over the full sequence of the signal, thereby creating the step approximation to a linear-frequency modulation [9].

From Figure 13 we see that the P2 code also has a slope that steadily flattens as the code index increases to the center, or mid-way, through the code sequence. This is similar to the P1 code, however, the P2 code starts with a negative phase slope at the beginning of the code sequence, whereas the P1 code starts with a positive phase slope. Just as in the case of the P1 code, once the index passes the mid-way point, the slope of the phase changes sign and becomes steeper. We also see from Figure 13 that the slope of

22

the phase increases as the code is indexed from the midpoint through to the end of the sequence. Again, the phase starting point for each of the rows in the phase matrix is non zero like the P1 code. An interesting observation from Figure 13 is that the phase states of the P2 code are palindromic, meaning the signal is symmetric about its center as defined in [15]. Like the Frank and P1 codes, the P2 code's phase slope changes over the full sequence of the signal, thereby creating a step approximation to a linear-frequency modulation.
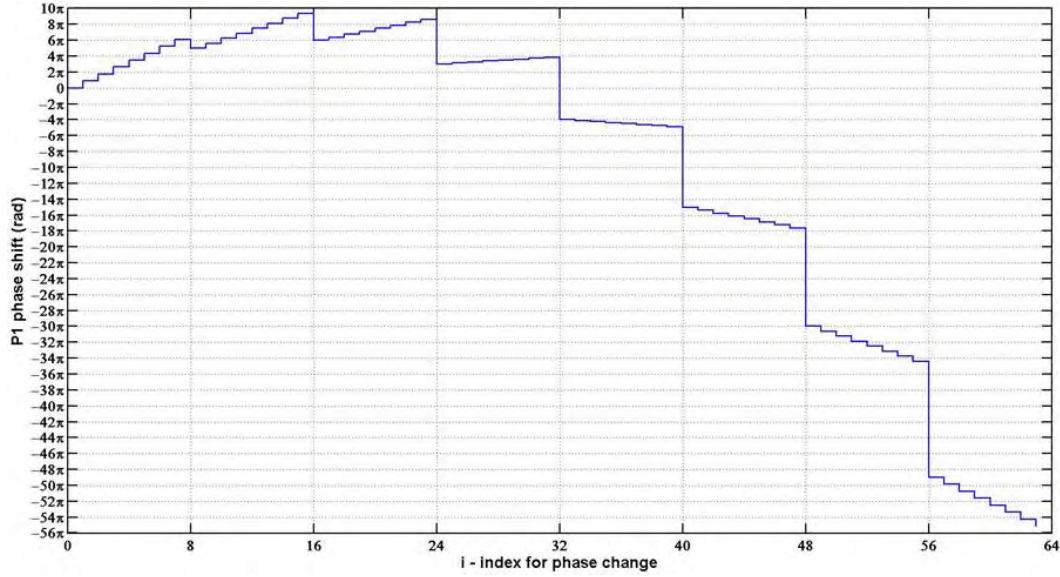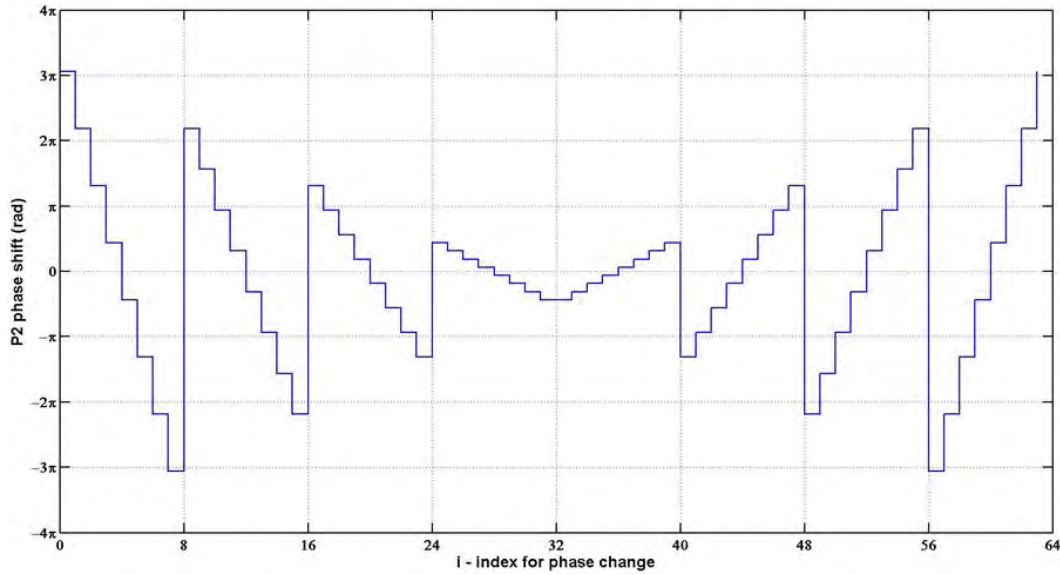

Figure 13.   P2 Coded 64-Element Phase Shift

Phase shift for each subcode period of the P2 coded 64-element sequence. Adapted from [9]: P. E. Pace, *Detecting and Classifying Low Probability of Intercept Radar*, 2nd ed., Norwood, MA: Artech House, 2009.

b.   Time-Domain Plots

In this section, the time domain of the P1 and P2 codes are discussed and plots of the modeled waveforms are presented. The following graphs were created by inserting the results of (16) and (17) into (18) for $\phi(m) = 0$ to generate the carrier waveform and $\phi(m)$ equal to (24) or (25) to either create the P1 or the P2 modulated waveform, respectively. The signals created from (18) for either the P1 or P2 codes were then plotted over time to create Figure 14 and Figure 15, respectively.

23

The time-domain plot for the P1 code is displayed in Figure 14. The sinusoidal carrier without modulation is shown in the top plot, and the carrier with the P1 modulation applied is shown in the bottom. The frequency of the sinusoid is 150 MHz, just as in the case of the Frank code. As mentioned in the previous section, we are able to see from the second plot of Figure 14 why the P1 code is characterized as a linear-step approximation to a LFM waveform by looking at the change in time between successive peaks as the time index increases.

The time-domain plot for the P2 code is displayed in Figure 15. The sinusoidal carrier without modulation is shown in the top plot, and the carrier with the P2 modulation applied is shown in the bottom plot. The frequency of the sinusoid is again set to 150 MHz to keep all the waveforms in this thesis comparable. Just as in the previous section, we are able to see from the second plot of Figure 15 that the P2 code also has a change in time between successive peaks as the time index increases, giving the P2 code its characterization as a linear step approximation to a LFM waveform.
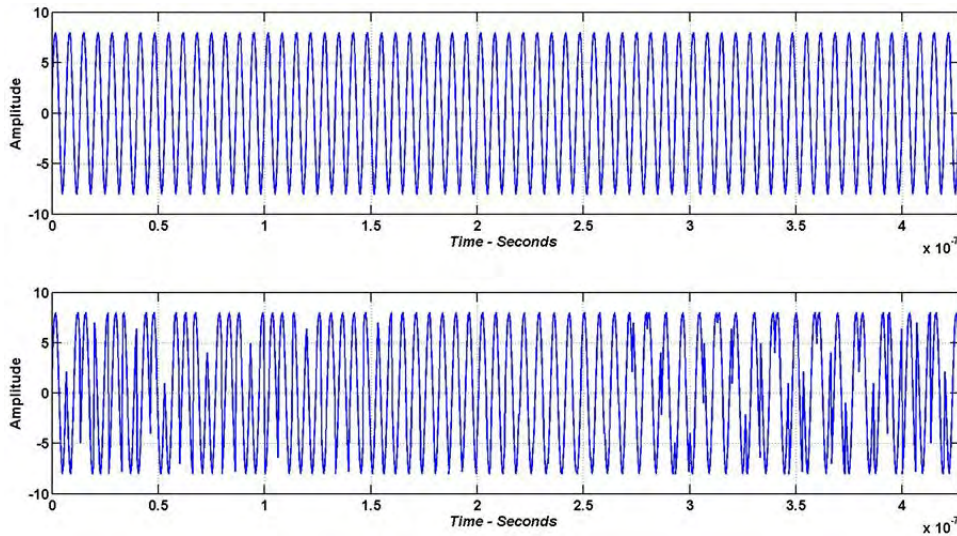
Figure 14.   Sinusoidal Carrier Compared to P1 Coded Modulation

Time-domain representation of the 150-MHz sinusoidal carrier (top) and the P1 coded modulation on the 150-MHz carrier (bottom). Adapted from [9]: P. E. Pace, *Detecting and Classifying Low Probability of Intercept Radar*, 2nd ed., Norwood, MA: Artech House, 2009.
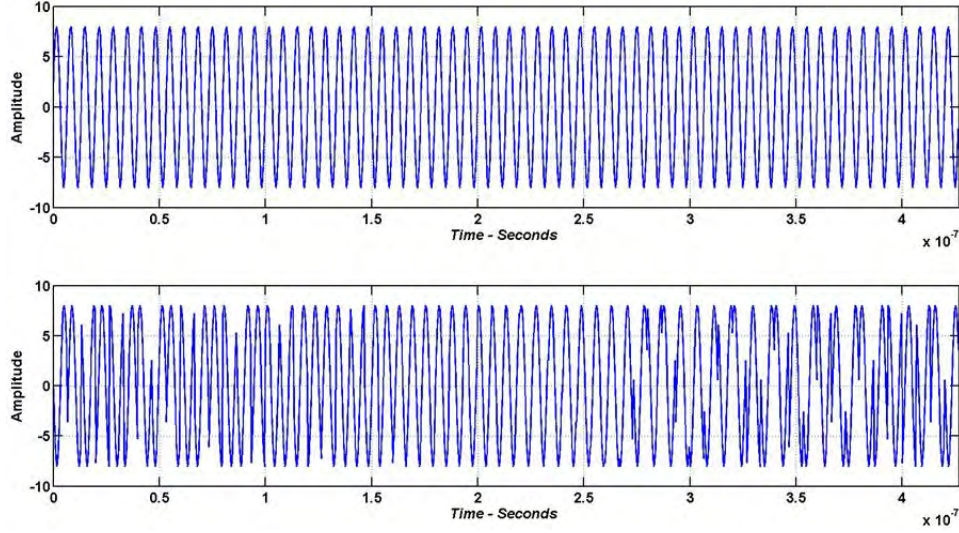
Figure 15.   Sinusoidal Carrier Compared to P2 Coded Modulation

Time-domain representation of the 150-MHz sinusoidal carrier (top) and the P2 coded modulation on the 150-MHz carrier (bottom). Adapted from [9]: P. E. Pace, *Detecting and Classifying Low Probability of Intercept Radar*, 2nd ed., Norwood, MA: Artech House, 2009.

c.   *Autocorrelation Function*

Graphs of the ACF for the P1 and P2 codes are displayed in this section. These graphs were created using the same approach as in the Frank code section. The phase state vector $\phi(m)$ was inserted into (16) and (17), and the results were used in (18), yielding $s(n)$. The results of (18) were used in (20) to generate the ACF. Again, the *x*-axis of the plot is defined as the number of samples per subcode multiplied by the number of subcodes in the signal. The *y*-axis is the energy of the signal normalized to the energy peak of the mainlobe. For this example the signal models are captured using 16 samples per subcode and both the P1 and P2 codes each use 64 elements; therefore, it is expected that the *x*-axis extend to 1024 samples, as seen in Figure 16 and Figure 17.

For the ACF from Figure 16, we see the mainlobe and sidelobe response of the matched filter for the 64-element P1 code. This tells us that other signal returns with nearby delays passed through the matched filter must have enough energy to overcome the sidelobe response of the P1 codes ACF [15]. In the case of the 64-element P1 code

25

with $N = 1$ as seen in Figure 16, the *PSL* level is approximately −27.8 dB, which is equal to that of the Frank code.

Figure 16.   Single Reference P1 Code ACF

ACF of the 64-element P1 modulated signal with $N = 1$. Adapted from [9]: P. E. Pace, *Detecting and Classifying Low Probability of Intercept Radar*, 2nd ed., Norwood, MA: Artech House, 2009.

Figure 17.   Single Reference P2 Code ACF

ACF of the 64-element P2 modulated signal with $N = 1$. Adapted from [9]: P. E. Pace, *Detecting and Classifying Low Probability of Intercept Radar*, 2nd ed., Norwood, MA: Artech House, 2009.

The P2 code also has a *PSL* = −27.8 dB for *N* = 1, as seen in Figure 17; however, we know that this worsens as the number of reference waveforms increases [9]. This modeled output of the *PSL* for the P1 and the P2 codes matches well with the expected theoretical response explored in the next section.

d.   Sidelobe Structure

As was shown in the previous section, the ACF of the P1 coded signal has a low *PSL* ratio of approximately 28 dB, just as with the Frank code. This is explained theoretically because the P1 code and the Frank code share the same equation that defines their respective peak sidelobe levels. As in the case of the Frank code the P1 code was modeled with a 64-element code with *L* = 8. When this is applied to (21), we find the theoretical *PSL* = −28 dB for the P1 code with *N* = 1. This result confirms the *PSL* shown in Figure 16.

We again apply (21) to the P1 code with *L* = 8, but this time with *N* = 4. We find that *PSL* = −40 dB in this case. The ACF of the P1 code was then modeled with the *L* and *N* parameters as mentioned above. As can be seen in Figure 18, the modeled *PSL* is in agreement with the theoretical *PSL*. As seen in (21) and shown in Figure 18, the *PSL* of the P1 code ACF can be improved by increasing the number of reference waveforms *N* in the matched filter. The capability for the P1 code to have an ACF with low *PSL* makes it a good candidate for use in a SAR system [9], [3].

The P2 code does not have the same *PSL* equation as the Frank and P1 codes. The *PSL* of the P2 code is [9]

$$PSL = 20\log_{10}\left(\frac{1}{L\pi}\right). \tag{25}$$

We see that the P2 code does not benefit from an increase in number of reference waveforms *N* as the Frank and P1 codes did. In fact, from a comparison of the ACF plot in Figure 17 and Figure 19, we see that the *PSL* actually increases in the ACF as the number of reference waveforms increase. This worsening *PSL* in the P2 codes ACF for an increase in *N* may cause it to generate false images in the SAR image formation due to large sidelobes.
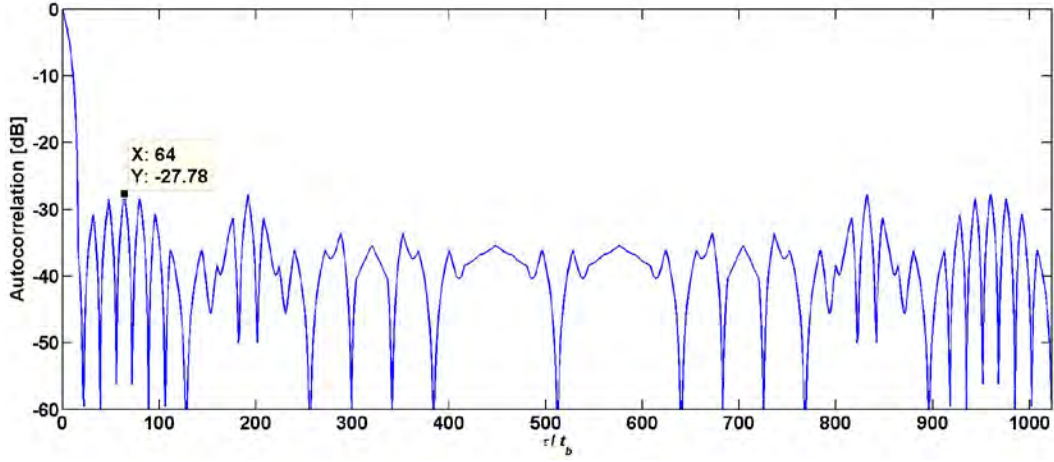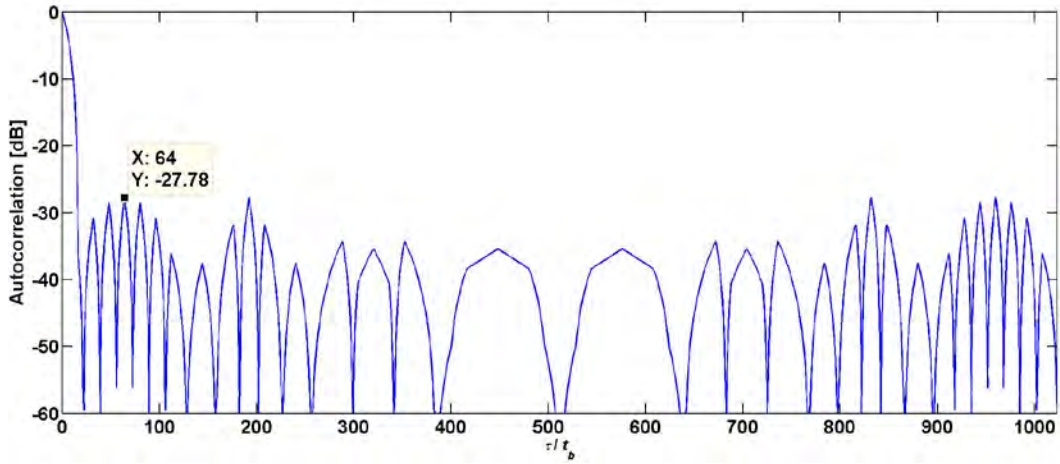
Figure 18.   Multiple Reference P1 Code ACF

ACF of the 64-element P1 modulated signal with $N = 4$. Adapted from [9]: P. E. Pace, *Detecting and Classifying Low Probability of Intercept Radar*, 2nd ed., Norwood, MA: Artech House, 2009.
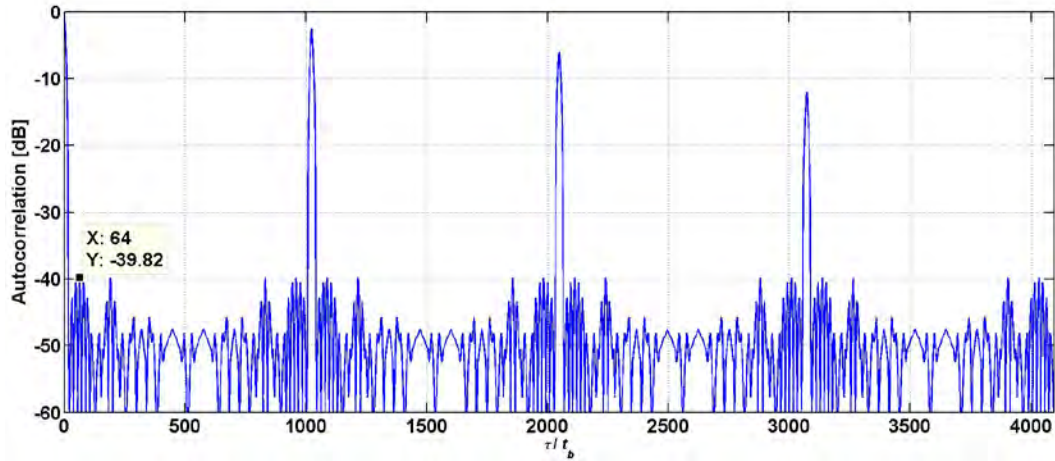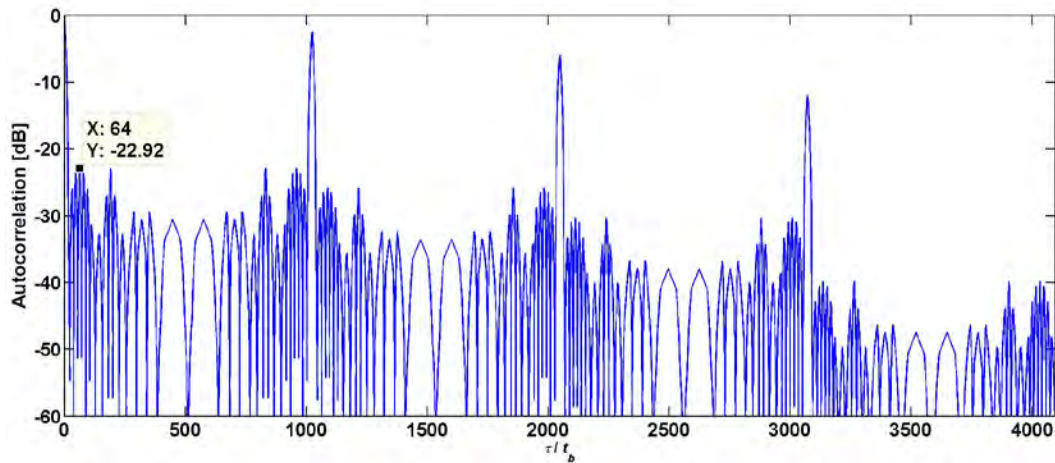

Figure 19.   Multiple Reference P2 Code ACF

ACF of the 64-element P2 modulated signal with $N = 4$. Adapted from [9]: P. E. Pace, *Detecting and Classifying Low Probability of Intercept Radar*, 2nd ed., Norwood, MA: Artech House, 2009.

C.   P3 AND P4 CODES

1.   History

The P3 and P4 codes were derived from a family of codes known as the Zadoff-Chu codes in 1982 by Lewis and Kretschmer [15]. Just as in the case of the P1 and P2 codes' relationship to the Frank code, the P3 and P4 codes are unique phase shifted versions of the Zadoff-Chu code [15]. Unlike the Frank, P1 and P2 codes, the P3 and P4 codes are valid for all integer lengths of subcodes and not just perfect squares [9]. The Doppler tolerance of the P3 and P4 codes is superior to that of the Frank, P1 and P2 codes [15]. While Doppler effects from each of the codes on a SAR image are not studied in this thesis, it is important to note this information so that it can be studied in future.

While the P3 and P4 codes are derived from a common source, they have some major differences. One of those differences is that the P3 code is only perfect for even-numbered code lengths [15]. Also, the P3 codes places its largest single-step phase changes at the center of the code versus at the ends of the code like the P4 [15]. This difference in phasing can be seen in a comparison of Figure 20 and Figure 22. To further grasp these differences in the codes, we look at how their individual phase vectors are calculated in the next section.

2.   Mathematical Discussion

In this section we look at the equations that define the phase states of the P3 and P4 sequences. The equation defining the individual phase states of the P3 and P4 codes are defined, respectively, as [15]

$$\phi(m) = \frac{2\pi}{M}\left[\frac{(m-1)^2}{2}\right], \tag{26}$$

and

$$\phi(m) = \frac{2\pi}{M}(m-1)\left(\frac{m-1-M}{2}\right), \tag{27}$$

where the variable M is used to define the code length such that $N_c = M$ and the variable m is simply the discrete index variable. These two phase history matrix equations do not

need to be modified to convert a matrix to a vector as with the Frank, P1 and P2 code equations. This is due to (26) and (27) depending only upon a single indexing variable m in order to create their phase history data.

3.   P3 and P4 code Simulations

The P3 and P4 codes were implemented using (26) and (27). Since the P3 and P4 codes only depend on a single indexing variable, there is no need for the two-step mathematical conversion process used for the Frank, P1 and P2 codes. There is also no need to use the construction method for the P3 and P4 codes because their phase history is already in vector form.

a.   *Phase versus Phase Index*

In this section, the phase history for the P3 and P4 codes is discussed to demonstrate to the reader how the signal's phase is being modulated. This is done by showing plots of the phase history for each of the sequences over the full code period. Figure 20 and Figure 22 were created by plotting the phase variable $\phi(m)$ over the entire code sequence of the P1 and P2 codes, respectively.

In Figure 20, we see that the P3 code initially has a small phase step or phase slope that steadily increases over the length of the code sequence. It is this continuous phase slope or frequency change that gives the P3 code a better Doppler tolerance over the stepped frequency or stepped phase slope of the Frank, P1 and P2 codes shown earlier [15]. To better understand how the P3 code modulates the carrier sinusoid signal, we plot $\phi(m)$ modulo 2π as shown in Figure 21. We see in Figure 21 that the step-to-step phase change steadily increases as the code index approaches the center, where the largest step-to-step phase change in the sequence occurs. Another interesting observation from Figure 21 is that the P3 code sequence mirrors itself across its center index value.

Figure 20.   P3 Coded 64-Element Phase Shift

Phase shift for each subcode period of the P3 coded 64-element sequences. Adapted from [9]: P. E. Pace, *Detecting and Classifying Low Probability of Intercept Radar*, 2nd ed., Norwood, MA: Artech House, 2009.

Figure 21.   P3 Coded 64-Element Phase Shift Modulo 2π

Phase shift of the signal for each of the subcode periods of the P3 coded 64-element sequence modulo 2π. Adapted from [9]: P. E. Pace, *Detecting and Classifying Low Probability of Intercept Radar*, 2nd ed., Norwood, MA: Artech House, 2009.

31

From Figure 22, we see that the P4 code initially has a large step-to-step phase change, which is minimized in the center of the sequence and steadily returns to the large step size as the sequences ends. Just as in the case of the P3 code, the P4 code has an increased Doppler tolerance over the Frank, P1 and P2 codes for its steady frequency change over the length the of the code sequence [15]. We can see that the P4 code is palindromic across its center index just as the P1 and P2 codes are.

To further our understanding of how the P4 code modulates the carrier's sinusoidal signal, we plot $\phi(m)$ modulo 2π as shown in Figure 23. From Figure 23, we see that the step-to-step phase change for the P4 coded is largest at the beginning and end of the code sequence. It is also observed that the step-to-step phase change steadily decreases as the code index approaches the center. Another interesting observation from Figure 23 is, just as in the case of the P3 code sequence, the P4 code mirrors itself across its center index value.
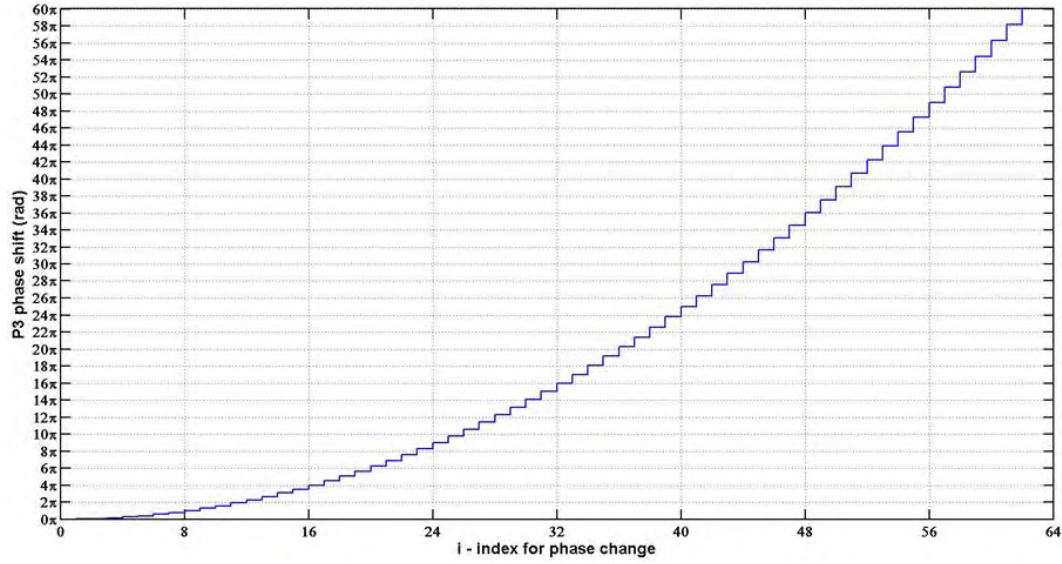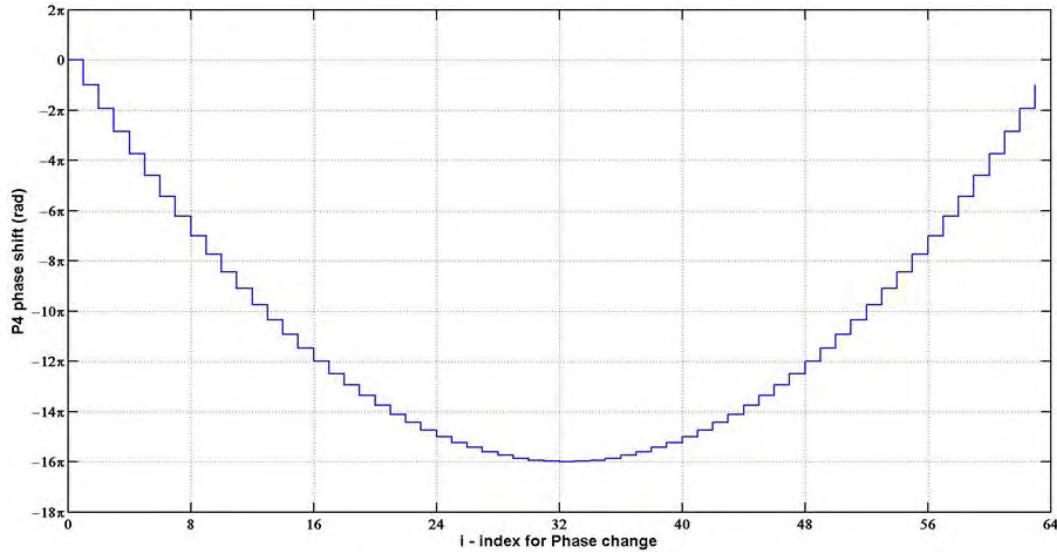

Figure 22.   P4 Coded 64-Element Phase Shift

Phase shift for each subcode period of the P4 coded 64-element sequence. Adapted from [9]: P. E. Pace, *Detecting and Classifying Low Probability of Intercept Radar*, 2nd ed., Norwood, MA: Artech House, 2009.
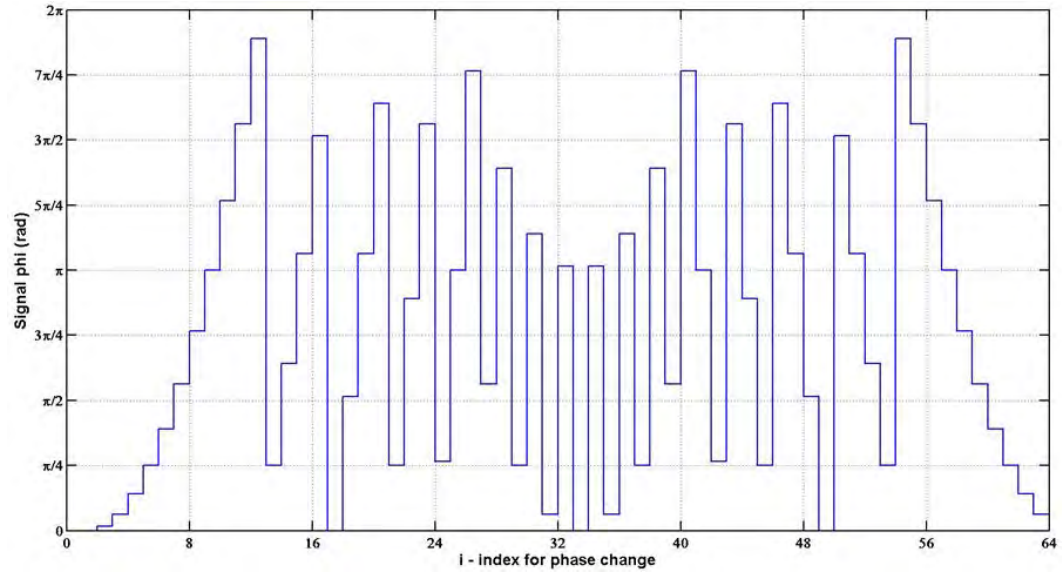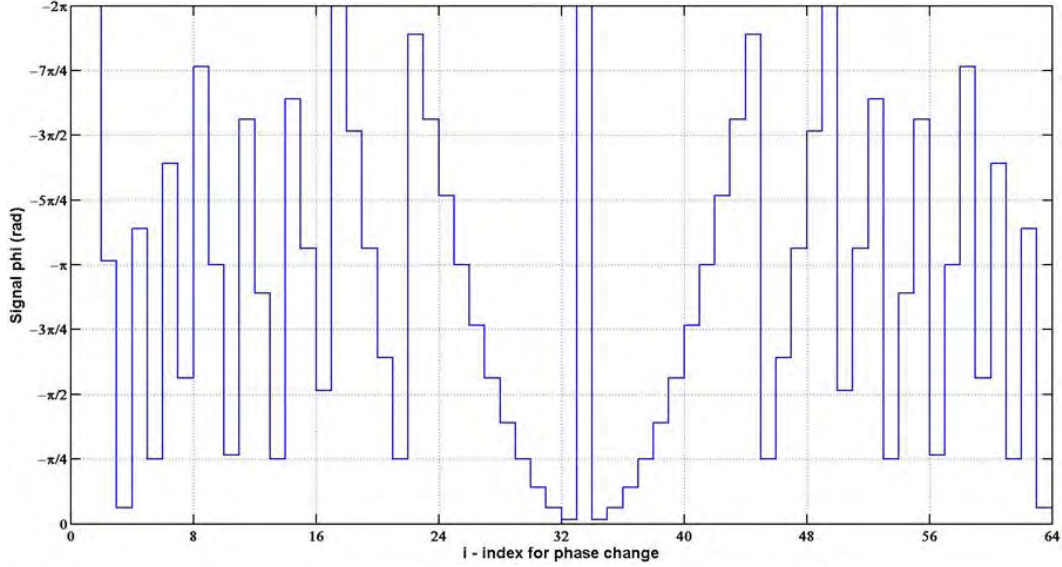
Figure 23.   P4 Coded 64-Element Phase Shift Modulo 2π

Phase shift of the signal for each of the subcode periods of the P4 coded 64-element sequence modulo 2π. Adapted from [9]: P. E. Pace, *Detecting and Classifying Low Probability of Intercept Radar*, 2nd ed., Norwood, MA: Artech House, 2009.

Just as in the previous signal sections, we see in the upcoming time-domain section the "chirp" behavior of these two phase modulations when they are mapped to a carrier signal and plotted over time.

b.   Time-Domain Plots

In this section, the time-domain response of the P3 and P4 codes is discussed, and plots of the modeled waveforms are presented. As for the previously discussed codes, the time-domain plots presented in the following figures were created using (16), (17) and (18) with $\phi(m) = 0$ for the carrier signal and $\phi(m)$ defined by (26) and (27) for the P3 and P4 modulations, respectively.

The time-domain plot for the P3 code is displayed in Figure 24. As for the previous time-domain graphs, the sinusoidal carrier without modulation is shown in the top plot and the carrier with the phase modulation applied is shown in the bottom. Again, the frequency of the sinusoid is 150 MHz. In Figure 24 we see from the second plot why the P3 code is characterized as a "chirp" waveform. It is evident that the time between successive peaks is smaller in the middle of the code sequence than at the ends of the

33

code sequence. This informs us that the code is up-chirping from the start of the sequence to the center and then down-chirping from the center towards the end of the sequence.

The time-domain plot for the P4 code is displayed in Figure 25. Using the same format as for the P3 code, we show the sinusoidal carrier without modulation in the top plot and the carrier with the phase modulation applied in the bottom. Keeping a common frequency for the carrier, we again set the sinusoid to 150 MHz to keep all the waveforms in the thesis comparable. Just as in the case of the P3 code, we are able to see from the second plot of Figure 25 that the P4 code is also chirping; however, in the case of the P4 code, the smallest time between successive peaks is at the ends of the code and the largest time is at the center. With this information, we conclude that the signal is down-chirping from the start to the center of the sequence and up-chirping from the center to the end of the sequences.
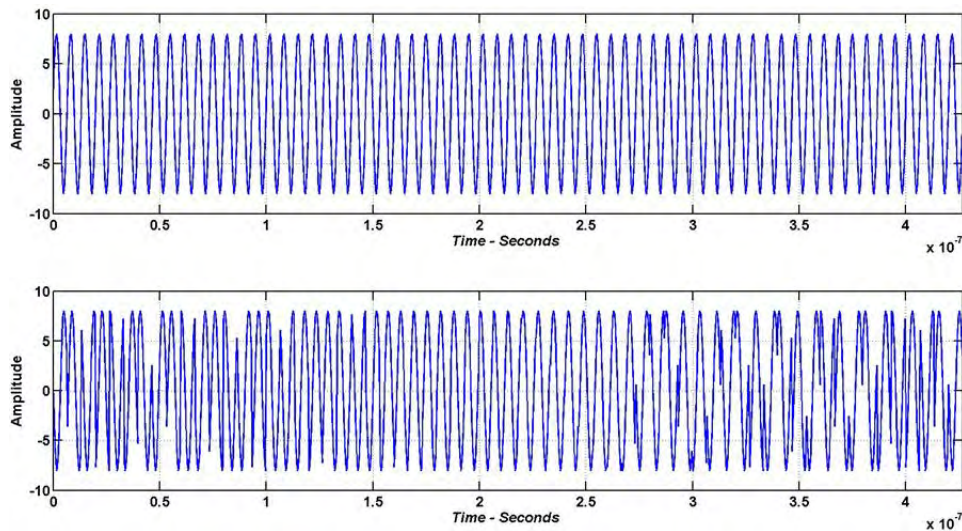
Figure 24.   Sinusoidal Carrier Compared to P3 Coded Modulation

Time-domain representation of the 150-MHz sinusoidal carrier (top) and the P3 coded modulation on the 150-MHz carrier (bottom). Adapted from [9]: P. E. Pace, *Detecting and Classifying Low Probability of Intercept Radar*, 2nd ed., Norwood, MA: Artech House, 2009.

34
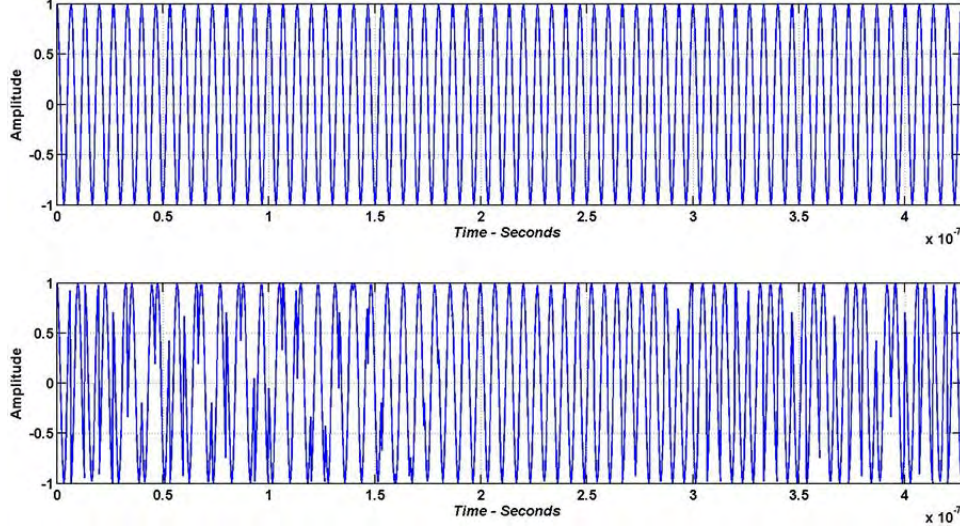
Figure 25.   Sinusoidal Carrier Compared to P4 Coded Modulation

Time-domain representation of the 150-MHz sinusoidal carrier (top) and the P4 coded modulation on the 150-MHz carrier (bottom). Adapted from [9]: P. E. Pace, *Detecting and Classifying Low Probability of Intercept Radar*, 2nd ed., Norwood, MA: Artech House, 2009.

In this section, we saw that the P3 and P4 codes both have LFM waveform characteristics from their individual time-domain plots. We have also seen how the P3 and P4 codes differ in their individual time-domain responses. In the next section, we look at the auto correlation of the P3 and P4 signals.

c.   *Autocorrelation Function*

The ACF for the P3 and P4 codes are discussed in this section. The graphs were created using the same approach as in the Frank code section. The phase state vector $\phi(m)$ from (26) and (27) for the P3 and P4 codes, respectively, were inserted into (16) and (17) and the results were used in (18), yielding the discrete-time signal $s(n)$. The results of (18) were used in (20) to generate the ACF. Just as in previous ACF sections, the x-axis of the ACF plot is defined as the number of samples per subcode multiplied by the number of subcodes of the signal. The y-axis represents the energy of the signal normalized to the energy peak of the mainlobe. As in the case of previous examples, the signal models in this example are captured using 16 samples per subcode and both the P3

and P4 codes each used 64 elements. As a result, we expect the *x*-axis to extend to 1024 samples, as seen in Figure 26 and Figure 27.

For the ACF from Figure 26 and Figure 27, we see the mainlobe and sidelobe response of the matched filter for the 64-element P3 and P4 codes, respectively. This tells us that other signal returns with nearby delays being passed through the matched filter must have enough energy to overcome the sidelobe response of the P3 and P4 codes ACF [15]. In the case of the 64-element P3 code with number of references $N = 1$ as seen in Figure 26, the *PSL* level is approximately −24.4 dB. This is approximately 3 dB worse than that of the Frank and P1 codes, as seen in Figure 10 and Figure 16, respectively, for the same number of subcodes. These modeled outputs of the *PSL* for the P3 and the P4 codes match well with their individual expected theoretical responses. In the next section, we investigate the theoretical *PSL* for the P3 and P4 codes.

Figure 26.   Single Reference P3 Code ACF

ACF of the 64-element P3 modulated signal with $N = 1$. Adapted from [9]: P. E. Pace, *Detecting and Classifying Low Probability of Intercept Radar*, 2nd ed., Norwood, MA: Artech House, 2009.
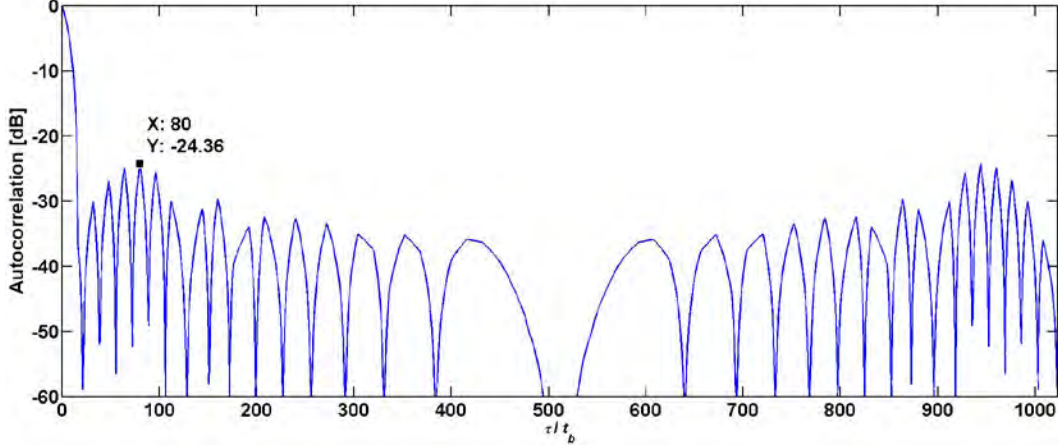
Figure 27.   Single Reference P4 Code ACF

ACF of the 64-element P4 modulated signal with $N = 1$. Adapted from [9]: P. E. Pace, *Detecting and Classifying Low Probability of Intercept Radar*, 2nd ed., Norwood, MA: Artech House, 2009.

d.   *Sidelobe Structure*

As was shown in the previous section, the ACF of the P3 and P4 coded signals have a low *PSL* ratio of approximately −25 dB. While this is not as low as the Frank and P1, it is still quite small. The difference in *PSL* for the P3 and P4 codes from that of the Frank and P1 codes can be explained by their individual *PSL* equations. The *PSL* for the Frank and the P1 code is defined in (21). For the P3 and P4 codes [9]

$$PSL = 20\log_{10}\left(\frac{1}{N} \sqrt{\frac{2}{\left(N_c\pi^2\right)}} \right) . \tag{28}$$

We clearly see that for a given code length and a fixed number of reference waveforms, the Frank and P1 *PSL* is always smaller than the P3 and P4 *PSL* by 3 dB due to the square root of two in the P3 and P4 *PSL* expression. The Frank and P1 codes were modeled as a 64-element code. The 64-element P3 and P4 codes with $N_c = 64$ and $N = 1$ both have a theoretical *PSL* = −25 dB, a difference of 3 dB as compared to the Frank and P1 codes.

We now look at the multiple reference example. Again, we apply (21) to the Frank and P1 code with $L = 8$ but this time with $N = 4$. We find that *PSL* = −40 dB in this case. We can compare this result to the *PSL* for the P3 and P4 codes using $N_c = 64$ and N

37

= 4 in (28). For this case, we see that the P3 and P4 codes both have a theoretical $PSL =$ −37 dB. Again, this is a difference of 3 dB.
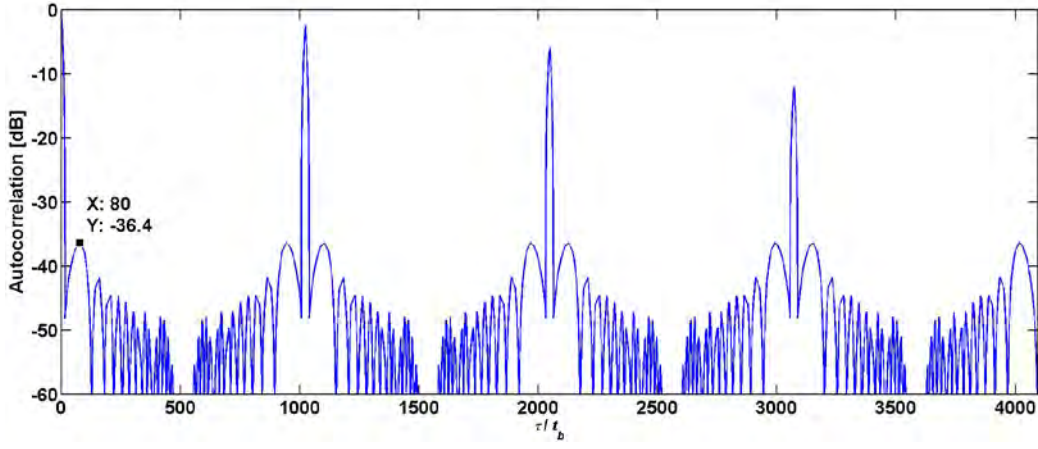
Figure 28.   Multiple Reference P3 Code ACF

ACF of the 64-element P3 modulated signal with $N = 4$. Adapted from [9]: P. E. Pace, *Detecting and Classifying Low Probability of Intercept Radar*, 2nd ed., Norwood, MA: Artech House, 2009.

The ACF of the P3 and P4 codes are modeled with the N_c and N parameter as mentioned above. We can see from Figure 28 and Figure 29 that the modeled *PSL* again agrees well with the theoretical *PSL*. We can note that the *PSL* ratio increased by 12 dB for $N = 4$.
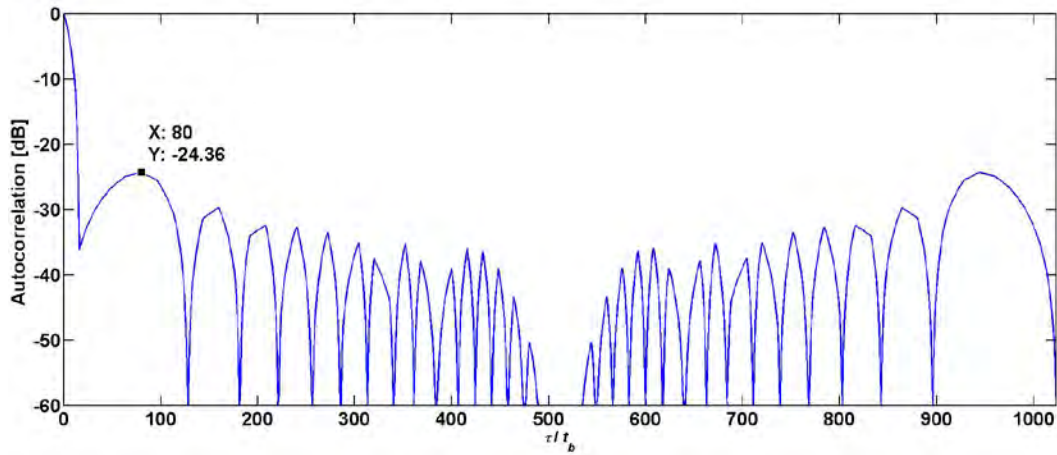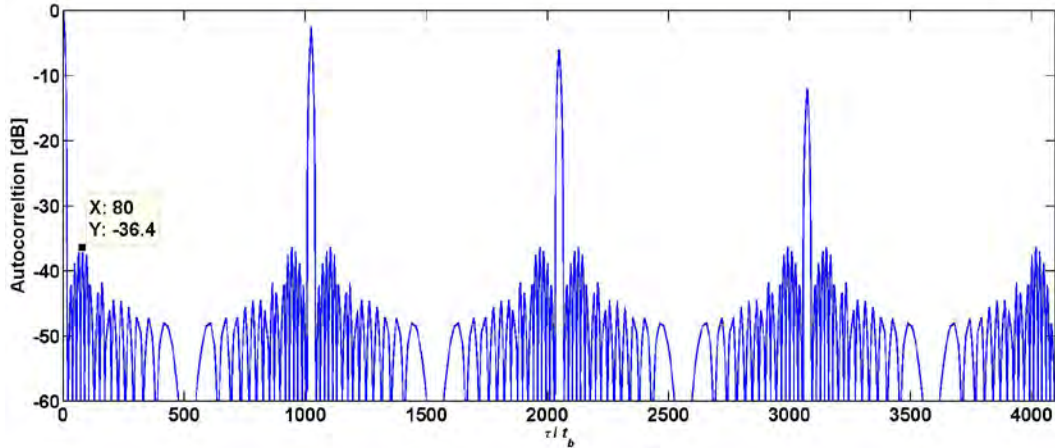

Figure 29.   Multiple Reference P4 Code ACF

ACF of the 64-element P4 modulated signal with $N = 4$. Adapted from [9]: P. E. Pace, *Detecting and Classifying Low Probability of Intercept Radar*, 2nd ed., Norwood, MA: Artech House, 2009.

In this chapter we discussed the five waveforms that are used in the SAR Simulator. The information in this chapter is used in later chapters to explain results. Before we begin the area of study in this thesis, we first build a basic understanding of how radars work and, more importantly, how synthetic aperture radars work. This is the topic of the next chapter.

THIS PAGE INTENTIONALLY LEFT BLANK

IV.   RADAR PRINCIPLES

A RADAR system is mainly comprised of two components, a transmitter and a receiver. The transmitter modulates the signal which serves as the antenna input radiating the signal into free space. The receiver is the system that collects the echoed energy from the transmitted signal and uses the received energy to generate information for display to the radar operator [1]. The operation of a notional radar and its two primary components are depicted in Figure 30.
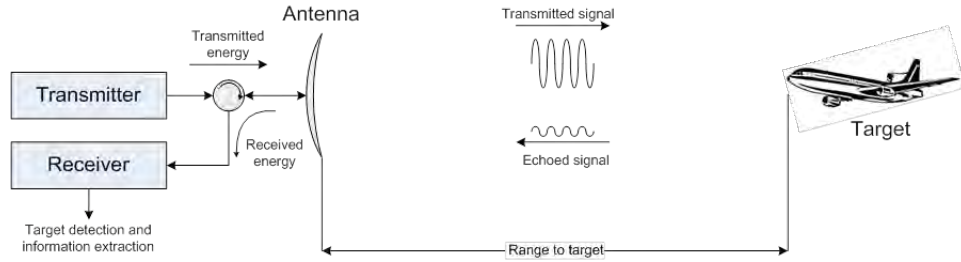
Figure 30.   Top-Level Diagram of Radar Operation

Adapted from [1]: M. Skolnik, *Introduction to Radar Systems*, 3rd ed., New York, NY: McGraw Hill, 2001.

A.   RADAR RANGE, RANGE RESOLUTION AND UNAMBIGUOUS RANGE

RADAR devices are used to detect disturbances in the electromagnetic field that are produced by the RADAR in the targeted space in which it operates [16]. The RADAR measures disturbances in the electromagnetic field and is able to estimate the distance to the disturbance by measuring the change in time Δt it takes for the transmitted signals to travel to the target and return to the RADAR, as depicted in Figure 30. The change in time Δt is given by

$$\Delta t = \frac{2R}{c} \tag{29}$$

where R is the range to the target and c is the propagation velocity of the signal. The factor of two in the numerator of (29) is due to the round trip the transmitted energy makes from the radar to the target and back again. Manipulating (29), we find the range to the target as [16]

$$R = \frac{c\Delta t}{2}.$$ (30)

Using (30) radars are able to calculate the range location of objects in space [16].

Radar range resolution is another important characteristic of a radar, because it defines a radar's ability to resolve tightly spaced objects illuminated by the radar's transmitted energy. If two or more objects are closer together than the radar's resolution capability, the radar is not able to distinguish the individual targets and sees the multiple objects as a single target. A radar's range resolution is described by

$$\Delta R = \frac{c\tau}{2},$$ (31)

where ΔR is a function of the radar signal pulse width τ as defined in [1].

The radar unambiguous range is defined as the range at which the radar is able to make time measurements without radar detection ambiguities occurring. The ambiguities are caused by an echo from a previously transmitted pulse arriving after another pulse has been transmitted, causing a form of aliasing in signal detection to occur in the radar. The unambiguous range is the maximum operating range of the radar for a given pulse repetition period, also known as the pulse-repetition interval (PRI), such that no detection ambiguities are generated and plays a major role in the radar's range capability. A radar's unambiguous range is

$$R_u = \frac{cT_p}{2}$$ (32)

and is a function of the radar's pulse repetition period T_p [1]. The PRI of a signal is the time it takes from the start of one pulse to the start of the next pulse. An example of the signal parameters for a pulse train is illustrated in Figure 31.
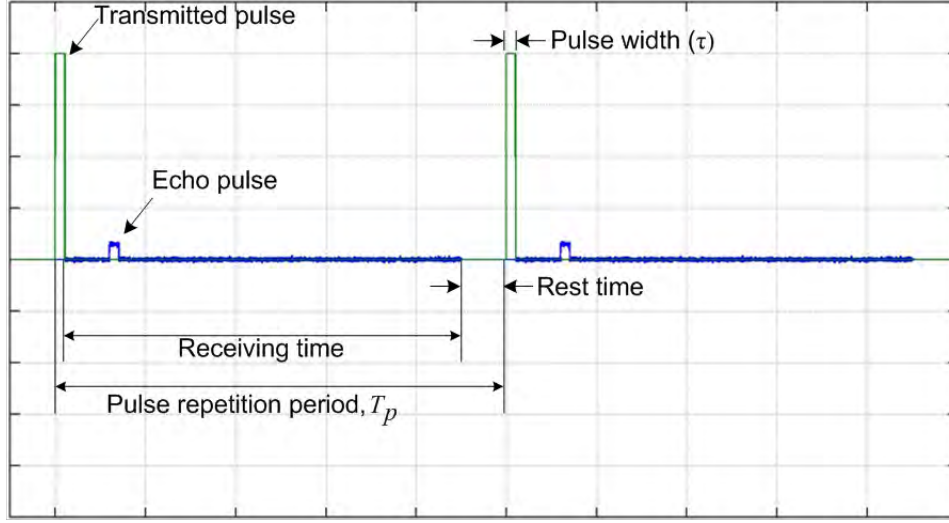
Figure 31.   Simulated Pulse Train Used to Identify Pulse Train Parameters

If we substitute the pulse-repetition period for PSK from (8) into (32), the R_u for PSK signals is

$$R_{u\_PSK} = \frac{cN_c t_b}{2} \; .$$ (33)

Substituting (31) into (33) yields

$$R_{u\_PSK} = N_c \Delta R \; ,$$ (34)

which is the unambiguous range definition for PSK signals [9].

B.   SAR RANGE IMAGING

1.   SAR Range Imaging Description

In this section, the mathematical equations and models for range imaging, also known as echo location, which are used as a basis or starting point for defining range resolution and extent are provided. In this thesis, range-to-target is defined as the distance from the radar to the target as the radar moves along its flight path. Range imaging is used by SAR radars to determine the range location of the objects in the targeted scene [3].

Before we define the mathematical equations for range imaging, we first establish ground rules for the model. First, the radar is assumed to simultaneously transmit and

43

receive with infinite isolation between the transmission and receive channels. This means the radar does not turn off the receiver while it transmits a signal or turn off the transmitter while waiting for the echoed return signal. This assumption is required because we are investigating near-continuous wave signals and are transmitting and receiving at the same time. In practice, shutting off the transmitter while receiving is traditionally done so that the radar does not blind itself with its own transmissions or cause permanent damage to the receiver hardware. We also assume the radar is monostatic and not bistatic, meaning that the radar transmits and receives out of the same antenna or sensor.

Secondly, we assume that the targeted scene does not move, meaning that the radar is not trying to image a moving object such as a fighter jet. Furthermore, in this thesis we only consider imaging ground patches. This mathematical model is limited to ground scenes comprised of m range cells and n cross-range cells. A third assumption is based on the targets, their individual radar-cross sections (RCS) and how they are defined. The reflectivity of a target depends on several parameters such as target size, angle-of-incidence and material make up. In this thesis, each of the target's characteristics are ignored and the target reflectivity is assumed to be that of an ideal point reflector, which is defined as a constant reflectivity for each of the individual targets [10].

The final assumption made in this thesis is relatively common in SAR models and is known as the "stop-and-go" assumption. What is meant by this is the radar stops at each predefined location along the synthetic aperture to transmit and receive signals before moving on to the next location along the synthetic aperture [3].

An illustration recreated from Soumekh showing a collection of n targets illuminated by a radar beam forming a SAR range imaging scene is shown in Figure 32. The idea of a SAR illuminating multiple targets and performing range processing on them is identical to conventional radar as described in the previous sections. This is the case for a SAR scene when only looking at a single cross-range cell or position. We can see from Figure 32 that the individual point targets are defined by their respective ranges, $x_1, x_2, x_3, \ldots, x_n$ and their respective RCS, $\sigma_1, \sigma_2, \sigma_3, \ldots, \sigma_n$. From the information in Figure 32,

we find that the total target area in range is defined as $2X_0$ and is centered at a point X_c [10].
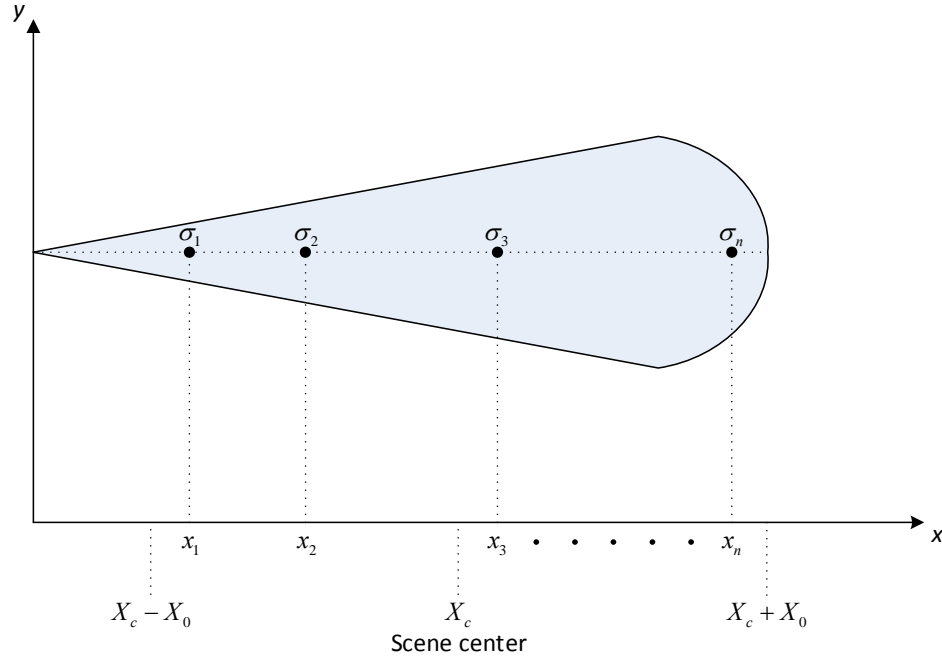
Figure 32.   Depiction of Range-Imaging Geometry

Adapter from [10]: M. Soumekh, *Synthetic Aperture Radar Signal Processing*, Hoboken, NJ: John Wiley & Sons, Inc., 1999.

Using the geometric description defined by Figure 32, we can build a mathematical model that represents the target area previously described. From Figure 32, we know the range-domain target area is a collection of points along the *x*-axis. To mathematically describe these targets along the *x*-axis we use the Dirac delta function $\delta(x_i)$ offset by the location of each target. The magnitude of the individual targets is described by the individual targets RCS, σ_i. Using this information, we can define a function $f(x)$

$$f(x) = \sum_{i=1}^{n} \sigma_i \delta(x - x_i) .$$ (35)

The function in (35) describes each of the discrete targets shown in Figure 32 [10]. The range-domain output of the range-target function described by (35) is illustrated in Figure 33. Now that a mathematical model for the target location and reflectivity has been described, we apply it to the radar's transmitted signal to obtain the return echo that is captured by the radar's receiver. To perform this action, we need to use a mathematical operation known as convolution. A good description of convolution can be found in [12].
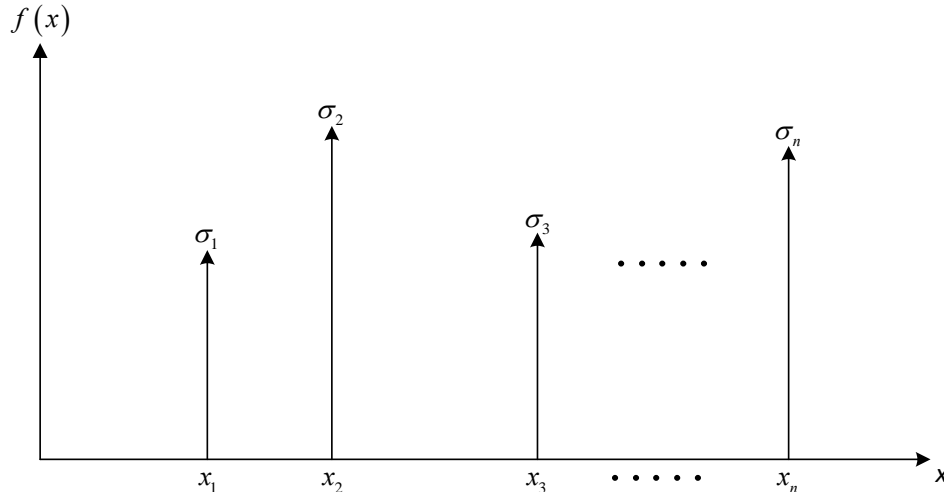
Figure 33.   Output of the Range Domain Target Function

Adapted from [10]: M. Soumekh, *Synthetic Aperture Radar Signal Processing*, Hoboken, NJ: John Wiley & Sons, Inc., 1999.

Assume the radar transmits a time-dependent signal $p(t)$ into a targeted scene described by a target function similar to the one shown in (35). The received signal $s(t)$ at the radar is described by the convolution of the target function and the transmitted radar signal $p(t)$. This is expressed as

$$s(t) = \sum_{i=1}^{n} \sigma_i p\left(t - \frac{2x_i}{c}\right),$$ (36)

where t is the time variable used to describe the time it takes for the signal to propagate to the nth target, re-radiate and propagate back to the radar [10].

2.   SAR Range Extent

For conventional radar, or real aperture radar, the range extent is dependent on the unambiguous range of the radar. This is not the case for synthetic aperture radars. The range extent for SAR is dependent on the range resolution of the radar and the number of range samples the radar takes during the range-integration time, with one complex sample captured for each range resolution cell [17]. Nyquist sampling must be maintained to ensure unambiguous data sampling [17]. The minimum allowable sampling rate is

$$\eta_{s(\min)} = \frac{cT_1}{2\Delta r_s} \; , \tag{37}$$

where Δr_s is the slant-range resolution and T_1 is the range-integration time for the PSK signal. The geometry describing this case is seen in Figure 34. The swath width in Figure 34 is described as the length the antenna 3-dB beamwidth illuminates on the ground in the range direction. The swath width is the maximum physical limit for SAR range extent.

Figure 34.   SAR Range Extent, Data Collection Geometry

Adapted from [17]: D. R. Wehner, *High-Resolution Radar*, 2nd ed., Norwood, MA: Artech House, 1995.

3. SAR Range Resolution

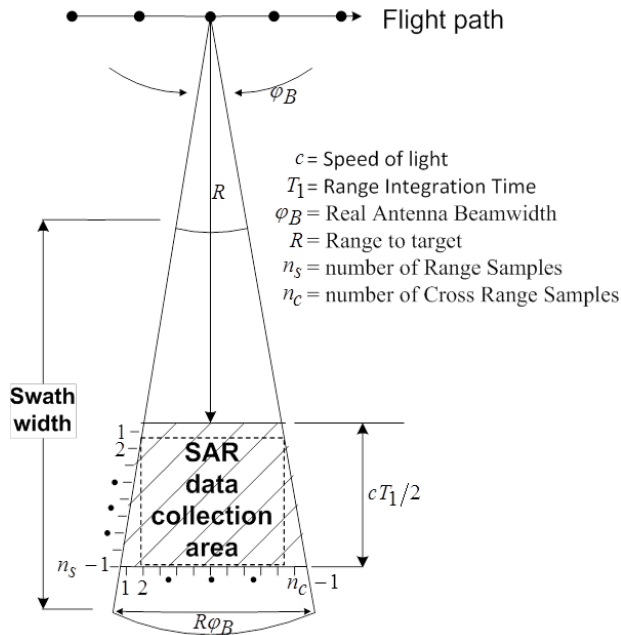Previously, we discussed how the range resolution of conventional radar depends on the pulse width of the transmitted waveform. The pulse duration is, roughly, the inverse of the bandwidth of the signal. For SAR, the range resolution is defined by the bandwidth of the radar signal [3]:

$$\Delta R \approx \frac{cK_r}{2B}. \tag{38}$$

In (38), c is the speed of light, B *is* the bandwidth of the signal and K_r is the excess bandwidth factor due to any signal weighting functions. In SAR, the pulse width is typically not used for range-resolution measurements since the waveforms used are pulse compressed. This compression allows the radar to achieve a finer range resolution, increasing its image quality [3].

C. SAR CROSS-RANGE IMAGING

In this section, the mathematical equations and models for cross-range imaging are presented. The cross-range location is the dimension perpendicular to the range location of an object in a SAR scene. Cross-range cannot be measured from a single radar point; calculating the target's cross-range and locating a target in the scene depends on the motion of the radar and requires multiple range measurements. The cross-range location is what gives SAR radars their imaging capabilities [10] .

1. SAR Cross-Range Imaging Description

To perform cross-range imaging, we assume that all targets lie along the same fixed range position. An example of this is shown in Figure 35, where n targets, $\sigma_1, \sigma_2, \sigma_3, \ldots, \sigma_n$ are located along a fixed-range position X_c. The range position X_c lies within the area illuminated by the radar's antenna beam. Each target's position is defined in Cartesian coordinates as (X_c, y_n), where y_n falls within the cross-range interval $[-Y_0, Y_0]$, as shown in Figure 35.

This span defines a scene cross-range size of $2Y_0$. In Figure 35, the radar moves along the synthetic aperture, or u-axis, from $-L$ to L collecting target information. The

data collection, over a distance, defines the size of the synthetic aperture as $2L$. The radar's instantaneous location along the synthetic aperture is defined as $(0,u)$. The 0 in the radar's location is from the radar lying on the u-axis, shown in Figure 35, giving it a zero range or x-axis value.
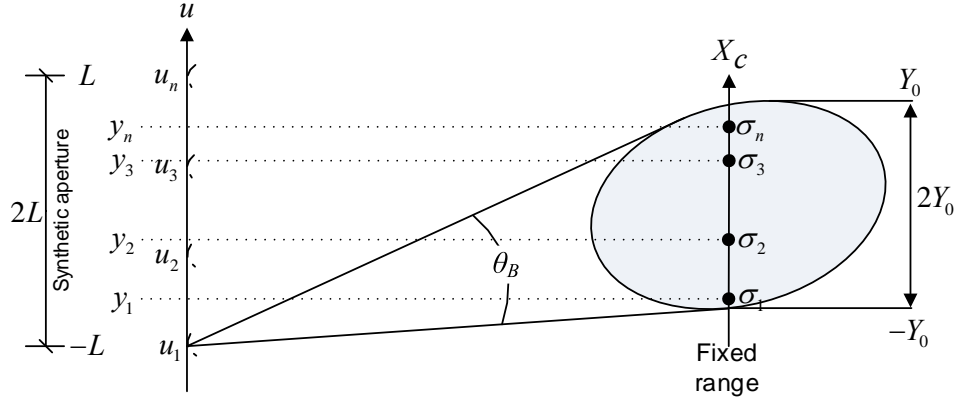
Figure 35.   SAR Cross-Range Geometry

Adapted from [10]: D. R. Wehner, *High-Resolution Radar*, 2nd ed., Norwood, MA: Artech House, 1995.

Generally, the cross-range target function is similar to the range target function in that it is defined by a group of Dirac delta functions $\delta(y_i)$ which are offset by the location of each target:

$$f(y) = \sum_{i=1}^{n} \sigma_i \delta(y - y_i).$$

(39)

The parameter σ_i is the nth target's RCS. At each position u_n along the synthetic aperture, the radar transmits a signal $p(t)$ and records the returned echoes, measuring the distance to each target. From each synthetic aperture point to the next, the range of each specific target changes is due to the motion of the radar; therefore, the distance to the ith target location (x_i, y_i) from the nth synthetic aperture position $(0, u_n)$ is expressed using

$$d_i = \sqrt{x_i^2 + (y_i - u_n)^2}.$$

(40)

Given the previously defined "stop-and-go" assumption, the radar transmits a signal $p(t)$ at each of the discrete synthetic aperture points as the radar moves along the

synthetic aperture. The echoed signals are defined as a summation of the individual target echoes

$$s(t,u) = \sum_{i=1}^{n} \sigma_i p[t - \Delta t].$$ (41)

The value for Δt is found by substituting (40) in place of the variable R in (29), yielding

$$\Delta t = \frac{2\sqrt{x_i^2 + (y_i - u_n)^2}}{c}.$$ (42)

This result gives the round-trip delay for when the radar signal echo returns to the radar from the individual targets.

2.   SAR Cross-Range Resolution

In this section we define cross-range resolution, its variables, and how it differs from the cross-range resolution of real aperture radar (RAR).

As defined in [18], cross-range resolution is the radar's ability to distinguish between two adjacent objects that lie on a plain that is normal to the radar's line-of-sight. For real aperture radar, the cross-range resolution is defined by the width of the radar's antenna 3-dB beam [17]. The antenna beam width φ_B is inversely proportional to the real aperture's physical size and is given by

$$\varphi_B \approx \frac{\lambda}{L_{antenna}},$$ (43)

where λ is the wavelength of the carrier frequency and $L_{antenna}$ is the physical length of the radar aperture in the azimuth or cross-range direction. Real aperture radar's cross-range resolution is defined by

$$\Delta CR_{RAR} \approx \frac{R\lambda}{L_{antenna}},$$ (44)

We see from (44) that the cross-range resolution of a real aperture radar is a function of the radar's distance to the target R, the radar's carrier frequency wavelength λ, and the physical length of the antenna aperture in the cross-range direction $L_{antenna}$. The small angle approximation is used in (44), allowing for the removal of the sine function. We

50

see from (44) that, in order to decrease the cross-range resolution, the physical size of the radar's antenna must increase for a fixed λ and R. This fact presents a fundamental limitation of real aperture radar due to available physical space aboard any given platform.

SAR radars overcome this cross-range limitation by using the motion of the radar to create or synthesize a much larger antenna than what exists physically. This process is accomplished by coherently summing multiple signal returns collected along the synthetic aperture length L_s [18]. The cross-range resolution of a SAR system is similar to that shown by (44). Figure 36 is provided to assist with understanding the variables in the rest of this section and how they relate to SAR geometry. The cross-range resolution still depends on the range of the target and the carrier frequency. The subtle change comes from how the antenna length is defined in SAR. Spotlight SAR cross-range resolution is defined as [3]

$$\Delta CR_{Spotlight\_SAR} = \frac{\lambda K_a}{2\Delta\theta}. \tag{45}$$

The variable K_a is a beam-broadening factor that arises from antenna tapering and is assumed to be one in this thesis [3]. The variable $\Delta\theta$ is defined as

$$\Delta\theta = \frac{L_s \sin(\alpha_{dc})}{R}, \tag{46}$$

in [3]. The sine function in the numerator of (46) is a beam-broadening factor that arises from antenna squint. For this section, we assume that the antenna points broadside, making the sine function equate to one. Using our assumptions, and substituting (46) into (45), we get

$$\Delta CR_{Spotlight\_SAR} = \frac{R\lambda}{2L_s}. \tag{47}$$

The synthetic aperture length L_s in SAR depends on two variables, the velocity of the radar V_p and the time the radar spends observing the targeted scene, as depicted in Figure 36 and further discussed in [5].

51

The similarities between the equations that define cross-range resolution for real aperture radars, expressed in (44), and spotlight mode SAR radars, expressed by (47), were discussed in this section.
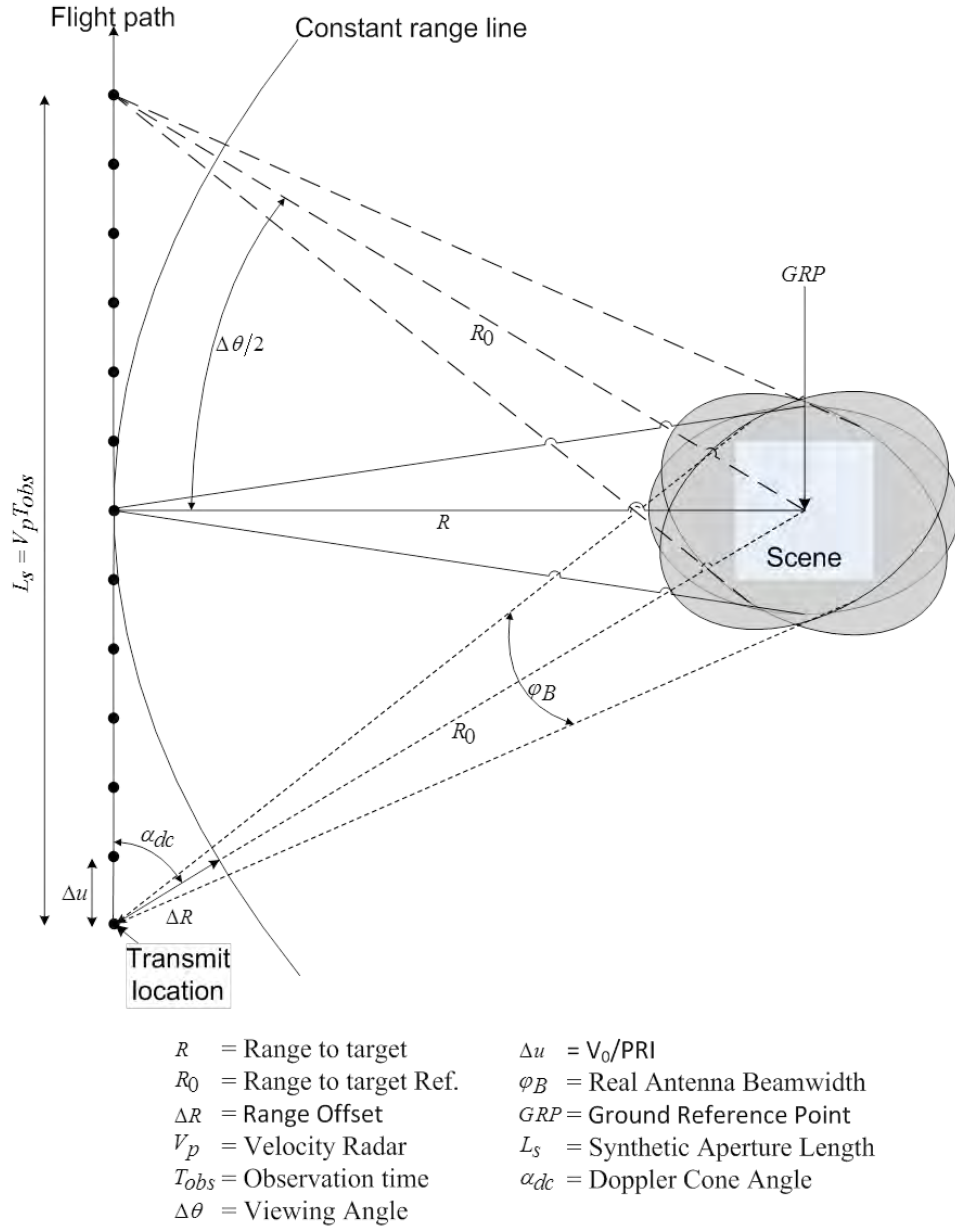

Figure 36.   Spotlight-mode SAR Data Collection Geometry

3.   Two-Dimensional SAR Imaging

In previous sections, we defined range imaging and cross-range imaging and discussed the general mathematical models of each. The next step is to combine the two imaging approaches to form a two-dimensional (2D) image. Since the focus of this paper is on the spotlight SAR mode, we further explore the two-dimensional imaging from a spotlight SAR approach.

In spotlight-mode SAR, the radar's real aperture is continuously pointed at a single ground location or target as the radar traverses the synthetic aperture [6]. As mentioned previously, spotlight mode SAR increases the cross-range resolution of the image by keeping the target in the illuminated area over the full synthetic aperture interval. The spotlight-mode SAR concept of continuous illumination of a single target area, along with the spotlight mode SAR geometry and associated geometric variables, is depicted in Figure 36.

4.   Spotlight SAR Data Collection

How SAR radar collects and stores its data is briefly discussed in this section. A simplified matrix diagram of data collected and stored by the radar for a single-point target is shown in Figure 37. If we consider a SAR radar illuminating its target as it travels overhead, the radar generates an M x N matrix populated with reflected signal returns that are mapped into the matrix using two different time variables. In radar, these time variables are known as fast-time and slow-time. The fast-time data is collected in the columns of the matrix, where each column represents a distinct position along the synthetic aperture. This index is referred to as fast-time because the transmitted radar signal propagates at the speed of light and is much faster than the platform speed, which is related to the slow-time indexing. The fast-time delay of the received echoed signal is proportional to range, as discussed in [10] and [19]. The cells in the columns represent the range bins and define the resolution of the range imaging.

Each row of data corresponds to slow-time samples received from successive reflective radar pulses across the entire synthetic aperture L_s [20]. The slow-time index is generated from the radar's position at the time it transmitted the signal being stored. This

time is called the slow-time index because it changes at a rate proportional to the speed of the radar. Since slow-time corresponds to the motion of the aircraft, it is used to measure cross-range as mentioned in [10] and [19].
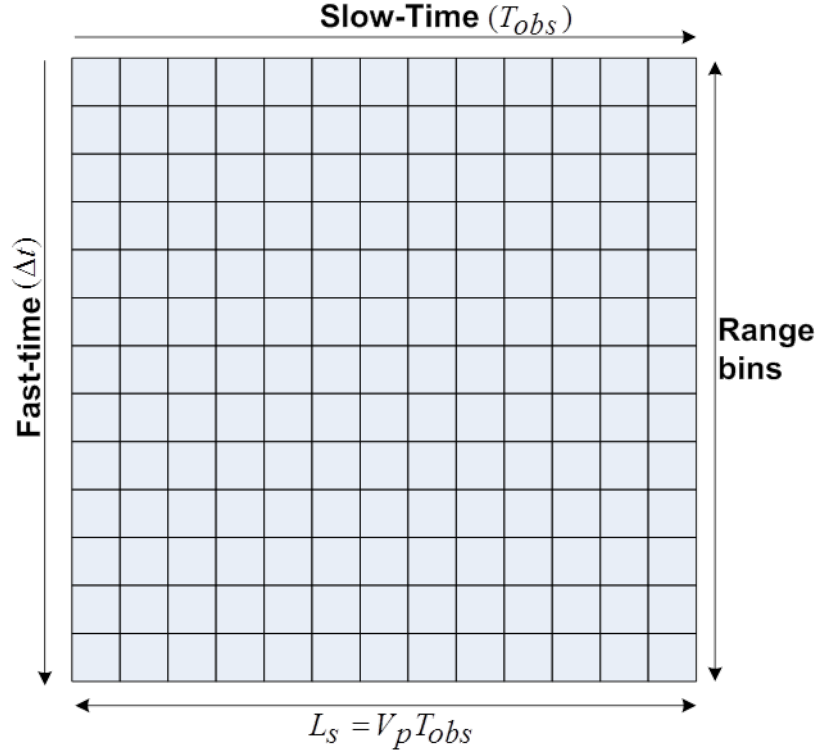
Figure 37.   Notional Synthetic Aperture Data Matrix

In this chapter, we reviewed top-level radar concepts and generated the equations that describe these concepts. We applied those concepts to SAR and redefined the equations for SAR applications. In the next chapter, we use the radar principles discussed in this chapter along with the PSK signals shown in Chapter III to build a PSK SAR model that can be used to study the image sidelobes.

V. LPI SAR SIMULATION

In this chapter, we explain the simulation models used in this thesis. This research combines two simulation models to perform the analysis presented in Chapter VI. The first model builds on the base code by Pace, known as the "LPI ToolBox," that is provided in [9]. The second model is Garren's SAR Simulator model, which is described in [6] and [7]. Both models are modified for use in this thesis, and they are integrated to generate the image information needed to study the individual PSK codes and their resulting sidelobe structure.

A. PSK SAR LPI TOOLBOX

The PSK SAR LPI Toolbox, also referred to as the PSK signal generator, is a modified/reduced version of the original LPI Toolbox. The PSK SAR version created for this research uses modified versions of the Frank, P1, P2, P3 and P4 codes from the original simulation model. The original LPI Toolbox is capable of generating other signal types, but they are omitted from this version. The PSK SAR version only allows the user to change the signal's amplitude, the signal's SNR, the number of subcodes, the number of consecutive code sequences and the signal's bandwidth. In the original version of the LPI Tool Box, the user could change other parameters, but those are now hardcoded in the PSK SAR version. This was done because, currently, the SAR simulator is built for baseband processing, and it is beyond the scope of this thesis to modify the SAR simulator to accept signals outside of baseband. The signal parameters omitted consist of the signal carrier frequency, sampling frequency and cycles per subcode.

The PSK SAR LPI Toolbox's main function is to generate the command line prompt, allowing the user to select one of the five PSK codes studied in this thesis. Invalid entry code has also been added. This particular code checks for non-compliant input and returns the user to the selection window if he or she provides an invalid entry. Once a valid entry is provided, the five modifiable parameters mentioned earlier are displayed and are capable of being set to user-selected values. There is also error checking for valid parameter entries, not only for parameter selection but also for the

individual parameters. For example, the amplitude can never be less than zero. In addition, the number of consecutive code sequences can never be less than one. Furthermore, for the Frank, P1 and P2 codes, the number of subcodes must always be a perfect square, and the bandwidth must always be greater than 1.0 Hz for all code selections. If any of the rules are violated, the input parameters are returned to the original command line values for the selected PSK signal.

Once the user selects all of the parameters and no simulation rules have been violated, the model proceeds to construct the signal per the entered parameters. Once the signal is generated, the user is asked if he or she would like to have the signal graphs displayed. These graphs include time-domain plots and a few phase plots describing the PSK code over the index value of the signal. The PSK signal generator also creates a data file containing the signal information that was generated. The file contains the signal modulation information in quadrature form by storing the I, Q and time vectors of the signal. The naming convention of the file is CodeName$\_f_c\_f_s\_N_c\_cpp\_N\_$SNR dB.

Examples of file names for each of the five different PSK codes are shown in Table 1. The letter "s" in the signal-only name tells the user that the generated signal contains no noise, or infinite SNR. The PSK signal generator produces a file that the SAR simulator uses to generate its transmission signal and the matched filter used on the correlation receiver.

Table 1.   Naming Convention of Output File Generated by the PSK LPI Toolbox

File Description	Example File Name
Signal and noise:	FR_150000_2400000_256_1_1_0
Signal only:	FR_150000_2400000_256_1_1_s
Signal and noise:	P1_150000_2400000_256_1_1_0
Signal only:	P1_150000_2400000_256_1_1_s
Signal and noise:	P2_150000_2400000_256_1_1_0
Signal only:	P2_150000_2400000_256_1_1_s
Signal and noise:	P3_150000_2400000_256_1_1_0
Signal only:	P3_150000_2400000_256_1_1_s
Signal and noise:	P4_150000_2400000_256_1_1_0
Signal only:	P4_150000_2400000_256_1_1_s

B. DESCRIPTION OF SPOTLIGHT SAR SIMULATOR MODEL

In this section, we examine how the SAR simulator model works and how it applies to this thesis. We also look at the changes or modifications made to the simulator for use in this thesis. To do so, it is important to understand the geometry and the coordinate system of the model. This process is followed by a step-by-step description of the model supported by the equations used in its development.

1. Geometry and Coordinates of SAR Simulator

In order to understand the output images of the SAR model, we must first understand the geometry and the coordinate system between the radar and the scene that is to be imaged. This information is discussed in detail in [6] and [7]. The target ground plane is defined as $\{x,y,z\} = \{0,0,0\}$. This point in the coordinate system is named the ground reference point (GRP) and is important to note because it is the range reference point for the rest of the scene. The GRP is also the target of the radar's peak, or the center of its antenna beam pattern, over the imaging time of the radar. In [6] and [7] the z-coordinate is defined as increasing with increasing elevation, the x-coordinate is defined as increasing with range from the radar, and the y-coordinate is defined orthogonally to both the z and x-axis such that it defines the cross-range direction of the radar. The three coordinates described form a Cartesian coordinate system as shown in [6] and [7].

We now relate the coordinate system above to the time dimension since the SAR radar collects its data to form the SAR image of the targeted scene over a time interval. This time interval, shown in Figure 36, is the observation time T_{obs}, and it represents the total time the radar images the targeted scene [6], [7]. We keep the GRP at $\{x,y,z\} = \{0,0,0\}$, as defined above, so we must define the length of the synthetic aperture such that the center is defined between $-V_p\,T_{obs}/2$ and $V_p\,T_{obs}/2$. This selection places the GRP at the center of the synthetic aperture as defined in [6] and [7].

We can now construct a set of useful parameters that define the radar trajectory in the SAR model. The parameterization used in [6] and [7] is as follows:

$$X(t) = -R_{Gr} , \tag{48}$$

$$Y(t) = \pm V_0 t , \tag{49}$$

57

and

$$Z(t) = Z_0 \ . \tag{50}$$

In (48), (49), and (50), $-R_{Gr}$ is the ground range from the GRP to the radar, V_0 is the speed of the radar and Z_0 is the radar's elevation above the defined ground plane or GRP. The "$\pm$" in (49) defines the direction in which the platform is moving. A positive sign denotes that the platform is moving in the $+y$-direction as defined in [6] and [7]. Also defined in [6] and [7] are the two equations for the azimuth and elevation angles of the radar relative to the GRP. They are, respectively,

$$\theta(t) \equiv \arctan\left(\frac{Y(t)}{X(t)}\right) , \tag{51}$$

and

$$\varphi(t) \equiv \arctan\left(\frac{Z(t)}{\sqrt{X^2(t) + Y^2(t)}}\right) . \tag{52}$$

The two angle equations are defined from the geometric coordinates shown in (48), (49) and (50).

2.   SAR Simulator Description

Now that we have defined the geometry and the image coordinate, we discuss the SAR simulator. A flow diagram of the simulator is shown in Figure 38. Each of the blocks is described in the following section to further our understanding of the simulator.
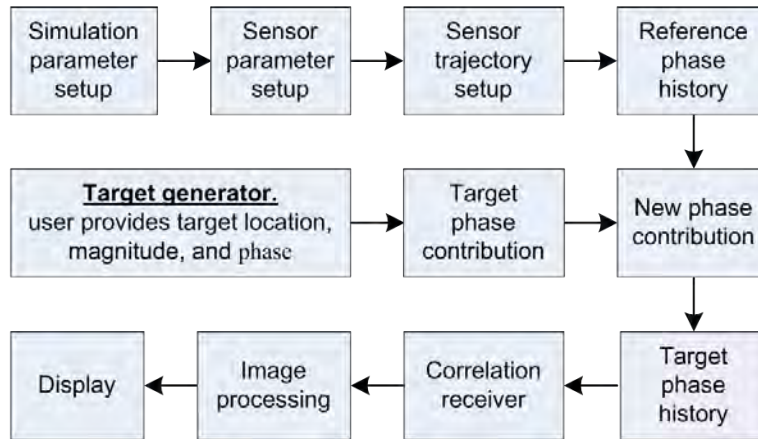

Figure 38.   Flow Diagram of SAR Simulator

58

Simulation and Sensor Parameter Setup

Before the simulation begins, many parameters for the simulator, including the modeled sensor and the targeted scene, must be loaded into the simulator. This happens in the "simulation parameter setup" block, shown in Figure 38. Some of the functions that were developed in [6] and [7] were modified for this thesis. These functions act as a form of header from which the SAR Simulator loads the required information to perform its task. Some of the parameters in these files are physical constants, such as π and the speed of light. Other parameters are related to the generation of the SAR images, such as the dynamic range of the SAR image. In this thesis, this variable is set so that the sidelobes of the waveforms are illuminated in the image and can be studied.

The radar, or sensor, is defined in the "sensor parameter setup" block, shown in Figure 38. This function allows the user to define the following characteristics of the radar: center frequency, the signal bandwidth, cross-range extent of the image, the range extent of the image, the speed of the radar, the direction the antenna beam is pointing, the ground range to the targeted scene and the elevation of the radar. Other parameters, such as the elevation angle γ and the required T_{obs} are defined by the parameters inputted by the user:

$$\gamma = \operatorname{atan}\left(\frac{Z_0}{R_{Gr}}\right),$$ (53)

and

$$T_{obs} = \frac{R\lambda}{2V_p\delta_{cr}}.$$ (54)

For (54), the variables R and V_p are defined in Figure 39. The variable R is the slant range to the target. The variable $\delta_{cr} = \Delta CR_{Spotlight\_SAR}$ refers to the cross-range resolution. In the simulator, the cross-range resolution is set to match the range resolution so the image is created from square pixels. The variable λ is the wavelength of the carrier frequency. A derivation of (54) is given in [21]. Once the radar parameters are set, we can establish the target parameters used in the SAR simulation.

RADAR

Z_0 = Height of radar
R = Slant Range
R_{Gr} = Ground Range
R_{uGr} = Unambiguous Ground Range
R_u = Unambiguous Slant Range
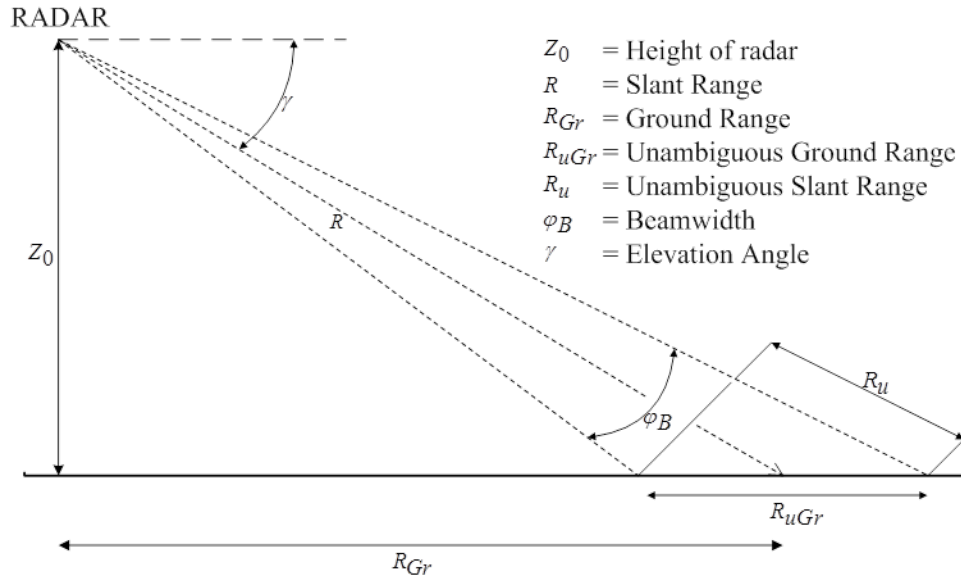φ_B = Beamwidth
γ = Elevation Angle

Figure 39.   Depiction of Radar Geometric Parameters

The targets in the SAR Simulator are defined by the user; point targets are placed in the $\{x,y,z\}$ coordinate plane. The user defines the target in the "target generator" block, shown in Figure 38. This function allows the user to define the characteristics of scattering centers. These characteristics include the $\{x,y,z\}$ coordinates of the target, the $\{x,y,z\}$ velocity of the target and the individual's RCS response in the form of phase and magnitude as seen in Table 2.

Table 2.   Target Parameter Definition for 11 Different Targets Used
in the SAR Simulator

Target	1	2	3	4	5	6	7	8	9	10	11
x pos.	0.14	0.14	13.4	13.4	28.4	28.4	35.4	−11.2	−11.0	−22.0	-23.0
y pos.	−6.1	20.0	−14.1	22.6	12.1	25.3	15.5	0.1	25.0	13.1	25.5
z pos.	0.0	0.0	0.0	0.0	0.0	0.0	0.0	0.0	0.0	0.0	0.0
x vel.	0.0	0.0	0.0	0.0	0.0	0.0	0.0	0.0	0.0	0.0	0.0
y vel.	0.0	0.0	0.0	0.0	0.0	0.0	0.0	0.0	0.0	0.0	0.0
z vel.	0.0	0.0	0.0	0.0	0.0	0.0	0.0	0.0	0.0	0.0	0.0
Mag.	10.2	10.1	9.9	10.2	10.1	9.9	10.2	10.1	9.9	10.2	10.2
Phase	13.2	34.3	−127.2	56.2	34.3	−127.2	56.2	34.3	−127.2	56.2	34.3

At this point, the simulator has the parameters it needs to begin the calculation process. The next step in the functional flow diagram, shown in Figure 38, is for the simulator to establish the sensor's trajectory. This is done by describing an idealized impulse of the projection range, as described in [6] and [7], and given by

$$\tilde{g}_{\theta,\varphi}(\rho) = \int dx \int dy \int dz \, f(x,y,z) \, \delta\big(x\cos(\theta)\cos(\varphi) + y\cos(\theta)\sin(\varphi) + z\sin(\theta) - s\big). \tag{55}$$

Garren asserts that (55) is essentially a form of the Radon transform [6].

b.   Simulator Phase History Generation

The radar's trajectory is calculated over the observation time defined by (54). This time is divided into the number of observation points that the user has defined. The radar's position at each of these times is stored. In Cartesian coordinates, this information is the idealized projection range from the radar to the GRP of the targeted scene. The calculated information is then converted from a Cartesian coordinate system into a spherical coordinate system and stored. These calculations establish a reference range R_0 and a reference phase for a fixed carrier frequency at each of the observation points along the synthetic aperture for the assigned elevation and azimuth angles. The equation that defines R_0 is derived in [6] and [7] as

$$R_0\big(\theta(t_n),\varphi(t_n)\big) = \sqrt{\{X(t_n)\}^2 + \{Y(t_n)\}^2 + \{Z(t_n)\}^2}, \tag{56}$$

where t_n is the slow-time variable. The calculations that produce the reference phase history data are then repeated for each of the individual scattering centers inside of the targeted scene. This produces a phase history data vector R_i defined in [6] and [7] and given by:

$$R_i\big(\theta(t_n),\varphi(t_n)\big) = \sqrt{\{X(t_n) - \alpha(t_n)\}^2 + \{Y(t_n) - \beta(t_n)\}^2 + \{Z(t_n)\}^2}. \tag{57}$$

This phase information is calculated for each of the range bins at each of the observation points along the synthetic aperture. In the next section, we discuss how the simulator uses this ideal phase information and turns it into radar echoes.

c. *Radar Echo Formation and Generation*

Using the reference phase history data from (56) and the scattering phase history data from (57), we generate an idealized radar echo. To start this process, the simulator takes the difference of the two phase history data matrices such that R_0 is subtracted from R_i to obtain [6], [7]

$$\Delta R_i(t_n) = R_i(\theta(t_n), \varphi(t_n)) - R_0(\theta(t_n), \varphi(t_n)). \tag{58}$$

The radar echoes are then defined by the variable [6], [7]

$$G(f_m, t_n) = \sum_i \sigma_i \exp(-2\pi \, \Delta R_i(t_n) \, 2 f_m/c), \tag{59}$$

where σ_i defines the magnitude of the scattering centers RCS, ΔR_i is the phase contribution of the scattering center due to its location in the scene as a function of slow time, t_n, and the $2f_m/c$ defines the spatial frequency spherical polar radius as defined in [6] and [7]. In the next section, we explain how the SAR Simulator maps waveforms onto the ideal radar echoes using the $G(f_m, t_n)$ matrix and the output file of the PSK SAR LPI Toolbox.

3. Simulation of Transmit Signals and Received Echoes

The simulation begins by setting up the geometry of the radar with the targeted scene. An ideal or impulse response of the scene is generated. The number of observation points and range bins are established pre-simulation by the user in "sensor parameter setup." This ideal response of the scene is defined in the previous section as $G(f_m, t_n)$ in (59). Using the scattering center distribution of the targeted scene defined in Table 2, along with the radar parameters, presented in Table 3, we generate an ideal radar echo by applying an FFT to the output of (59). This concept is further discussed in [6] and [7] , and is illustrated in Figure 40.

Table 3. Notional Radar Parameters

Simulation Parameters	Assumed Value
Number of Range Bins	250
Number of Observation Points	250
Carrier Frequency	9.0 GHz
Radar Bandwidth	150 MHz
Radar Velocity	200 m/s
Radar Altitude	1 km
Ground Range to Target Scene	30 km

At this point, the SAR simulator uses the PSK SAR LPI Toolbox to generate the modulated signal. Once the PSK signal generator has created the desired signal, the waveform is convolved with the impulse response of the scene, shown in Figure 40, to generate the echo response that uses the desired PSK waveform

$$g_{\theta,\varphi}(s) = p(s) \otimes \tilde{g}_{\theta,\varphi}(s),$$ (60)

where $\otimes$ denotes the convolution of two signals.

The PSK echo is calculated mathematically using (60), where $p(s)$ is the mean time of the waveform in the spatial domain and $\tilde{g}_{\theta,\varphi}(s)$ is the idealized impulse response of the scene. The result of the convolution is plotted in Figure 41. The idealized echo shown in Figure 40 differs substantially from the radar echo due to the Frank coded waveform, shown in Figure 41. For the radar to pull the range information out of the Frank coded echo, shown in Figure 41, a correlation receiver is used. This is the topic of the next section in this chapter.
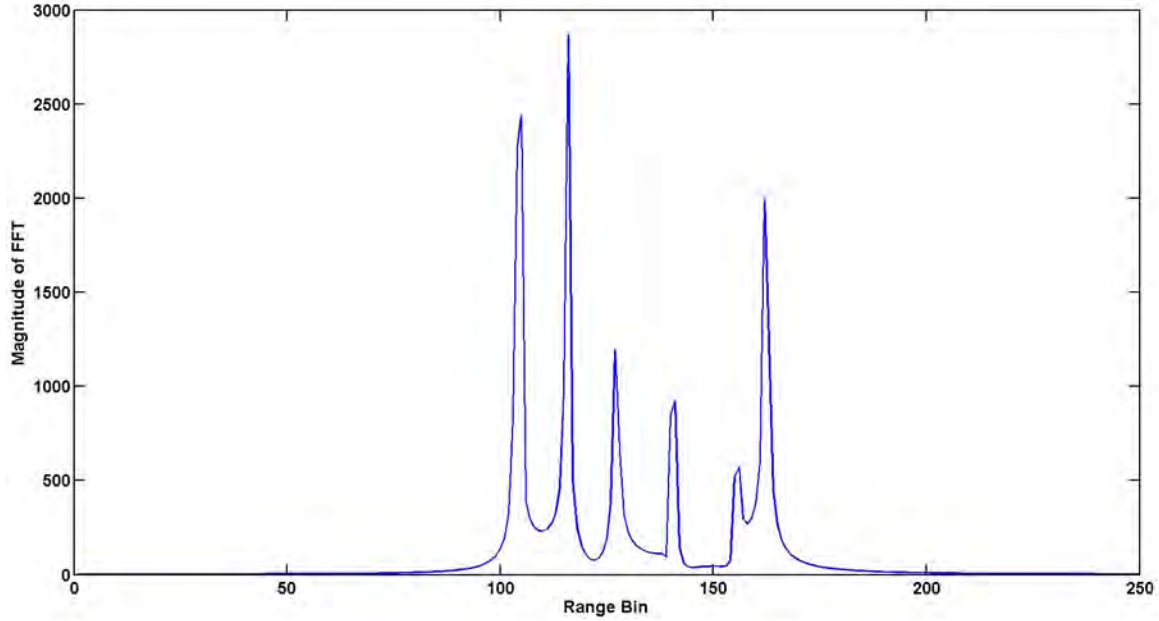
Figure 40.   Idealized Radar Echo

Radar echo that enters the receiver from the radar's initial observation point. Adapted from [6]: D. Garren, P. Pace and R. Romero, "Phenomenology of Low Probability of Intercept Synthetic Aperture Radar via Frank Codes," in *Proc. of SPIE, Algorithms for Synthetic Aperture Radar Imagery XXI*, Baltimore, 2014.
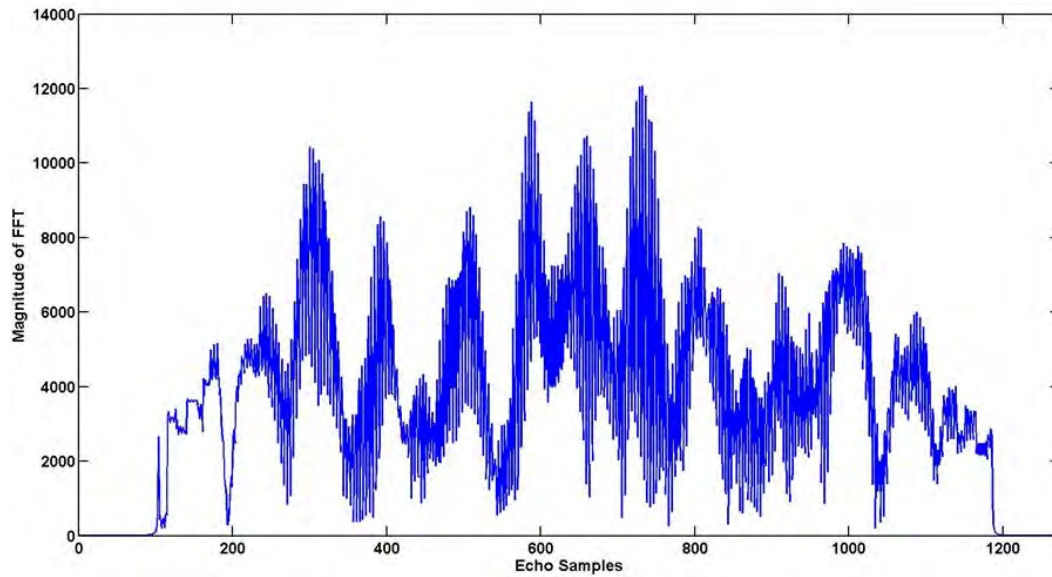

Figure 41.   Radar Echo from a Simulated 256-Element Frank Coded Waveform

Adapted from [6]: D. Garren, P. Pace and R. Romero, "Phenomenology of Low Probability of Intercept Synthetic Aperture Radar via Frank Codes," in *Proc. of SPIE, Algorithms for Synthetic Aperture Radar Imagery XXI*, Baltimore, 2014.

64

4. Correlation Receiver

A block diagram of the correlation receiver is shown in Figure 42. In its simplest form, a correlation receiver compares the received signal to a stored copy of the transmitted signal. The benefit of this type of receiver is that signal distorters, such as noise, do not correlate to the stored signal, so weak signal strengths come out of the receiver and into the image processing units [15]. To create the matched filter, the receiver stores a local copy of the transmitted signal and then correlates the returned echo with the stored waveform. This process allows the radar to generate processing gain in the receiver. The receiver also uses waveform integration to improve SNR.
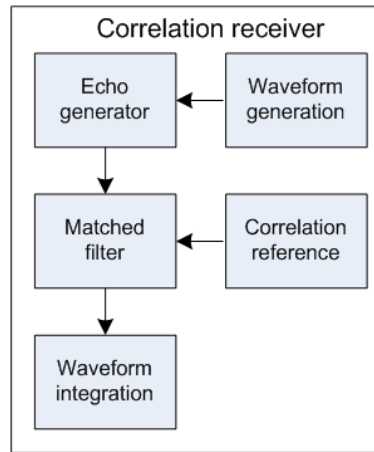

Figure 42.   Signal Flow Diagram Correlation Receiver

Correlation receiver integrated into the SAR Simulator.

a. *Matched Filter*

The SAR Simulator generates a radar echo by convolving the PSK signal with the idealized impulse response of the targeted scene. The correlation reference is also created by the PSK signal generator. As shown in Table 1, the PSK SAR LPI Toolbox creates a signal having a desired SNR defined by the user and a signal with infinite SNR. The signal with the desired SNR is used to create the radar echo. The signal having infinite SNR is used as the correlation reference in the receiver. In Chapter II, the impulse response of the matched filter is the conjugated time reversal of the signal-of-interest, as

seen in (7). To get the output of the matched filter, we must convolve the impulse response of the matched filter with the radar echo $g_{\theta,\varphi}(s)$ [6], [7]:

$$h_{\theta,\varphi}(s) = p^{*}_{\theta,\varphi}(s) \otimes g_{\theta,\varphi}(s). \qquad (61)$$

If the receiver input is the echo shown in Figure 41 and the time-reversed signal that created that echo is used, then the resulting output $h_{\theta,\varphi}(s)$ of the matched filter is represented by Figure 43.
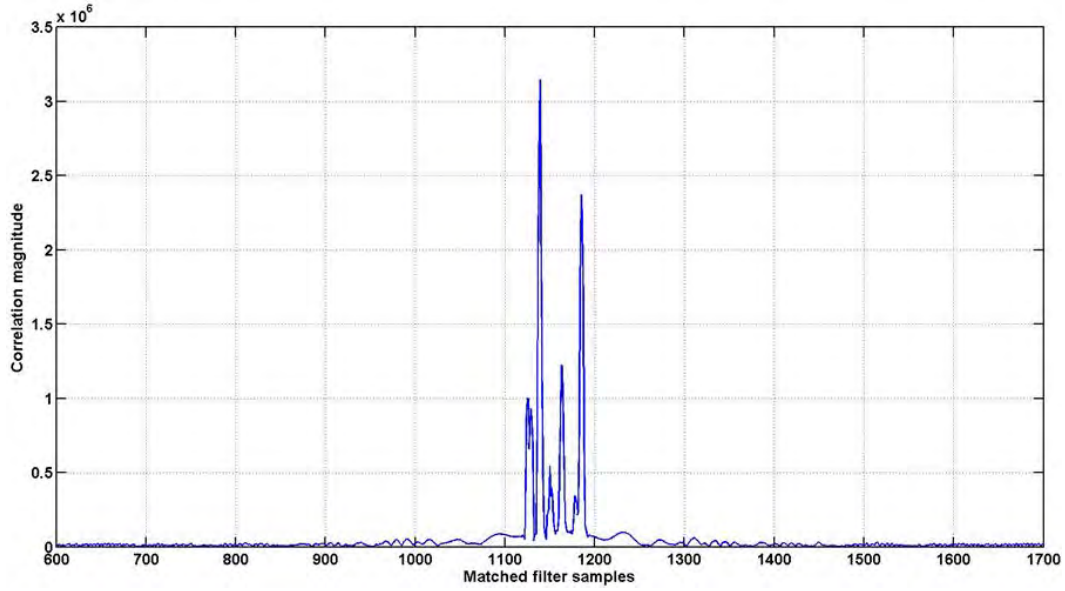

Figure 43.   Matched Filter Output

b.   *Waveform Integration*

Waveform integration in a receiver increases the SNR of the received signal by integrating the total energy over a given interval of time. In the simulation, waveform integration is performed by the integration filter. The integration filter has two roles in the simulation's signal processing. First, it integrates cascaded code sequences to improve the SNR of the receiver. Second, it performs data cleanup by removing any unwanted range samples fed to it by the matched filter. If the input to the integration filter is the output of the matched filter, shown in Figure 43, the output of the integration filter after pulse integration is illustrated by Figure 44.
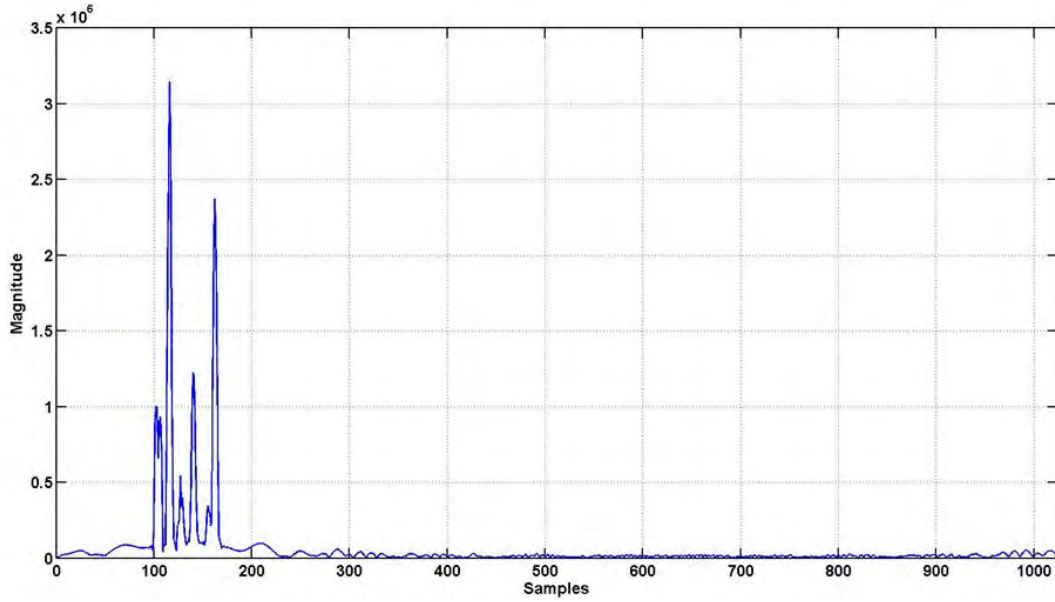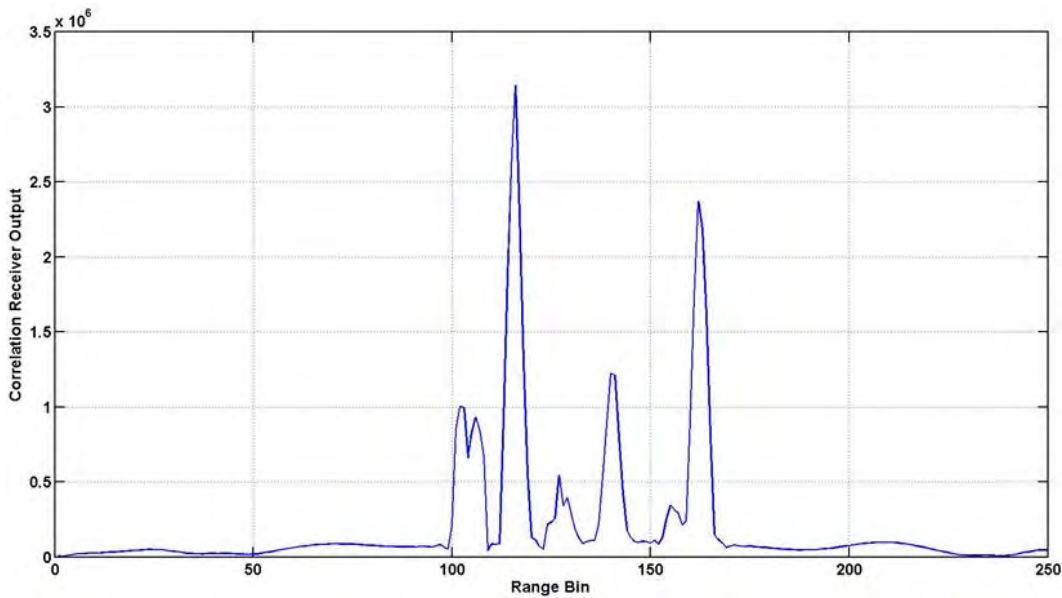
Figure 44.   Integration Filter Output

Figure 45.   Receiver Output

In Table 3, the radar is defined as having 250 range bins. We see that the number of range samples in Figure 44 is larger than the 250 range bins that the radar uses to define its targeted scene. This is where the integration filter performs its second role of truncating the range samples to equal the number of range bins. The result of the truncation can be seen in Figure 45, which shows the output of the correlation receiver.

67

To generate a SAR image from the output of the correlation receiver, the SAR simulator converts the polar formatted data to Cartesian format [6] and [7]. The data tips, shown in Figure 46, are for targets 10, 9, 3 and 6 in Table 2. While the locations in the image are not identical to those shown in Table 2, they are approximately within half of the range and cross-range resolution of the target truth of Table 2. This provides confidence that the SAR Simulator is functioning properly.
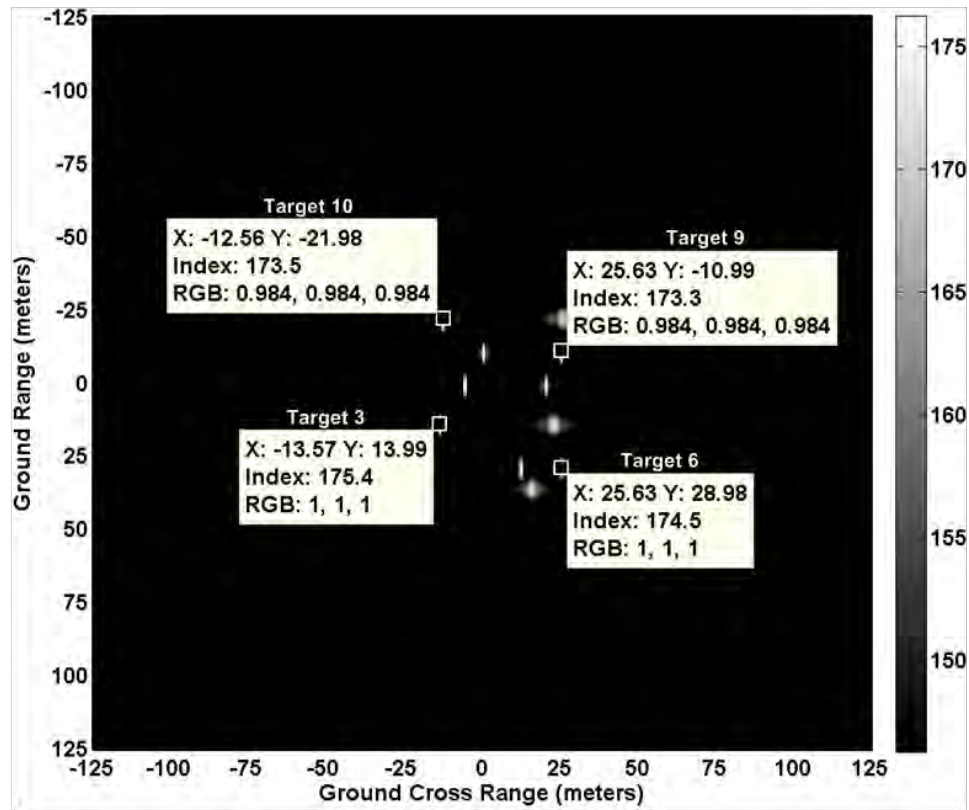

Figure 46.   Simulated SAR Image

SAR image formed using a 256-element Frank code and correlation receiver. (Scale on right is for 30-dB image dynamic range.) Adapted from [6]: D. Garren, P. Pace and R. Romero, "Phenomenology of Low Probability of Intercept Synthetic Aperture Radar via Frank Codes," in *Proc. of SPIE, Algorithms for Synthetic Aperture Radar Imagery XXI*, Baltimore, 2014.

We have shown that the SAR Simulator and the PSK generator are operational and provide acceptable outputs. The next step is to use the outputs to study the image sidelobes of the selected PSK codes. In the next chapter, we use the SAR images and

their corresponding .mat files created by the SAR Simulator and PSK SAR LPI Toolbox to generate images slices that show the range and cross-range sidelobe structure. We then compare the image slices to the five PSK codes that are shown in Chapter III.

THIS PAGE INTENTIONALLY LEFT BLANK

VI.   PSK SIDELOBE STUDY

A.   METHODOLOGY

To study the sidelobe structure created from the five PSK codes generated by the PSK signal generator, a two-step approach is taken. The first step is to define notional radar parameters used in the SAR simulator and declare any assumptions. The second step is to check that the sidelobes of each of the five PSK signals are not distorted in the processing of the SAR image. This is done by increasing the image dynamic range and using a single scattering center. Next, we look at a range "slice" of the SAR image in the location of the scatterer and check that the sidelobe structure of each of the codes look similar, if not identical, to the autocorrelation plots for each of the codes presented in Chapter III.

B.   NOTIONAL RADAR AND SIMULATION ASSUMPTIONS

The first step in the study is to define the radar parameters to be used in the SAR simulator. To begin, we define a targeted scene. For computational purposes, we use a ¼ km by ¼ km scene to investigate the sidelobe levels of the single point target. This selection is shown in Table 4 as the "target area." Also seen in Table 4 is the desired range and cross-range resolution of the SAR image. The resolutions are variable and can be changed in the SAR simulator. The number of range bins and observation points is 250 based on the target area and the range and cross-range resolution. We choose a notional carrier frequency of 9 GHz. The required bandwidth of the signal is defined when the required range resolution is substituted into (38). As seen in Table 4, we set the dynamic range of the image arbitrarily high to ensure that the sidelobe levels of the PSK signals are captured for the second step in the methodology. We select the number of subcodes in the PSK signal such that (34) matches the size of the target area. Because the Frank, P1 and P2 codes have perfect square subcode limitations, the closest N_c value that can be selected, given the 1-m range resolution and perfect square limitation, is 256. This is shown in Table 4. An $N_c = 256$ equates to $L = 16$ for the Frank, P1 and P2 codes. The

radar velocity, altitude and range-to-target scene variables are reused from Table 3 in Chapter V.

Table 4.   LPI SAR Parameters

Simulation Parameters	Assumed Value
Target Area	¼ km by ¼ km
Range Resolution	1 m
Cross-Range Resolution	1 m
Number of Range Bins	250
Number of Observation Points	250
Carrier Frequency	9.0 GHz
Radar Bandwidth	150 MHz
Dynamic Range of Image	100 dB
Number of Subcodes (Nc)	256
Radar Velocity	200 m/s
Radar Altitude	1 km
Ground Range to Target Scene	30 km
Single Target location (Relative to GRP)	20.1m x 19.9m

The second step in the study is to create a SAR image. This step uses the parameters defined in Table 4 for a single-point target that uses the SAR simulator and the PSK signal generator. This approach allows us to observe the sidelobes of the detected signal with the matched filter. Before the sidelobes are studied, we first confirm that the SAR Simulator is placing the target in the correct location as defined in Table 4. A ground truth plot is shown in Figure 47, and the accompanying SAR image for the same target is shown in Figure 48. By comparing the two images, we see that the target from the SAR Simulator is within the accuracy of the SAR resolution.

Now that we have shown that the target is in the correct location, we study the sidelobe energy of the returned signal. From Figure 48, we see that there are sidelobes present in the SAR image in the *y*-axis and *x*-axis directions. To observe these sidelobes, the image scale or dynamic range of the image is set to 100 dB. To isolate the range sidelobes from the cross-range sidelobes, data slices from the image are extracted and plotted over their respective axes. Examples of these slices are seen in Figure 49 and Figure 50. This process is performed for each of the five PSK codes, with a summary of the results in the next section.
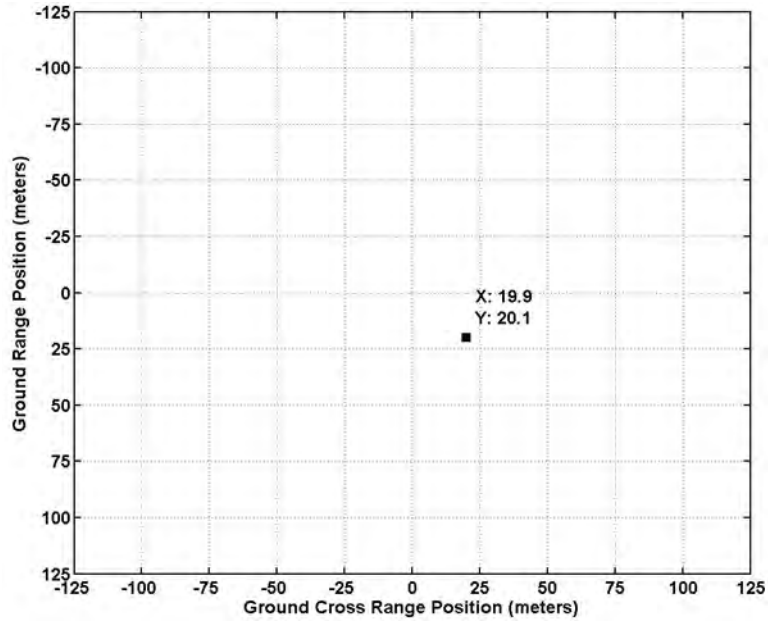
Figure 47.   Target Truth

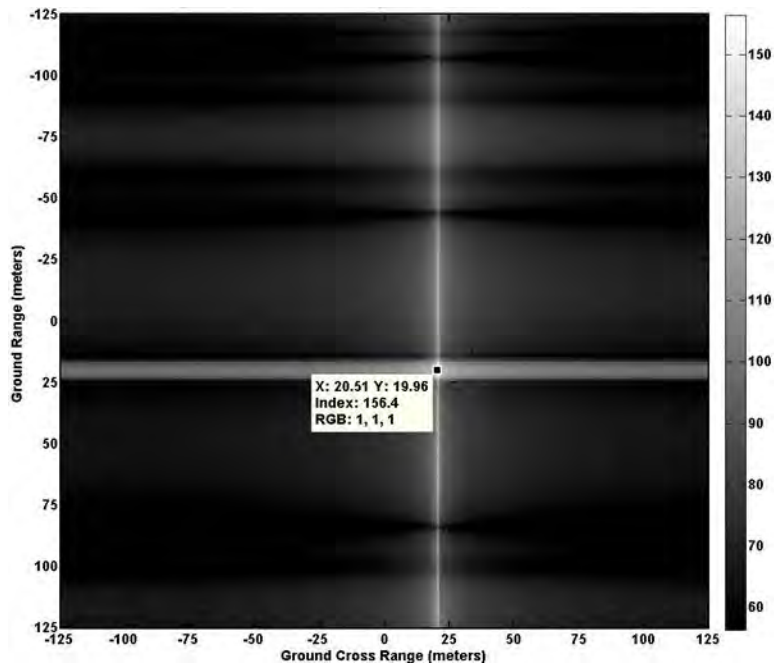True Target Location of the single target as defined in Table 4.

Figure 48.   Simulated Target Location

Simulated Target Location of the single target using parameters as defined in Table 4.
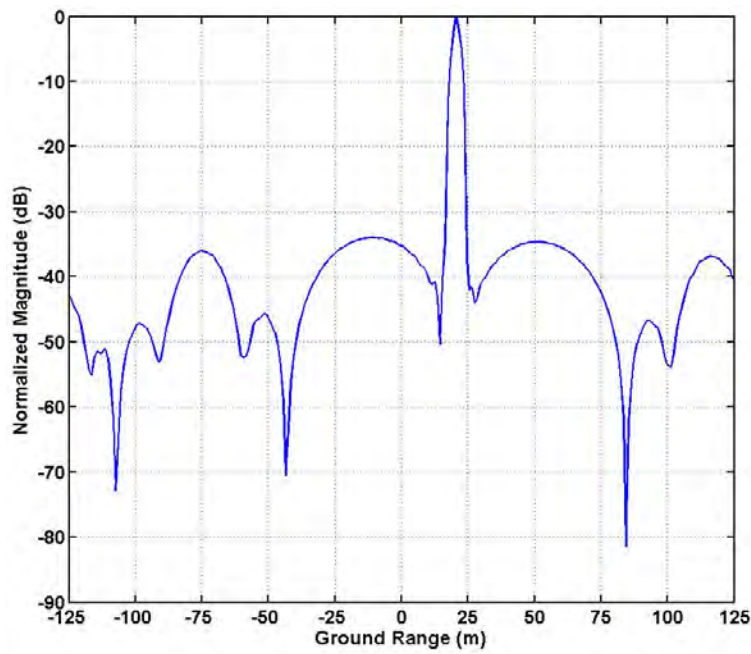
Figure 49.   SAR Image Range Slice

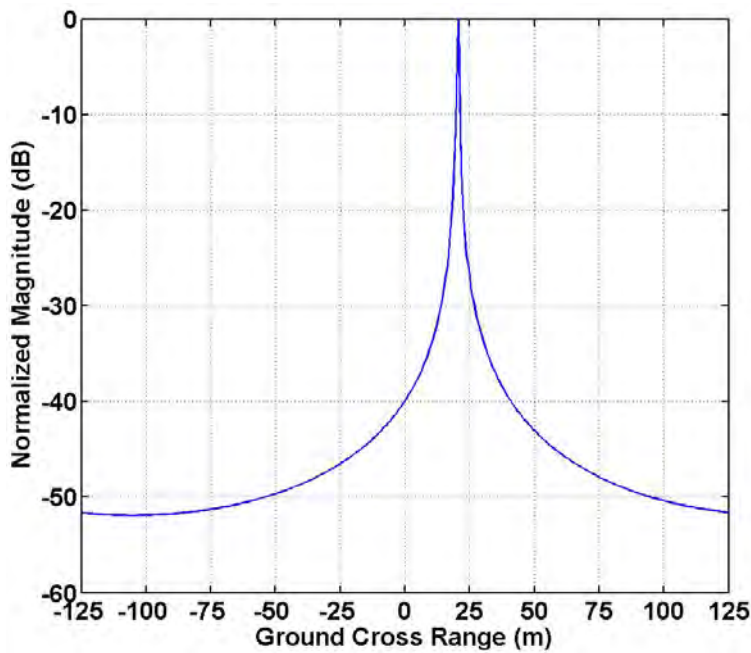Example range slice of a SAR image used to characterize the range sidelobe levels.

Figure 50.   SAR Image Cross-Range Slice

Example cross-range slice of a SAR image used to characterize the cross-range sidelobe levels.

74

C. SINGLE CODE RESULTS

The sidelobes are investigated by taking range and cross-range slices of the SAR image that is produced by the SAR Simulator using the PSK signal. By replotting the data over its corresponding axes, we can separate the range and cross-range image data from each other. This process provides direct access to the data of the sidelobes for each of the individual targets so that the data may be observed and processed.

1. Frank Code

To generate the image slice for the Frank code, the signal parameters from Table 4 are plugged into the PSK signal generator to create the desired Frank modulation. The I/Q data from the modulation is then passed into the SAR Simulator to generate the SAR image, seen in Figure 51.
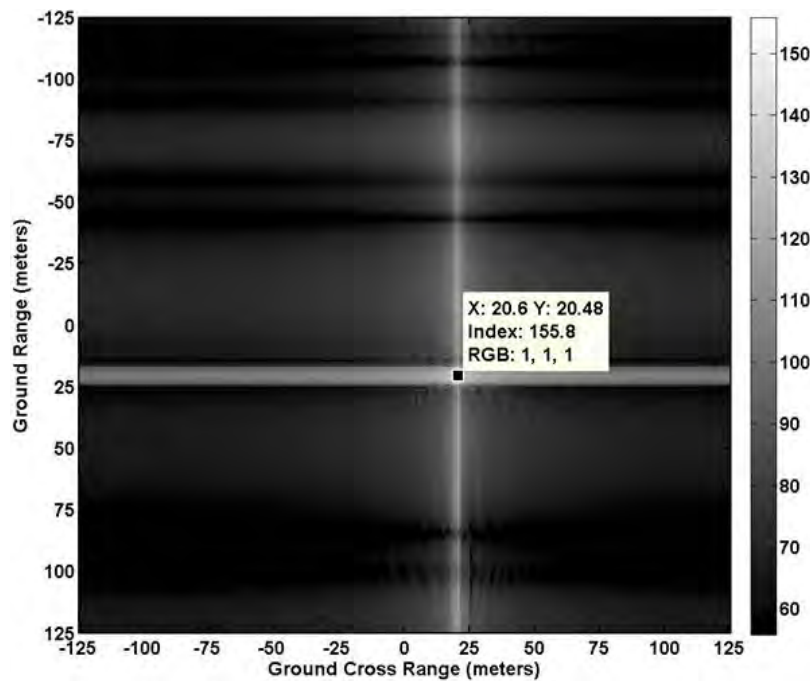

Figure 51.   Frank Code Modulation SAR Image

Frank code SAR Image of the single-point target using radar parameters defined in Table 4.

From Figure 51, we see that the target is in the correct location and within the tolerance of the range and cross-range resolutions. We took image slices in the range and cross-range direction through the single target in the SAR image. These slices extend across the full range and cross-range extent of the SAR image so that all sidelobe characteristics in the SAR image are captured and can be studied. The corresponding plots for the range and cross-range slices are seen in Figure 52 and Figure 53, respectively.
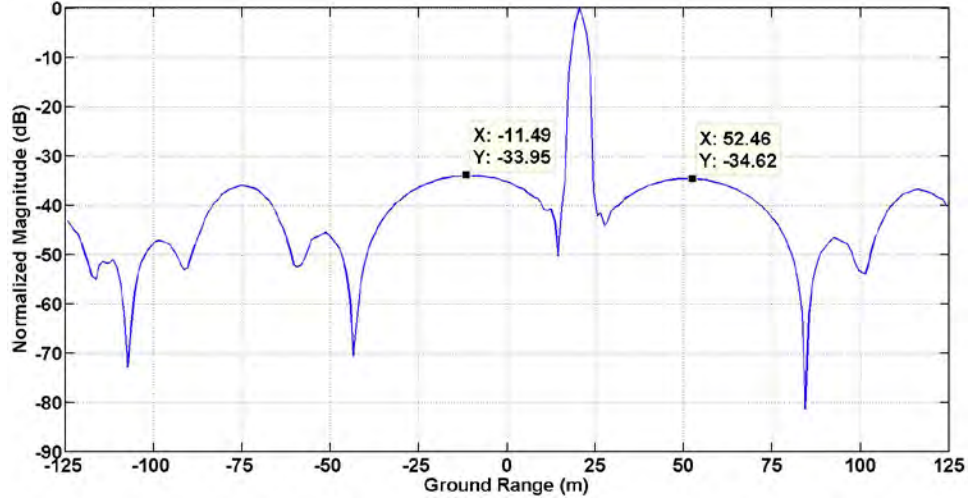

Figure 52.   Frank Code Modulation SAR Image Range Slice

Normalized ground plane range slice of SAR image using the Frank coded waveform and the parameters defined in Table 4.

From Figure 52, we observe that the point target is in the correct location and that the range slice covers the full extent of the image ground range, allowing the sidelobes in the full range extent to be observed. The second item of importance is that the sidelobe structure highly resembles that shown in Figure 10, which was a plot of the ACF for the Frank code with a single waveform reference. This result provides confidence that the SAR Simulator is not greatly distorting the signal through its required image processing. The *PSL* of the image slice theoretically should be about -34 dB. This is calculated by substituting L for the Frank code that is calculated from N_c in Table 4 into (19) with $N =$ 1. From the data tips in Figure 52, we see that the sidelobes are approximately -34 dB from the main peak, with $PSL = -33.9$ dB on the left and $PSL = -34.6$ dB on the right.

From Figure 53, we see that the cross-range peak is in the correct location. The image slice covers the full cross-range extent to ensure complete observation of the SAR Image. We observe no sidelobes in the cross-range direction of the image. This is an area that requires future study. The next code we investigate is the P1 code.
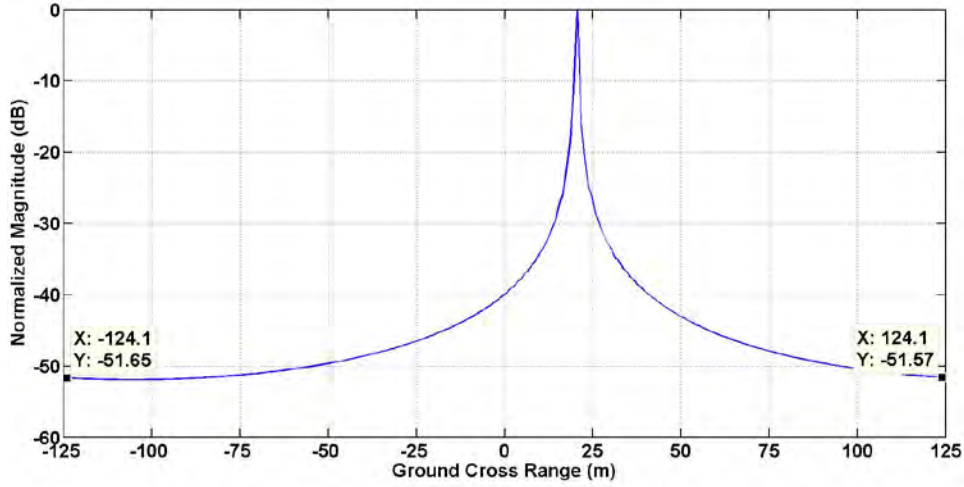

Figure 53.   Frank Code Modulation SAR Image Cross-Range Slice

Normalized ground plane cross-range slice of SAR image at the target location using the Frank coded waveform and the parameters defined in Table 4.

2.   P1 Code

To generate the image slice for the P1 code, the signal parameters from Table 4 are inserted into the PSK signal generator in order to create the desired modulation. The I/Q data from the modulation is then passed to the SAR Simulator, similar to the case for Frank modulation, to generate the SAR image we see in Figure 54. In addition, we observe that the target is in the correct location and within the tolerance of the range and cross-range resolution. This result is important because the P1 code is not studied in [6] and [7]. Using the same approach as in the previous section, we take image slices in the range and cross-range directions. The corresponding plots for the range and cross-range slices are seen in Figure 55 and Figure 56, respectively.
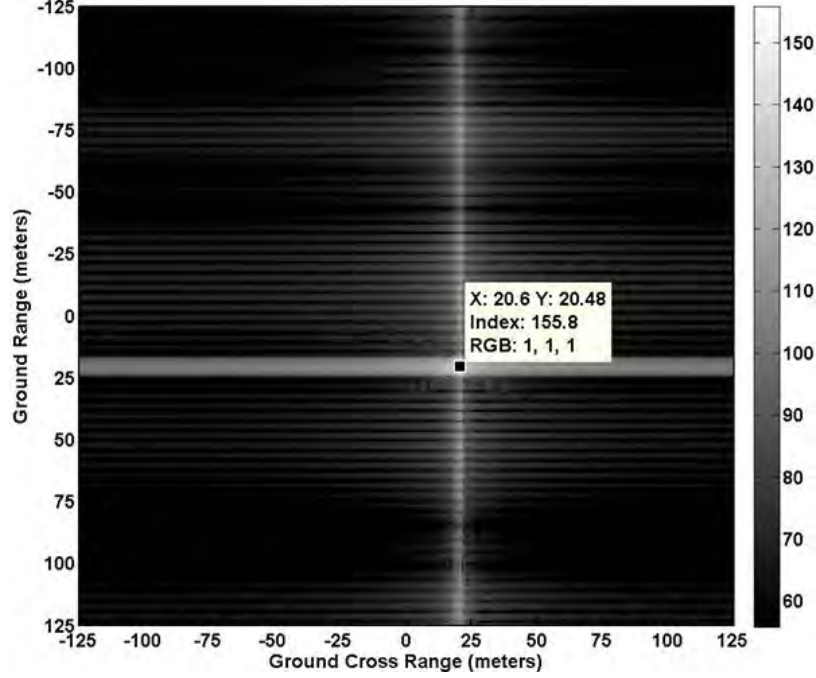
Figure 54.   P1 Code Modulation SAR Image

P1 code SAR Image of the single-point target using radar parameters defined in Table 4.

From Figure 55, we observe that the point target is in the correct location and that the range slice covers the full extent of the image ground range. The sidelobe structure highly resembles that shown in Figure 16, which is the plot of the ACF for the P1 code with a single waveform reference. These results provide confidence that the SAR Simulator is not distorting the signal through its required image processing. The *PSL* of the image slice, theoretically, should be about −34 dB since the *PSL* equation for the P1 code is that same as that for the Frank code. From the data tips in Figure 56, we see that the sidelobes are approximately −34 dB, with *PSL* = −34.2 dB on the left and *PSL* = −34.8 dB on the right.

From Figure 56, we see that the cross-range peak is in the correct location. The image slice covers the full cross-range extent to ensure complete observation of the SAR Image. Just as in the case of the Frank code, we observe no sidelobes in the cross-range direction of the image.
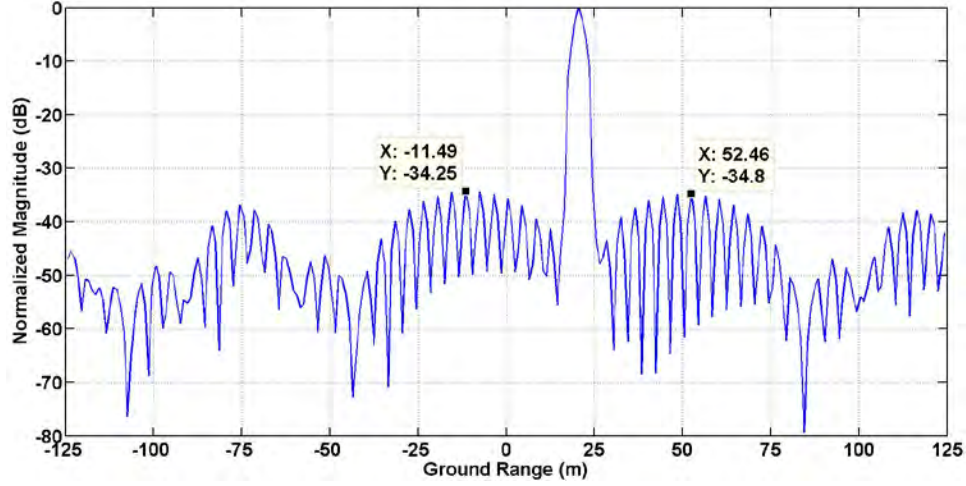
Figure 55.   P1 Code Modulation SAR Image Range Slice

Normalized ground plane range slice of SAR image using the P1 coded waveform and the parameters defined in Table 4.
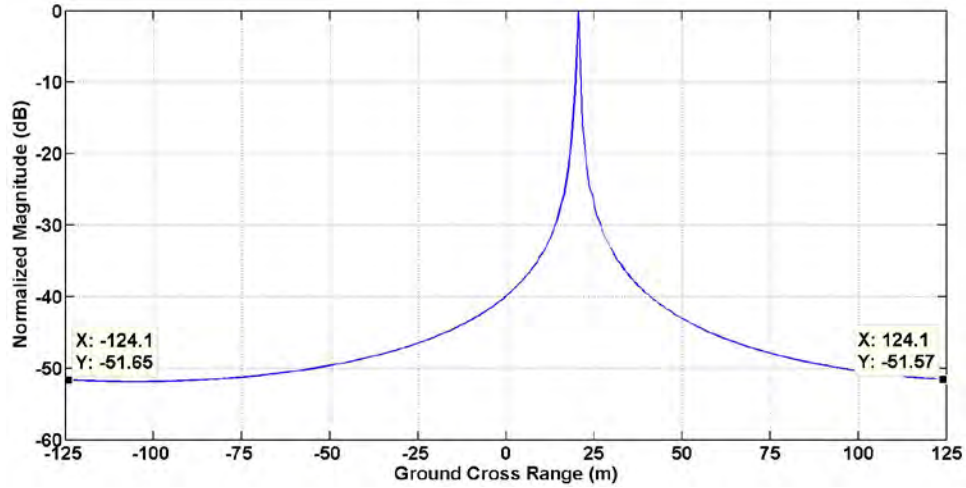

Figure 56.   P1 Code Modulation SAR Image Cross-Range Slice

Normalized ground plane cross-range slice of SAR image using the P1 coded waveform and the parameters defined in Table 4.

3.   P2 Code

To generate the image slice for the P2 code, we use the approach from the previous codes. From the SAR image in Figure 57, we see that the target is in the correct location within the tolerance of the range and cross-range resolution. Because the P2 code was not studied in [6] and [7], it is important to confirm that the SAR simulator is

working properly for the modulation. Again, we take image slices in the range and cross-range direction. The corresponding plots for the range and cross-range slices are shown in Figure 58 and Figure 59, respectively.
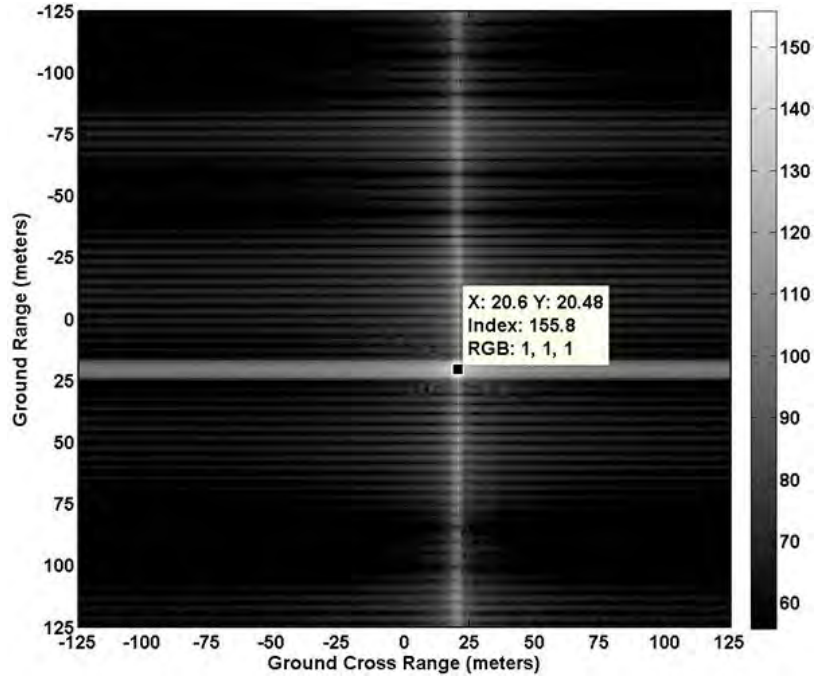

Figure 57.   P2 Code Modulation SAR Image

P2 code SAR Image of the single-point target using radar parameters defined in Table 4.
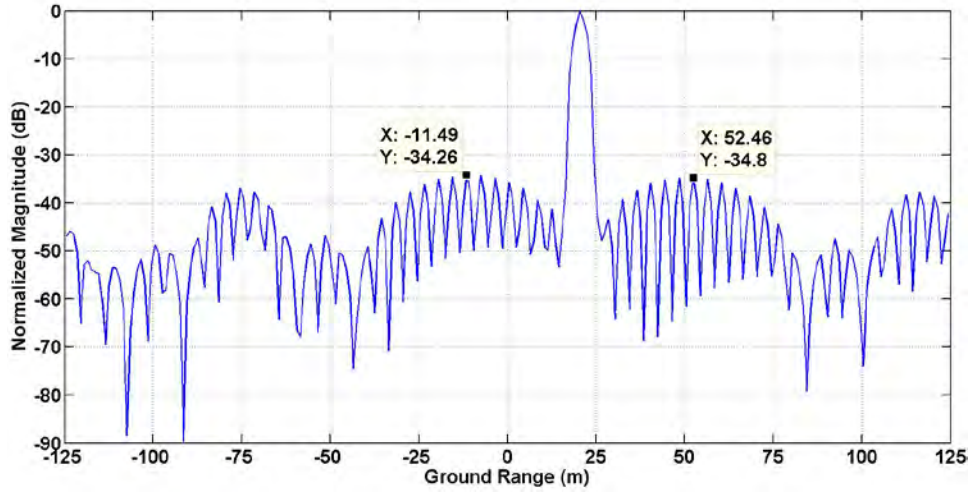
Figure 58.   P2 Code Modulation SAR Image Range Slice

Normalized ground plane range slice of SAR image using the P2 coded waveform and the parameters defined in Table 4.
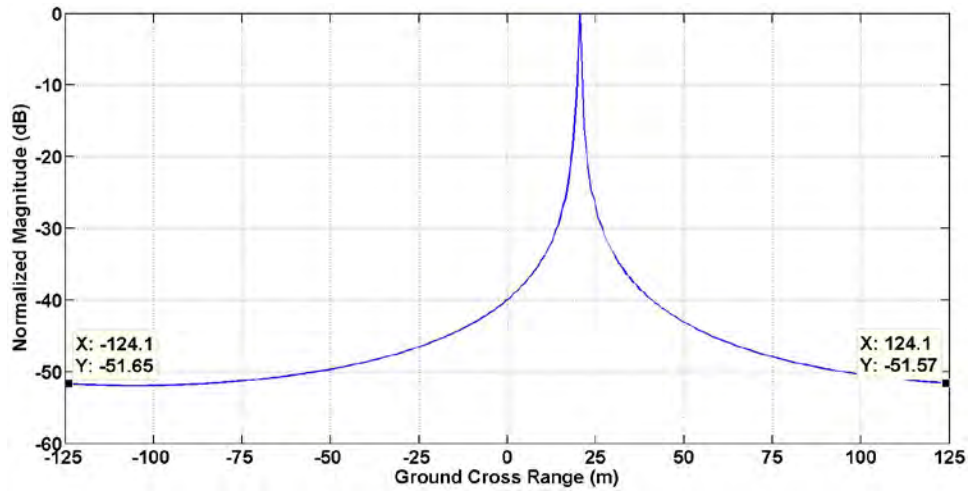

Figure 59.   P1 Code Modulation SAR Image Cross-Range Slice

Normalized ground plane cross-range slice of SAR image using the P2 coded waveform and the parameters defined in Table 4.

4.   P3 Code

The image slices for the P3 code are generated from the SAR image and are created using the parameters listed in Table 4 and seen in Figure 60. From Figure 60, the corresponding plots for the range and cross-range slices are created and can be seen in Figure 61 and Figure 62, respectively.

81

From Figure 61, we observe that the sidelobe structure highly resembles that shown in Figure 26, which was a plot of the ACF for the P3 code with a single waveform reference. The *PSL* of the image slice, theoretically, should be about −31 dB. This is calculated by substituting N_c in Table 4 into (28) with a single waveform reference. From the data tips in Figure 61, we see that the sidelobes are approximately −31 dB, with *PSL* = −30.5 dB on the left and *PSL* = −31.3 dB on the right. From Figure 62, we see that the cross-range peak is in the correct location when compared to Figure 60. Again, the image slice covers the full cross-range extent to ensure complete observation of the SAR Image. We observe no sidelobes in the cross-range image.
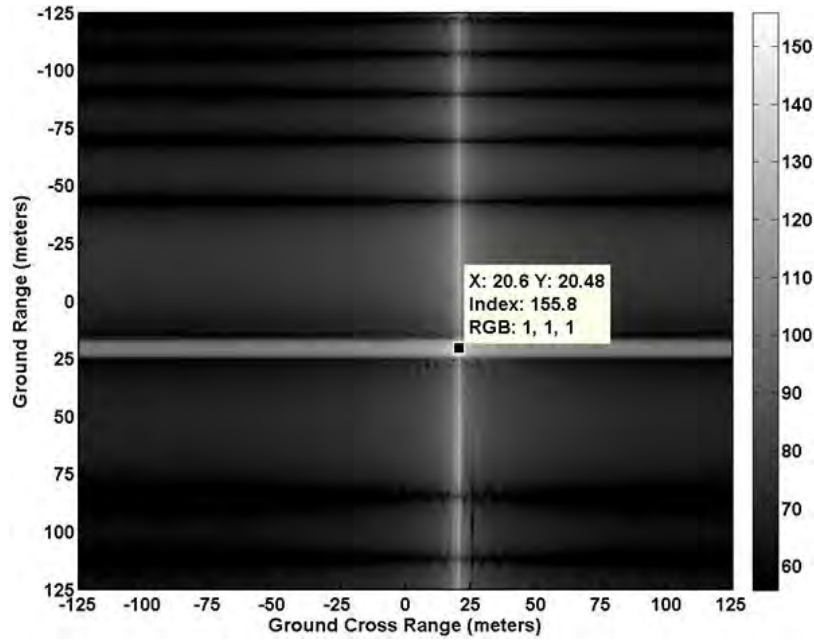

Figure 60.   P3 Code Modulation SAR Image

P3 SAR Image of the single-point target using radar parameters defined in Table 4.
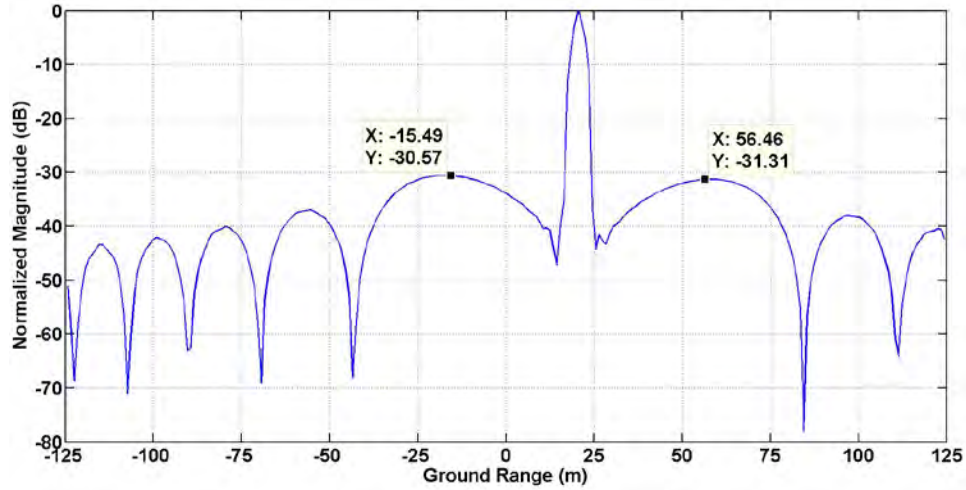
Figure 61.   P3 Code Modulation SAR Image Range Slice

Normalized ground plane range slice of SAR image using the P3 coded waveform and the parameters defined in Table 4.

Figure 62.   P3 Code Modulation SAR Image Range Slice

Normalized ground plane cross-range slice of SAR image using the P3 coded waveform and the parameters defined in Table 4.

5.   P4 Code

To generate the image slice for the P4 code, we insert the signal parameters from Table 4 into the PSK signal generator to create the desired P4 modulation. The P4 SAR image, shown in Figure 63, results from using the Table 4 parameters.

83

From Figure 63, we see that the target is in the correct location and within the tolerance of the range and cross-range resolution. Image slices were taken in the range and cross-range direction through the single target in the SAR image. These image slices extend the full range and cross-range of the SAR image so that all sidelobe characteristics in the SAR image are captured. The corresponding plots for the range and cross-range slices are seen in Figure 64 and Figure 65, respectively.

From Figure 63, we see that the point target is in the correct location. This result is important because the P4 code was not studied in [6] and [7]. It is important to confirm the SAR simulator is working properly for the selected modulation and that the sidelobe structure highly resembles that shown in Figure 29, which is a plot of the ACF for the P4 code with a single waveform reference. This result provides confidence the SAR Simulator is not distorting the signal with its image processing. The *PSL* of the image slice, theoretically, should be about −31 dB, since the *PSL* for the P3 and P4 code are both defined by (28). From the data tips in Figure 64, we see that the sidelobes are approximately −31 dB, with *PSL* = −30.9 dB on the left and *PSL* = −31.5 dB on the right.

Figure 63.   P4 Code Modulation SAR Image

P4 code SAR Image of the single-point target using radar parameters defined in Table 4.
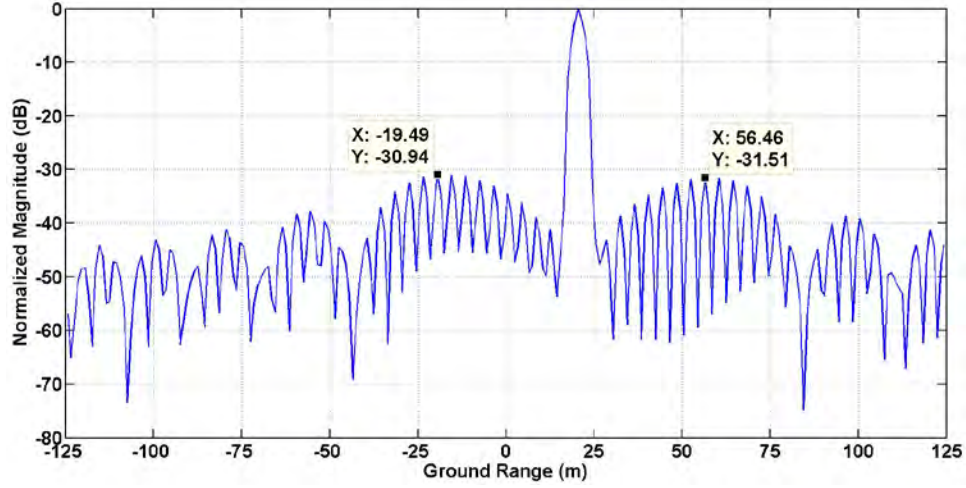
Figure 64.   P4 Code Modulation SAR Image Range Slice

Normalized ground plane range slice of SAR image using the P4 coded waveform and the parameters defined in Table 4.
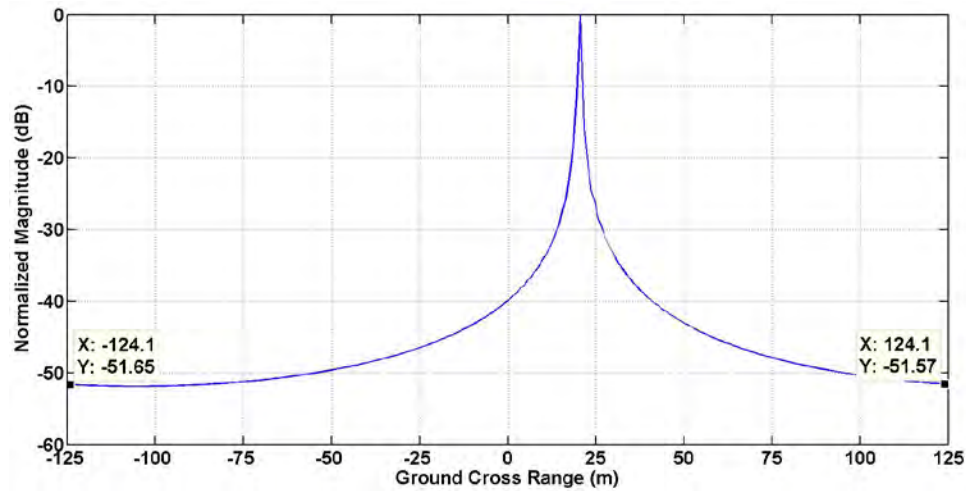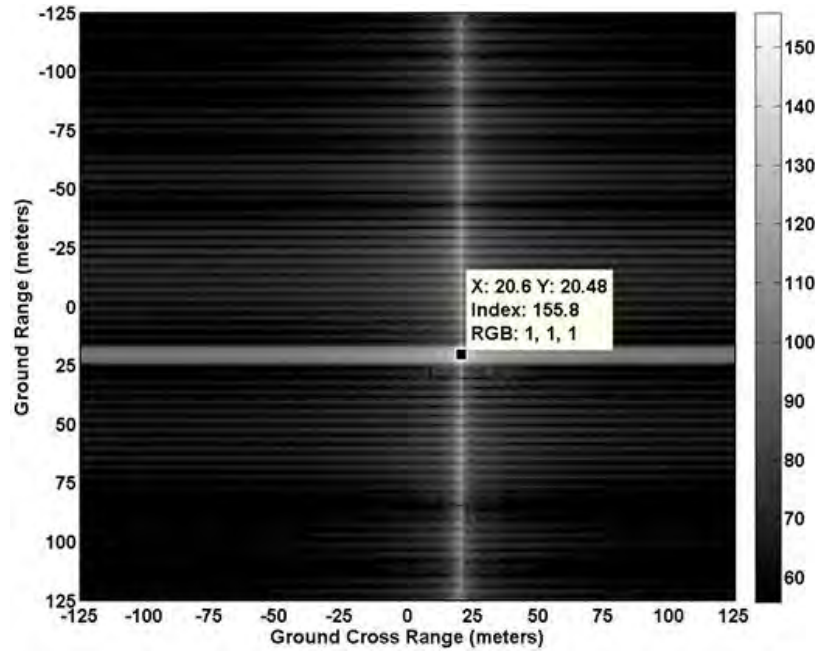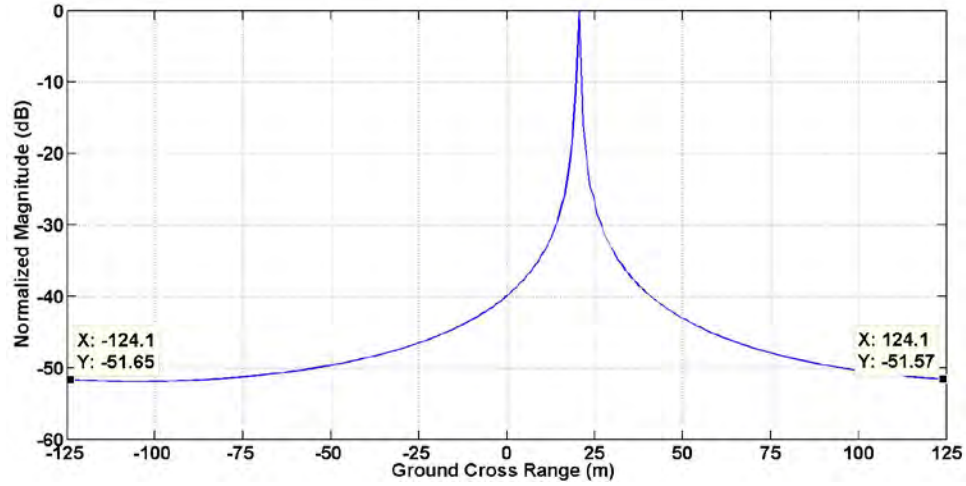

Figure 65.   P3 Code Modulation SAR Image Cross-Range Slice

Normalized ground plane cross-range slice of SAR image using the P4 coded waveform and the parameters defined in Table 4.

In Figure 65, we see that the cross-range peak is in the correct location when compared to Figure 63. Again, the image slice covers the full cross-range extent to ensure complete observation of the SAR Image. No sidelobes are observed in the cross-range direction of the image.

The SAR image slices shown in Figures 52, 55 and 58 indicate that the P1, P2 and Frank codes, respectively, have the lowest *PSL* when a single reference waveform is considered. This result is also displayed in Figure 66, a comprehensive plot of all five PSK codes. The P3 and P4 codes *PSL* shown in Figure 66 is 3-dB worse than that of the P1 and Frank codes, matching theory from Chapter III. We also found in Chapter III that the P2 codes *PSL* degrades as the number of integrated waveforms increases. This result leads to the next section, where the *PSL* of the individual signals are investigated when pulse integration is used.

Figure 66.   Single Waveform Reference Range Slice Composite

All PSK waveforms normalized ground plane range slices taken from their respective SAR images using parameters defined in Table 4.

D.   RESULTS FROM INTEGRATION OF MULTIPLE PSK CODES

As mentioned in Chapter III, four of the five PSK codes studied have perfect sidelobe responses when the waveform is periodic. If the code period of the waveform is small enough, it is possible to cascade multiple waveforms together to gain the benefit of pulse integration.

To find the time that is available between observation points in the synthetic aperture, we divide the observation time by the desired number of observation points. To do this, we first substitute the needed parameters from Table 4 into (54) to find

$$T_{obs} = \frac{\sqrt{R_{Gr}^2 + Z_0^2}\, c/f_c}{2V_p \delta_{cr}}$$
$$T_{obs} = \frac{\sqrt{3 \times 10^4\ \text{m}^2 + 10^3\ \text{m}^2}\left(3 \times 10^8\ \text{m/s}\right)/\left(9 \times 10^9\ \text{s}^{-1}\right)}{2\left(200\,\text{m/s}\right)1\ \text{m}} \approx 2.5\ \text{s}.$$

(62)

By taking the result of (62) and dividing it by the number of observation points from Table 4, we find that the total time between observation points is

$$\Delta t_{obs} = \frac{T_{obs}}{\#\,Observations} = \frac{2.5\ \text{s}}{250} = 10\ \text{ms}.$$

(63)

To find the number of code sequences that can be cascaded in the 10 ms calculated from (63), we divide (63) by the code period from (8) using the parameters in Table 4 to get

$$\frac{\Delta t_{obs}}{N_c t_b} = \frac{10\ \text{ms}}{\left(256\right)\left(6.67\ \text{ns}\right)} \approx 5856.$$

(64)

From (64), we see that a substantial number of code sequences can be cascaded together; however, range migration effects may occur if using the total number of cascaded waveforms. For this investigation, we assume that 128 waveforms can be cascaded without the effect of range migration. In future analyses, researchers should consider range migration for these waveforms and develop a range migration algorithm.

Using the 128 cascaded waveforms, we recreated the previous range slice plots and placed them into a single graph as shown in Figure 67. From Figure 67, we see that the P2 waveform *PSL* has drastically increased as compared to the other four PSK waveforms. This shows that the P1 and the Frank codes have the lowest *PSL* of the five PSK waveforms when waveform integration is considered.
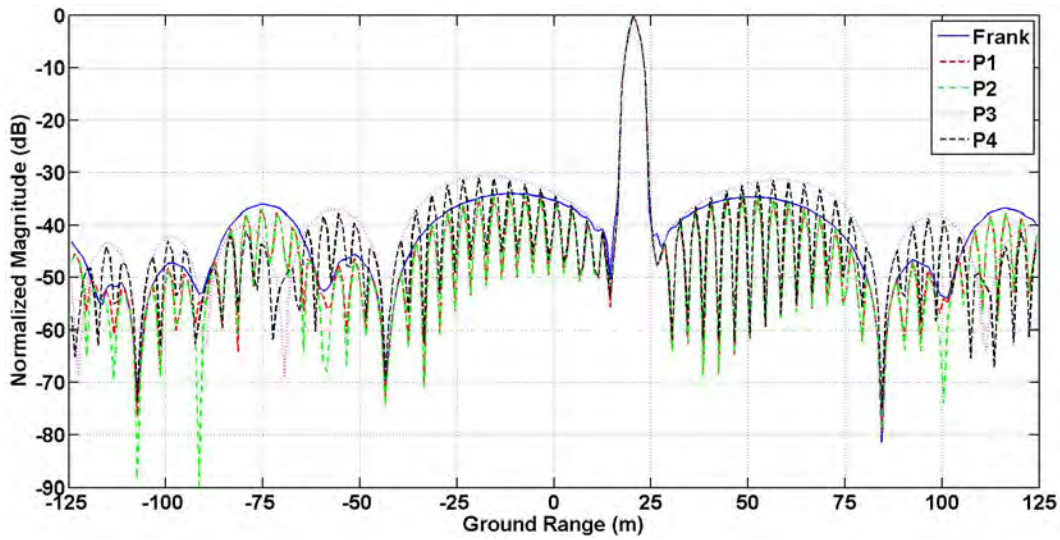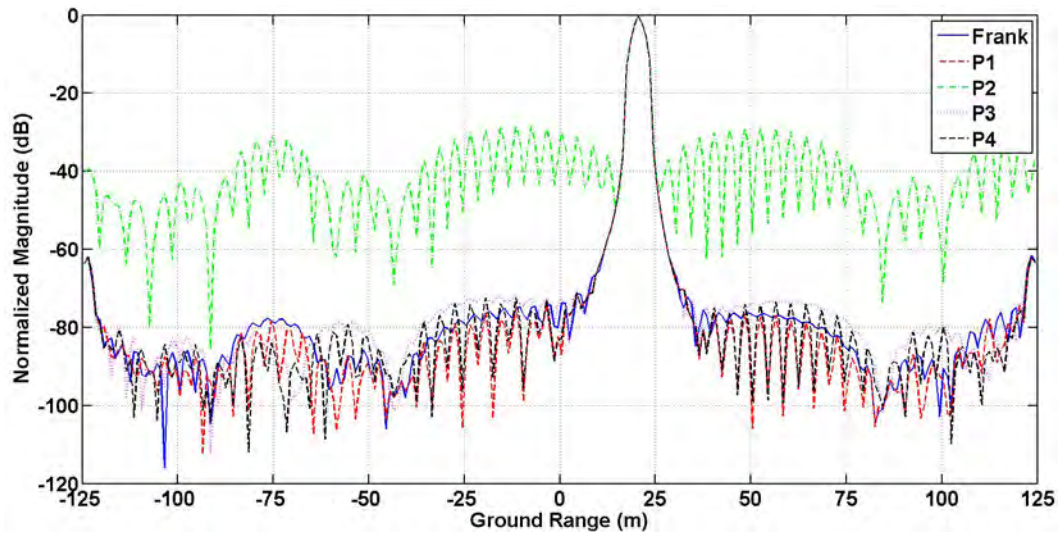
Figure 67.   Multiple Waveform Reference Range Slice Composite

All PSK waveforms normalized ground plane range slices taken from their respective SAR images using parameters defined in Table 4 with the number of consecutive waveforms per observation point set to 128.

VII.   CONCLUSIONS

A.   DISCUSSION OF RESULTS

In this chapter, we summarize and discuss the results displayed in the previous chapter. Due to lack of sidelobe structure in the cross-range slices as seen in all cross-range plots for all five PSK codes, we cannot discuss which modulation performs best in the cross-range direction. This issue is retained as a possible course for future studies in this area.

The range sidelobe structure of the individual PSK codes provide a means of comparison, as seen in Figure 66 and Figure 67. In the summary of results in Table 5, it is evident that the P1 and P2 codes have the lowest *PSL* at −34.2 dB, with the Frank code slightly having a slightly higher *PSL* at −33.9 dB for a single waveform echo. The P3 and P4 are approximately 3 dB greater than the P1, P2 and Frank codes, which match theory when their respective *PSL* equations are compared, as discussed in Chapter III.

Table 5.   Summary of PSL Results from the Single-Target Range
Slices Using a Single Waveform

Modulation	Normalized Sidelobe (Left) (dB)	Normalized Sidelobe (Right) (dB)	Maximum *PSL* (dB)
Frank	−33.9	−34.6	−33.9
P1	−34.2	−34.8	−34.2
P2	−34.2	−34.8	−34.2
P3	−30.5	−31.3	−30.5
P4	−30.9	−31.5	−30.9

We see from Figure 67 and from the tabulated results in Table 6 that the P2 code loses its favorable *PSL* once pulse integration is considered. From the information shown in Table 5 and Table 6, it seems the P1 and Frank codes have the best peak sidelobe levels of the five PSK codes, with the P1 performing slightly better than the Frank code.

Table 6.   Summary of PSL Results from the Single-Target Range
Slices after Integrating 128 Waveforms

Modulation	Normalized Sidelobe (Left) (dB)	Normalized Sidelobe (Right) (dB)	Minimum PSL (dB)
Frank	−74.2	−76.1	−74.2
P1	−74.1	−76.0	−74.1
P2	−28.4	−28.8	−28.4
P3	−72.2	−73.3	−72.2
P4	−72.5	−73.4	−72.5

B.   FUTURE WORK

A few areas of possible future work are identified in this thesis. The first area is defining the point at which range migration becomes a factor and identifying the parameters that affect the image results. This will help to determine whether or not these PSK-type signals can be used for spotlight mode SAR and in what capacities; specifically, if they can be used in CW operation and if there is a limit to the number of code sequences that can be used. As shown in this thesis, there are great sidelobe benefits to using multiple code sequences; however, there are range migration issues if multiple codes sequences are used. This area needs to be studied to either confirm or deny that a range migration algorithm needs to be developed.

Previous work has shown that SNR benefits from using pulse integration. We can study this to determine how much processing gain can be achieved. This idea would apply to LPI-type research for SAR because when more energy is integrated over time, less peak energy is transmitted, making the radar more LPI in nature [9].

In the future, the Doppler tolerance of the individual waveforms should be considered prior to selecting the best of the five PSK codes.

A final area of future study could extend from recent studies using the Robust Symmetrical Number System with the P4 code, which has been shown to improve the unambiguous range of the code. This would allow shorter codes to cover larger spaces. This means that for the same amount of processing time, more code sequences could be transmitted and integrated to improve SNR and sidelobe response.

LIST OF REFERENCES

[1] M. Skolnik, *Introduction to Radar Systems*, 3rd ed., New York, NY: McGraw Hill, 2001.

[2] T. Freeman, "What is imaging radar?," Jet Propulsion Labratories, 26 January 1996. [Online]. Available: http://southport.jpl.nasa.gov/desc/ imagingradarv3.html.

[3] W. G. Carrara, *Spotlight Synthetic Aperture Radar, Signal Processing Algorithms*, Norwood, MA: Artech House, 1195.

[4] C. Ozdemir, *Inverse Synthetic Aperture Radar with MATLAB Algorithms*, Hoboken, NJ: John Wiley and Sons, 2012.

[5] C. V. Jakowatz, *Spotlight-Mode Synthetic Aperture Radar: A Signal Processing Approach*, New York, NY: Springer Science+Business Media, Inc., 1996.

[6] D. Garren, P. Pace and R. Romero, "Phenomenology of low probability of intercept synthetic aperture radar via Frank codes," in *Proc. of SPIE, Algorithms for Synthetic Aperture Radar Imagery XXI*, Baltimore, 2014.

[7] D. A. Garren, P. E. Pace and R. A. Romero, "Use of P-3 coded transmission waveforms to generate synthetic aperture radar images," in *Proc. of the IEEE Radar Conference*, Cincinnati, Ohio 2014.

[8] C. Oliver and S.Quegan, *Understanding Synthetic Aperture Radar Images*, Norwood, MA: Arctech House, 1998.

[9] P. E. Pace, *Detecting and Classifying Low Probability of Intercept Radar*, 2nd ed., Norwood, MA: Artech House, 2009.

[10] M. Soumekh, *Synthetic Aperture Radar Signal Processing*, Hoboken, NJ: John Wiley & Sons, Inc., 1999.

[11] C. Ozdemir*, Inverse Synthetic Aperture Radar with MATLAB Algorithms*, Hoboken, NJ: John Wiley and Sons, 2012.

[12] L. F. Chaparro, *Signals and Systems Using MATLAB, Second Edition*, San Diego, CA: Academic Press, 2015.

[13] S. Haykin, *Communication Systems*, New York, NY: John Wiley & Sons, Inc., 2001.

[14] National Instruments Corporation, "What is I/Q data?," 6 Febuary 2014. [Online]. Available: http://www.ni.com/white-paper/4805/en/. [Accessed 29 December 2014].

[15] N. Levanon and E. Mozeson, *Radar Signals*, Hoboken, NJ: John Wiley & Sons, Inc., 2004.

[16] F. Neri, *Introduction to Electronic Defense Systems*, 2nd ed., Norwood, MA: Artech House, 2001.

[17] D. R. Wehner, *High-Resolution Radar*, 2nd ed., Norwood, MA: Artech House, 1995.

[18] D. L. Mensa, *High Resolution Radar Cross-Section Imaging*, Norwood, MA: Artech House., 1991.

[19] G. Lanari and R. Franceschetti, *Synthetic Aperture Radar Processing*, Boca Raton, FL: CRC Press, 1999.

[20] B.Wang, *Digital Signal Processing Techniques and Applications in Radar Image*, Hoboken, NJ: Wiley and Sons, 2008.

[21] M. Skolnik, *Radar Handbook*, 3rd ed., New York, NY: McGraw-Hill, 2008.

INITIAL DISTRIBUTION LIST

1. Defense Technical Information Center
   Ft. Belvoir, Virginia

2. Dudley Knox Library
   Naval Postgraduate School
   Monterey, California